# MicroTesla Enabled 3D Printing Microfluidic Co-culturing of Adipocytes and Beta Cells for Diabetes on a Chip

**by**

**Kai Duan**

**A dissertation submitted in partial fulfillment**
**of the requirements for the degree of**
**Doctor of Philosophy**
**(Mechanical Sciences and Engineering)**
**in the University of Michigan-Dearborn**
**2023**

**Dissertation Committee:**

**Associate Professor Joe Fujiou Lo (Chair)**
**Associate Professor Gargi Ghosh**
**Associate Professor Mathumai Kanapathipillai**
**Professor Yasha Yi**
**Professor Oleg Zikanov**

# Acknowledgements

I would like to take this opportunity to express my gratitude to all those who have supported me throughout my doctoral journey.

First and foremost, I would like to express my deepest appreciation to my supervisor, Dr. Joe Lo, for his unwavering guidance, invaluable feedback, and endless patience. His expertise, support, and encouragement have been instrumental in shaping my research and guiding me towards the successful completion of my PhD.

I am also grateful to my thesis committee members, for their insightful comments and constructive criticism that have significantly improved the quality of my research.

I am indebted to my colleagues, friends, and family, who have offered their support and encouragement throughout my PhD. Their encouragement and motivation have helped me to persevere through the challenges and setbacks I have encountered during my research.

Thank you all for your support and encouragement.

# Table of Contents

# List of Figures

# Abbreviations

| | |
|---|---|
| ABS | acrylonitrile butadiene styrene |
| ER | endoplasmic reticulum |
| FFA | free fatty acid |
| FFT | fast Fourier transform |
| FSS | flow shear stress |
| GSIR | glucose-stimulated insulin response |
| PDMS | polydimethylsiloxane |
| PEG | polyethyl glycol |
| PLA | polylactic acid |
| PET | polyethylene terephthalate |
| RGD | arginylglycylaspartic acid |
| SLP | stereolithography |
| VDCCs | voltage-dependent calcium channels |

# Abstract

Diabetes has become a serious life-threatening pandemic disease: 1.5 million people perish as a direct result of diabetes each year worldwide. Due to the lack of methods for diabetes prevention and treatments, there is an urgent need to explore the mechanisms in diabetes and its related health disorders, such as obesity; excessive arterial stiffness; hypertension; cerebral microvascular complications, among others. In particular, diabetic patients with comorbidities like cancer, kidney dysfunction, and cardiovascular conditions have more complications and lower survival rates than those without diabetes. To better understand the mechanisms and pervasive effects of diabetes throughout the body, researchers are actively developing *in vitro* and *in vivo* models. One promising technique is microfluidics—where cellular and tissue microenvironments are precisely controlled to mimic pathophysiological conditions, within devices we call disease-on-a-chip. By combining the advantages of cell and tissue engineering, materials engineering, and on-chip biosensing, microfluidics has become a powerful tool for biomedical and disease research.

This dissertation reports the approaches and results in microfluidic device fabrication, microfluidics oxygen gradient generating; cells stimulation; biosensing; hydrogel-based biosensors fabrication; and integrated on-chip disease model building. From the outcome points of view, this dissertation provided a comprehensive method to fabricate flow-source integrated microfluidics in fast and cost-efficient ways, examined the beta cells dysfunction under oxygen and glucose stimulations, and in combination, realized an on-chip co-culture model to study the

relationship between obesity and diabetes. Following the microfluidics development, the dissertation was divided into four main parts: i) beta cells stimulation and sensing under oxygen gradient, ii) μTesla pump design and fabrication, iii) 3D printed microfluidic device, and iv) co-culture of adipocytes and islet beta cells. The oxygen microfluidics were fabricated using traditional SU8/PDMS softlithography. The prototype μTesla pump was fabricated using Stereolithography (SLP) 3D printing. The pump integrated co-culture device was fabricated via Fused Deposition Modeling 3D (FDM) printing. These fabrication methods showed a progressive advancement of our device techniques. Moreover, oxygen gradients was generated by the oxygen diffusion and nitrogen conviction inside the microfluidic channels. The integrated device was enabled co-culturing of adipocytes and beta cells. The cells were then stimulated by oxygen and glucose, with the insulin secretion from beta cells and IL-6 secretion from adipocytes detected using hydrogel enhanced biosensors. Membrane Znt8 level were measured under microscopy using fluorescent probes. With the integrated device, we demonstrated the *in situ* detection of insulin, IL-6, and Znt8 during the co-culture of adipocytes and beta cells in response to oxygen and glucose stimulation. This demonstrated the power of our 3D printed co-culture platform for on-chip diabetes research. In future applications, this platform can also be functionalized to many other disease models for biomedical studies.

# Chapter 1. Visualizing Hypoxic Modulation of Beta Cell Secretions via a Sensor Augmented Oxygen Gradient

One distinct advantage of microfluidic-based cell assays is their scalability for multiple concentrations or gradients. Microfluidic scaling can be extremely powerful when combining multiple parameters and modalities. Moreover, *in situ* stimulation and detection eliminates variability between individual bioassays. However, conventional microfluidics must combat diffusion, which limits the spatial distance and time for molecules traveling through microchannels. Here, we leveraged a multilayered microfluidic approach to integrate a novel oxygen gradient (0-20%) with an enhanced hydrogel sensor to study pancreatic beta cells. This enabled our microfluidics to achieve spatiotemporal detection that is difficult to achieve with traditional microfluidics. Using this device, we demonstrated the *in situ* detection of calcium, insulin, and ATP (adenosine triphosphate) in response to glucose and oxygen stimulation. Specifically, insulin was quantified at levels as low as 25 pg/mL using our imaging technique. Furthermore, by analyzing the spatial detection data dynamically over time, we uncovered a new relationship

between oxygen and beta cell oscillations. We observed an optimum oxygen level between 10 and 12%, which is neither hypoxic nor normoxic in the conventional cell culture sense. These results provide evidence to support the current islet oscillator model. In future applications, this spatial microfluidic technique can be adapted for discrete protein detection in a robust platform to study numerous oxygen-dependent tissue dysfunctions.

## 1.1 Introduction

Spatial transport and concentrations of molecules between cells are important in many physiological processes. Specifically, oxygen, calcium, insulin, and other signaling molecules play major roles in diabetes-related pathologies. Oxygen and hypoxia, for instance, are closely controlled via hypoxia-inducible factors and exhibit spatial gradients in diabetic tissues (fat and islets) [1-13]. Furthermore, intracellular calcium and cell-to-cell calcium transport demonstrate dynamic concentrations in pancreatic beta cells [14-16]. However, contemporary techniques using molecular assays and fluorescence microscopy can only determine responses at single concentrations and static time points, rather than a gradient of concentrations dynamically over time. These assays and microscopy techniques were designed for discrete concentrations and require lengthy sample preparations. To address these limitations, microfluidic devices have been realized to enable spatial and dynamic studies of molecular transport in islets and beta cells, providing rapid transient detection or microscopy imaging of pathophysiological conditions in diabetes [17-21]. However, these contemporary microfluidics prioritize either spatial gradients or fast detection dynamics as they combat diffusion in microchannels. We previously addressed this diffusion limitation by coupling nitrogen convection to drive diffusion[22]. In this work, we further leveraged our spatial microfluidic oxygen gradient combined with integrated calcium, ATP, and

insulin detection to study beta cell hypoxia *in situ*. In contrast to previous hypoxia studies[18], in this study, a gradient of oxygen concentrations was applied across an entire Beta TC6 culture. Thus, we extended current detection techniques in both spatial and temporal dimensions for beta cell studies. Using this novel technique, we uncovered a relationship between calcium and insulin modulation as a function of oxygen levels.

### 1.1.1 Islet Calcium and Insulin Oscillations

To illustrate the dynamics of signaling molecules in beta cells, we summarize here the process of the glucose-stimulated insulin response (GSIR). GSIR begins with glucose uptake, followed by an increase in the ATP/ADP (adenosine triphosphate/adenosine diphosphate) ratio due to glucose metabolism. This upsurge in ATP closes ATP-dependent potassium ($K_{APT}$) channels, which depolarizes the membrane and triggers a calcium influx through voltage-dependent calcium channels (VDCCs). This intracellular calcium flux then prompts the exocytosis of packaged insulin vesicles. *In vitro* and *in vivo*, both calcium flux and insulin secretions exhibit oscillations on a time scale from 10 seconds to several minutes [14-16, 23-25]. These calcium oscillations propagate as a wave across beta cells in an islet [14-26]. The faster oscillations are based on electrical modulations of membrane potentials [23, 27, 28], while the slower, minute-scaled oscillations are based on metabolite modulations [23, 28, 29]. Oxygen can modulate membrane channels responsible for electrical oscillations [18, 30-32]. Oxygen can also modify glucose metabolism and thus affect metabolite oscillations [23, 30, 33, 34]. These aspects of calcium oscillation represent cell-to-cell communications in islets [14-16, 26], of which oxygen may be a key modulator. While both types of oscillation affect insulin secretion [23, 35], mitochondrial ATP specifically affects GSIR sensitivity [15, 36]. However, a systematic assay of oxygen on calcium

or insulin using a gradient is lacking. To visualize these temporal oscillations and their modulation by oxygen, a spatial gradient with integrated GSIR detection would be the ideal experimental platform. Moreover, such a platform could test whether Beta TC6 cells can mount the same kind of ATP responses to glucose stimulation as other beta cell lines (see supplementary data) and whether their ATP responses coincide with calcium or insulin modulation across the cell culture.

### 1.1.2 Advantages of Gradient-Based Multimodal Microfluidics

To enable oxygen modulation and spatial detection within the same device, we designed a multilayered construct by integrating our membrane-based gas microfluidics [18, 19, 22] with a porous hydrogel sensor layer [37, 38] (Figure 1.1). As described in our previous work, this gas microfluidics balanced oxygen diffusion against nitrogen convection [22] and expressed a 0-20% hypoxia gradient across a 200 μM polydimethylsiloxane (PDMS) membrane (Figure 1.1A). Note that the gradient was designed to span the range below atmospheric oxygen (21%) with symmetry so that both halves could be used. Across this membrane, a polyethyl glycol (PEG)-based hydrogel was created to provide a surface for cell attachment and insulin immunodetection. Cell attachment was enabled via Arginylglycylaspartic acid (RGD) peptides copolymerized in the hydrogel. Insulin detection provided capture antibody within the hydrogel. Additionally, porosity generated via nonacrylated PEG fragments enhanced the molecular transport and thus detection sensitivity in the hydrogel [37, 38]. The complete microfluidic device was fabricated by bonding the multiple layers one by one, as shown in Figure 1.1B. To physically immobilize this multifunctional hydrogel, both silane chemistry and surface texturization were applied to enhance gel-PDMS bonding (Figure 1.1C).

As a result, the device was capable of dynamically imaging GSIR with *in situ* calcium, ATP, and insulin detection. Together with the integrated oxygen gradient, the device increased the throughput of conducting beta cell experiments. Our design utilized both enhancements in scaling and reaction kinetics afforded by microfluidics. It offered novel visualization of calcium oscillations across beta cell cultures, a multiplexing of spatial and temporal parameters that was difficult to achieve using contemporary microfluidics.

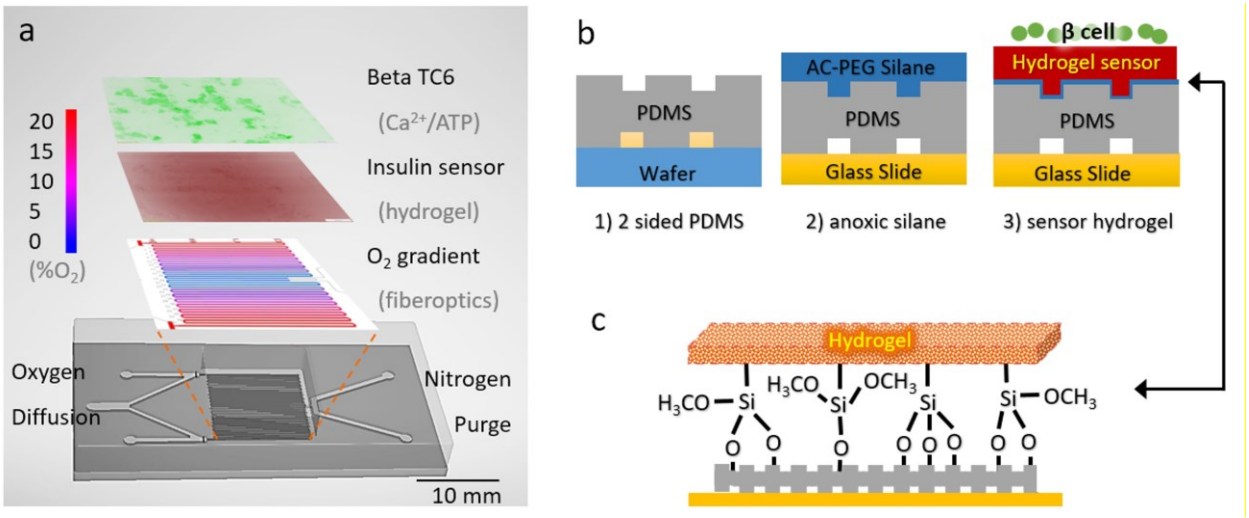


Figure 1-1 Microfluidic oxygen gradient with spatial hydrogel sensor. A. The microfluidic device contains multiple layers. The gas layer balances oxygen diffusion (red) with nitrogen convection (blue) to create a 0 to 20% gradient as measured with a fiber optic oxygen probe. Note that the gradient is symmetrical, so either half can be used. The 200 µM polydimethylsiloxane (PDMS) membrane that defines the gas channels is highly permeable to oxygen and diffuses the gradient to the hydrogel and cell culture seeded atop. On top of the oxygen gradient, a porous hydrogel sensor was bonded to the microchannels. This hydrogel encapsulates anti-insulin capture antibodies, 20k polyethylene glycol (PEG) porogen, and arginylglycylaspartic acid (RGD) peptides to provide cell attachment and insulin detection. The open top aqueous reservoir allows normal cell culture processes and fluorescence microscopy. B. The fabrication process of the multilayered microfluidics begins with normal photolithography and PDMS molding. During the chemical surface modifications, a nitrogen chamber is used to prevent oxygen inhibition of hydrogel cross-linking at the PDMS-gel interface. The resultant sandwich is washed with buffer to remove uncross-linked reagents and porogens to complete the porosity-enhanced hydrogel sensor. C. Moreover, attachment of the functionalized hydrogel is achieved through both topological and chemical surface modifications. Microtextures are patterned on the cell facing the side of the PDMS membrane to increase the surface area in contact. Then, the sandwich is incubated with acrylated silane to create Si-O-bonds to tether the hydrogel backbones.

## 1.2 Materials and Methods

### 1.2.1 Fabrication of the Microfluidic Device

The device molds were fabricated using SU-8 photolithography methods. Briefly, an SU-8 2100 (Microchem) was spin-coated on a silicon wafer (University Wafer) to yield a 100 μm thick layer, soft baked and exposed to UV light through a mask. After the postexposure bake, it was finally developed with an SU-8 developer. The thickness of the channel for the gradient layer was measured using a surface profilometer. The surface of the wafer was plasma treated and then left in a vacuum overnight for salinization with trichloro (1H,1H,2H,2H-perfluorooctyl). To enable hydrogel bonding on top of the gas microfluidics, a double-sided PDMS membrane was fabricated using two SU8 masters First, a 200 μm membrane was molded over the gas microchannel master by spin coating PDMS. Then, a 100 μm membrane was molded on a separate wafer master to define the surface textures. These two membranes were bonded back-to-back to create a single layer with features of both sides. This two-sided membrane was then plasma bonded to a glass slide to enclose the gas channels with the textures exposed. Finally, a 1 cm thick PDMS gasket was cut and bonded to create the cell culture chamber.

### 1.2.2 Polyethylene Glycol Diacrylate (PEGDA) Hydrogel Preparation

UV curable PEGDA hydrogel solution was prepared with the following: 8% PEGDA 6k (Sigma), 10% PEG 20k for porogen (Sigma), and 200 pg/mL of acrylated anti-insulin antibody. Anti-insulin was synthesized via the reaction between acrylate-PEG-SVA 5k (Laysan Bio) and anti-insulin (mouse MAB1 clone, Sigma) and incubated in phosphate-buffered saline (PBS) at

room temperature for 3 hours. Finally, 3 mM acrylamide-PEG5k-RGD and 2% photoinitiator 2-hydroxy-4'-(2-hydroxyethoxy)-2-methylpropiophenone (Sigma) were added to create the hydrogel precursor.

### 1.2.3 PEGDA Hydrogel on PDMS

Before pouring the hydrogel prepolymer solution onto the PDMS device, the textured PDMS surface was first plasma treated and then incubated in 5% acrylate-PEG-silane 10k (creating PEGWorks) for 2 hours. Then, 100 μm PEGDA hydrogel solution was pipetted onto the PDMS and covered with a spacer to maintain a uniform gel thickness of 100 μm. The hydrogel solution was finally cured in a nitrogen chamber for 5 minutes. The entire procedure was conducted inside a nitrogen chamber to prevent PEGDA oxygen inhibition [39]. Finally, the device with the hydrogel was incubated with PBS for 5 hours and washed several times to remove the porogen and create porosity in the hydrogel.

### 1.2.4 Hydrogel Bonding Test

To test the adhesion of the hydrogel on PDMS, we designed a 3D printed support for the device. Then, we attached the device with the hydrogel facing down and placed the apparatus in a beaker full of water with a magnetic stir bar. The water was stirred at specified RPMs (rotations per minute) as verified by an optical tachometer. Membrane shearing was observed by eye, and the RPMs at which shearing occurred were recorded.

### 1.2.5 Cell Culture

Beta TC6 (ATCC) cells were cultured in high glucose Dulbecco's modified Eagle's medium (DMEM) (4500 mg/l glucose) with 15% heat inactivate fetal bovine serum (FBS) inside a cell culture incubator. To culture inside the microfluidics, $1.5\times10^7$ Beta TC6 cells were loaded onto the device with 2 mL of medium without glucose. The device was incubated for 24 hours prior to the start of experiments to allow Beta TC6 cells to reacclimatize to normal glucose levels before stimulation. During the microfluidic experiments, the media was replaced with Krebs-Ringer buffer (Boston Bioproducts) containing 129 mM sodium chloride, 5 mM sodium bicarbonate, 4.7 mM potassium chloride, 1.2 mM potassium phosphate monobasic, 1.2 mM calcium chloride, 1.2 mM magnesium sulfate, 1.2 mM heptahydrate and 10 mM HEPES.

### 1.2.6 Oxygen Gradient Application

After 24 hours of culturing, cells in the microfluidics device were washed with no glucose Krebs-Ringer and moved to an on-stage incubator on a microscope. Nitrogen and oxygen gas supplies were then connected to the device and adjusted to 18.30 sccm and 7.14 sccm flow rates, respectively. The cells were incubated for 10 minutes to allow the gradient to stabilize, and then the experimental protocol described below was applied.

### 1.2.7 Glucose Stimulation

For glucose stimulation experiments, cells were then stained with 5 μM Fura-2AM for 10 minutes. The dye was replaced by no glucose Krebs-Ringer, and cells were then imaged for 10 minutes of incubation; then, cells were exposed to 1 mM, 2 mM, or 3 mM glucose-spiked Krebs-

Ringer buffers and recorded for another 25 minutes. Finally, the cells were washed with buffer without glucose and recorded for another 10 more minutes.

### 1.2.8 Insulin Detection

The sensor optimizations were completed without cell culture in the device. After curing under UV light for 5 minutes, the PEGDA hydrogel was washed for 5 hours to remove the porogen. The device was incubated with 3% BSA (Sigma) buffer to prevent protein absorption in PDMS and washed with PBS. Then, the sensor was incubated with different concentrations of insulin for various durations. After the insulin incubation, the device was washed with TBST buffer, and then the insulin reporter antibody (mouse anti-human with Alexa 594, R&D Systems) was incubated for different durations. For the optimization of insulin and reporter incubation times, the reporter antibody was diluted at 1:1000. The optimized incubation times were used for later experiments. For the optimization of anti-insulin in the hydrogel and detectivity assay, the reporter antibody was diluted 1:500. All subsequent cell-based experiments were performed with the same reporter antibody dilution.

### 1.2.9 Mitochondrial ATP Imaging

ATP live cell fluorescence dye (BioTracker) was used to measure the ATP levels in the mitochondria of Beta TC6 cells. After 24 hours of incubation in the microfluidic device, the glucose-free medium was removed and replaced with 2 mL Krebs-Ringer buffer containing 5 μM BioTracker dye for 15 minutes, followed by washing with no glucose Krebs-Ringer buffer. Cells in the device were imaged for 10 minutes. Then, the buffer was replaced by Krebs-Ringer with 3

mM glucose for stimulation and recorded for the next 25 minutes. Finally, the glucose buffer was replaced with buffer without glucose and recorded for another 10 minutes.

### 1.2.10 Imaging

All images were taken using an Olympus IX75 microscope. All images were at 10× magnification. An approximately 7.5×1 mm slice of the symmetrical gradient was recorded for calcium, ATP, and insulin quantifications using the automated X/Y stage to generate image collages. Each slice contained 13156×2556 pixels or 33 Megapixels. Forty-five timepoints at 1 minute intervals were recorded before, during and after the glucose stimulation bolus.

### 1.2.11 Calcium and Insulin Analysis

To calculate the fluorescence ratios for insulin detection, we used Olympus Cellsense software. An $8\times10^5$ $\mu m^2$ area was selected to calculate an average fluorescence intensity. The background image was measured by calculating the average intensity of the area without hydrogel. The ratio was then measured as the intensity divided by the background intensity.

The Fura ratio was calculated as the intensity of the 340 nm channel divided by the intensity of the 380 nm channel. The measurement process was the same for the insulin measurement. An $8\times10^5$ $\mu m^2$ area with cells was selected per measurement and tracked over the time points. The resultant time profile was leveled by removing the trend line as defined by the initial and end points.

### 1.2.12 Temporal Analysis via FFT

Processed Fura ratio images were imported into MATLAB. Twenty-five time points corresponding to the glucose stimulation pulses were cropped and used for the analysis. The initial time point was also removed to account for overshoot anomalies seen in supplementary data S3. The resultant image series contained 13156 by 2556 pixels for each time point, resulting in a total of 33 Megapixel datasets. A per-pixel fast Fourier transform was applied across the time points. The absolute magnitude of the transform was used to calculate a nominal center of gravity frequency and replotted in the processed image. The processed image was normalized to show the frequency peaks seen at approximately 12% oxygen. Subsequently, the averaged frequency versus the gradient axis (13156 pixel axis) was calculated and plotted as a summary of the 12% peak frequency.

### 1.2.13 Live Dead Assay

Cell viability was determined by a Live and Dead Cell Assay (Abcam). After the cells were attached to the device for 0, 6, 12, and 24 hours, they were washed with PBS, and 5X diluted live and dead dye in PBS was added to the device. After 10 minutes of incubation, the device was put under a fluorescence microscope for imaging.

### 1.2.14 Statistical Analysis

All the evaluations of statistical significance were performed using unpaired two-tailed Student's t test; *$p<0.05$, **$p<0.01$, and ***$p<0.001$. Figures with stars for statistical significance were plotted using the MATLAB Superbar function.2.

## 1.3 Results

### 1.3.1 Surface Modifications Improved Hydrogel Adhesion

Although the hydrogel biosensor was not exposed to external mechanical forces, it acted as a substrate for cell seeding and was subject to handling and fluid exchanges during cell culturing. Direct placement of the gel on PDMS resulted in gel delamination and lift-off from the surfaces, causing uneven spots in the spatial biosensing. To address these issues, both chemical and topological—i.e., silanization and texturization—modifications were employed: PEG chains were attached directly to the exposed PDMS hydroxyl groups via silanization. Microtexture dimples with increasing numbers of sides—triangle, square, and star—were patterned. These increased the cross-sectional bonding surface by 16.8%, 25.7%, and 32.9%, respectively (Figure 1-2A). Both modifications contributed to the strength of adhesion between the hydrogel and PDMS.

To quantify the adhesion, a fluidic shear apparatus was devised via 3D printing. The apparatus was submerged in water, and a standard stir plate was employed to create rotational shear against the hydrogel mounted inversely atop the apparatus (Figure 1-2B). At a specified angular rotation ω, the fluid velocity $u$ at the projected perimeter of the hydrogel was calculated. This velocity decreased toward the hydrogel surface, where the no-slip condition was assumed. With the slope of this velocity profile, $\frac{\partial u}{\partial h}$, and a given viscosity, e.g., $\mu_{water}$, the shear stress experienced by the hydrogel edge was calculated. The angular rotation ω at which the hydrogel delaminated was recorded for unmodified hydrogel, silanized hydrogel, textured hydrogel, and texture + silanized hydrogel preparations (Figure 1-2C). Silanization alone improved the attachment over unmodified hydrogel (baseline at 125 rpm or 1.3 mPa). Texturization increased hydrogel adhesion across geometries. Moreover, texture + silanized hydrogels showed a significant increase over

texturization alone, with additional increases from triangle to square textures. With the star geometry, no delamination was observed at the highest stir plate rotation (1200 rpm), suggesting that even greater shear stress could be tolerated. Hence, silane-modified, star-textured hydrogel bonding was selected for all subsequent experiments.

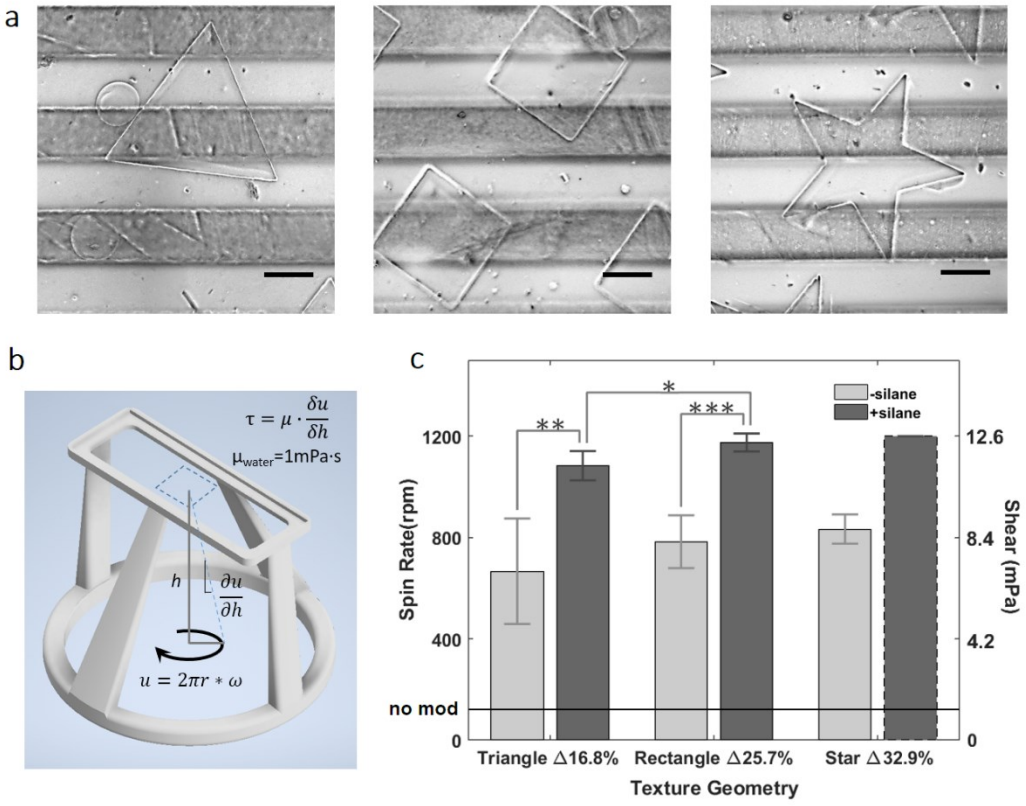


Figure 1-2. Hydrogel adhesion characterized via fluidic shearing. A. Microtextures were employed to increase the bonding areas in addition to chemical surface modifications. From left to right, triangular, square, and star-shaped dimples were micropatterned at 100 μm depths on the PDMS membrane atop the gas microchannels. The increase in the number of sides of these microstructures increased the cross-sectional contact areas by 16.8%, 25.7%, and 32.9%, respectively, resulting in stronger hydrogel bonding (scale bars denote 200 μm). B. To quantify the improved hydrogel adhesion, a fluidic shearing apparatus was designed and 3D printed in polylactic acid (PLA). The apparatus positioned hydrogel integrated devices upside down in a beaker of water, exposing the gel to rotational shear produced by a stir bar atop a stir plate. The angular rate of rotation translated to the linear speed at the edge of the hydrogel can be projected to the gel surface to define a shear stress τ. When the shear stress reaches the limit of gel adhesion, delamination is observed, and the rotational rate and shear stress are recorded. C. The unmodified hydrogel ("no mod") provided a baseline for comparison to enhanced bonding. Significant increases were found when both silane and microtexture were used together, with rectangular and star shapes topping the measurable stress at 12.6 mPa. Please note that the star-shaped membrane exceeded the stir plate speed of 1200 rpm and never showed delamination. Increases in cross-sectional area as percentages were noted for each shape. *p<0.05, **p<0.01, and ***p<0.001.

### 1.3.2 Optimized Porous Hydrogel Spatial Insulin Detection

The 100 μm PEG hydrogel covered the entire 1.5×1.5 cm cell culture area to provide spatial detection of insulin secretion on top of the oxygen gradient. The hydrogel provided enhanced by porosity to enhance molecular transport [37, 38]. The integrated insulin immunodetection was optimized for assay speed and sensitivity. By measuring the fluorescence ratio, i.e., signal to background fluorescence, the optimal capture antibody concentration was found to be 200 pg/mL (Figure 1-3A). The target insulin and final reporter incubation times were optimized at 30 and 60 minutes, respectively, beyond which no further improvements were seen (Figure 1-3B, C). Profiling concentrations from 50-1000 pg/mL resulted in the detectivity curve shown in Figure 3d, with a calculated limit of detection of approximately 25 pg/mL (Figure 1-3D). This limit of detection is half of what is typical for insulin ELISA kits (~50 pg/mL) yet allows spatial readouts in tandem with the oxygen gradient. This improvement is typical of what we achieved using porous hydrogels for other biomolecular detection methods.

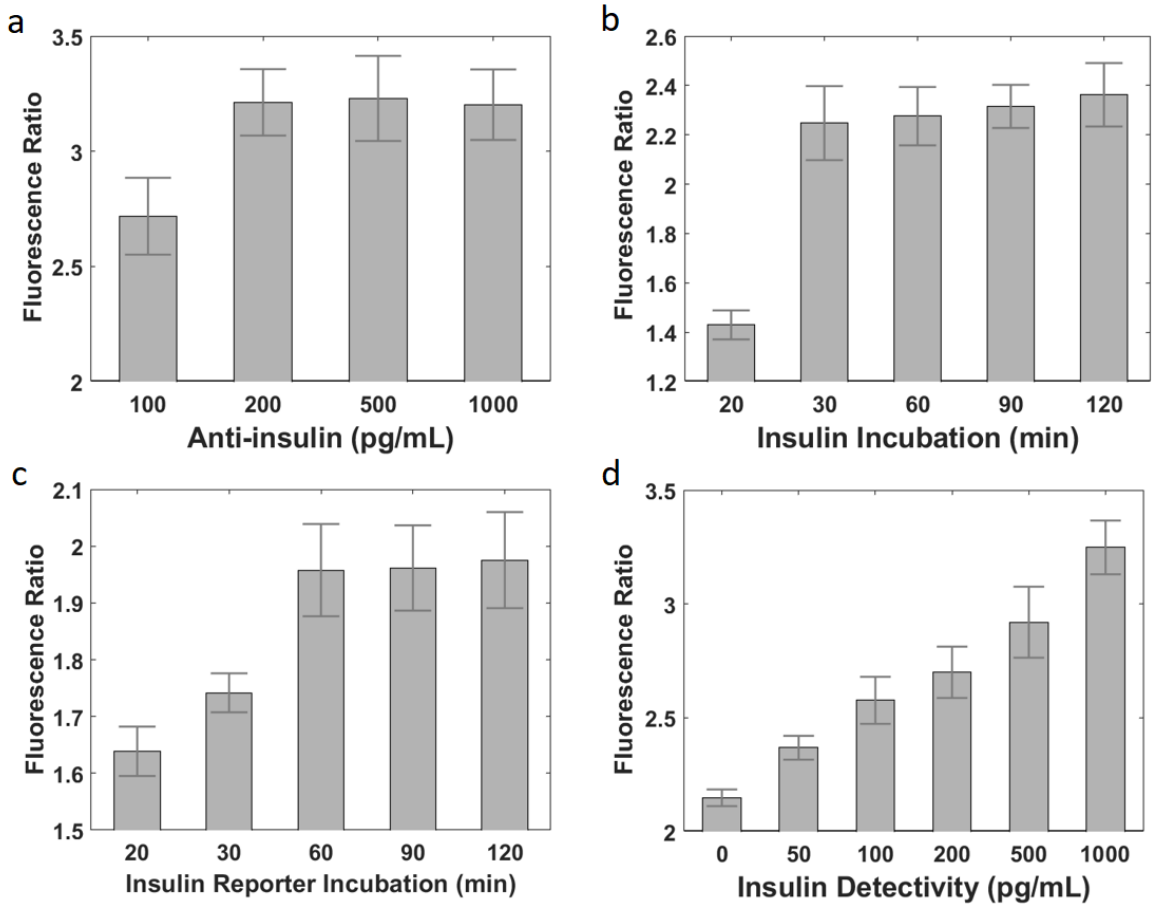


Figure 1-3. The optimized spatial insulin sensor achieved a 25 pg/mL limit of detection. The assay was optimized by using the fluorescence ratio as the readout, where the signal intensity was divided by the background fluorescence in the hydrogel. A. The amount of capture antibody was tested in the porous hydrogel by varying the concentrations from 100 to 1000 pg/mL. Treatment with capture antibody at excess of 200 pg/mL resulted in no observed significant increase in the fluorescence ratio. B. Next, the incubation time for target insulin was tested from 20 to 120 minutes. The incubation time was markedly improved compared to that of conventional assays at 30 minutes. C. Then, the reporter antibody incubation was tested, and the optimal time was 60 minutes. D. Finally, a detectivity curve from 50 to 1000 pg/mL was assayed to determine the limit of detection. Using the convention of twice the standard deviation of the blank sample, the insulin limit of detection in our spatial sensor was 25 pg/mL.

### 1.3.3 Simultaneous Detection of Calcium and Insulin in Beta TC6

We quantified beta cell calcium and insulin responses to glucose stimulation under normoxic conditions using Fura-2 and the integrated hydrogel sensor. Beta TC6 cells were cultured on the

surface of the 100 μm sensor hydrogel. The RGD group copolymerized in the hydrogel enabled the attachment of beta cells. After culturing beta cells without glucose for 24 hours, we stimulated them using Krebs-Ringer buffer spiked with different glucose concentrations: 1 mM, 2 mM and 3 mM [40]. The Fura-2 ratio of 340 nm to 380 nm intensities increased with increasing glucose concentration from 1 mM to 3 mM. Here, Fura signals were sampled at 15 s intervals, showing cyclic oscillations at 3 mM stimulation (Figure 1-4A). The 3 mM glucose group also exhibited a significantly higher Fura ratio than the 1 mM glucose group (Figure 1-4B). Using the integrated hydrogel sensor, we measured 2.36 pg/mL insulin for the 1 mM glucose stimulation, 72.0 pg/mL insulin for the 2 mM glucose stimulation, and 373 pg/mL insulin for the 3 mM glucose stimulation (Figure 1-4C). The insulin response showed a linear increase with higher glucose concentrations (Figure 1-4D). As the 3 mM stimulation exhibited the most robust calcium and insulin responses, all subsequent experiments were performed using this glucose concentration.

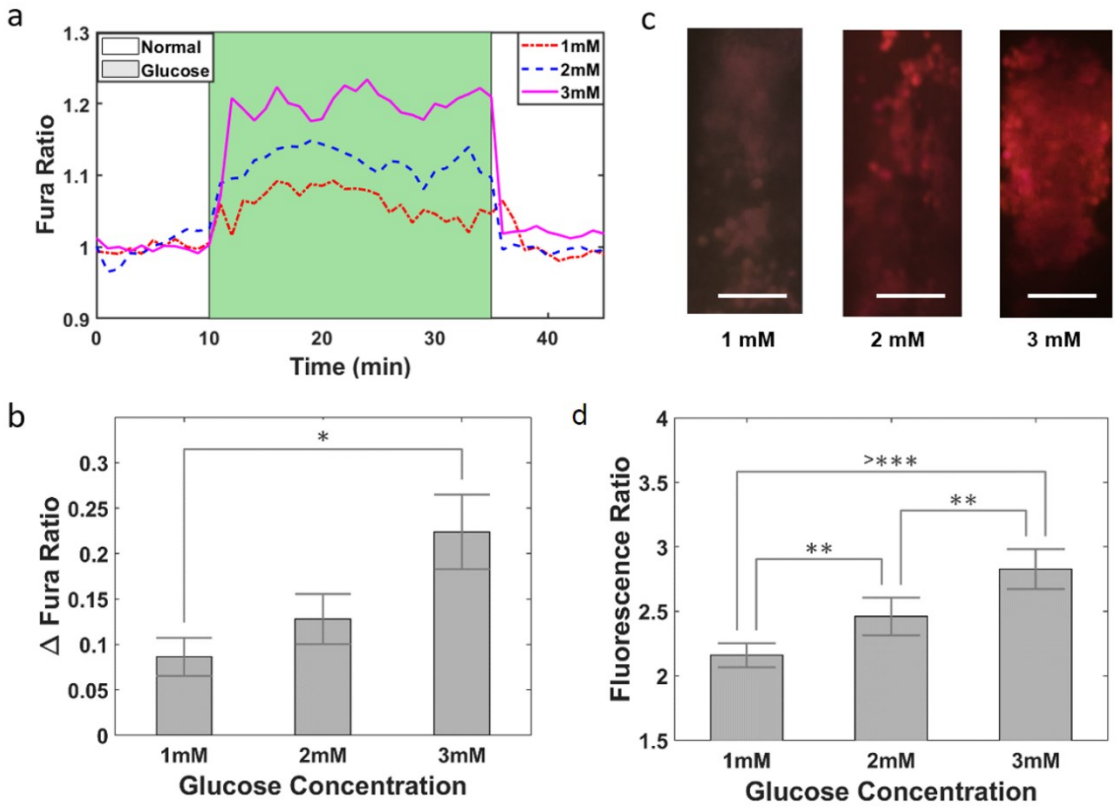


Figure 1-4. Simultaneous detection of calcium and insulin in beta TC6 cells. The microfluidic platform was first tested for GSIR under normoxic conditions at a single location without spatial oxygen gradients. Boluses of 1 to 3 mM glucose were injected into the aqueous reservoir during observation via microscopy for 25 minutes before flushing with Krebs-Ringer buffer to return to baseline. Intracellular calcium was monitored using Fura-2 AM dye, while insulin release was detected using the hydrogel assay. A. Beta TC6 cells responded to glucose stimuli and demonstrated intracellular calcium flux, with 3 mM resulting in the highest Fura measurements. Here, Fura was sampled at 15 s intervals. At this sampling rate, cyclic oscillation was observed at the 3 mM concentration. However, at lower concentrations, the noise averaged out the oscillations. B. The change in the Fura ratio from baseline to peak was plotted for the three concentrations. Significant increases were seen in 3 mM over 1 mM stimulation. C. Corresponding fluorescence micrographs on the right show increased insulin detection with increasing glucose stimulation. (scale bar denotes 100 μm). D. Insulin release detected using the built-in sensor demonstrated significant increases at all concentrations. * $p<0.05$, ** $p<0.01$, and *** $p<0.001$.

### 1.3.4 Spatial Gradient With In Situ Calcium, Insulin, and ATP Detection

To study the effect of different oxygen concentrations on GSIR, we applied microfluidic spatial oxygen gradients to Beta TC6 cells. Leveraging the device's symmetry, we acquired half of the

gradient using a 2×12 frame microscopy collage at 10× magnification and then analyzed eleven positions within the 0-20% oxygen range (Figure 1-5A). Calcium flux and insulin release were quantified at 1-minute time intervals for 46 minutes. In response to 3 mM glucose boluses, the Fura ratio difference did not change much between 0% and 10% oxygen concentrations. For concentrations higher than 10%, the ratio increased with increasing oxygen concentration (Figure 1-5B). From 0% to 10% oxygen, insulin secretion increased slowly from 1.17 pg/mL to 39.8 pg/mL. At 12% oxygen, however, insulin secretion jumped significantly, $p=0.057$, and subsequently rose from 98.31 pg/mL to 641.68 pg/mL from 12 to 20%, Figure 1-5C. These results were consistent with our previous findings of a significant impairment of GSIR in whole islets under 10% oxygen [12, 13]. In addition, the mitochondrial ATP response rose between 0-6% oxygen concentrations and then dipped in the same 8-12% oxygen range, followed by a recovery toward 20% oxygen (Figure 1-5D). The results showed that Beta TC6 cells did mount a modest ATP response in the presence of glucose stimulation compared to other beta cell lines. The results also suggested that the changes from 8-12% are related to metabolic activities, with no visible changes to the static magnitudes of calcium responses. This prompted our investigations of calcium oscillations using Fourier analysis (see the next section).

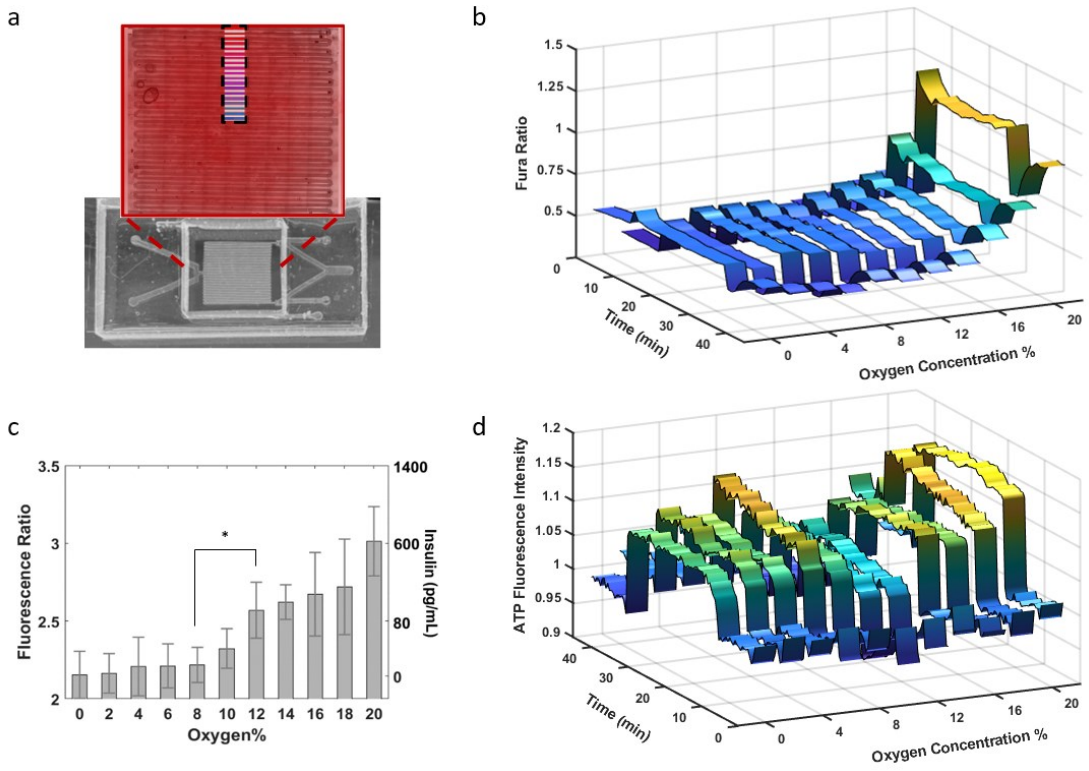


Figure 1-5. Oxygen gradient stimulation with spatiotemporal detection. A. Eleven positions within the oxygen gradient were selected as regions of interest for calcium, ATP, and insulin responses. B. Fura ratios for oxygen concentrations were recorded at 1-minute intervals for 46 time points. The Fura ratios remained relatively low until above 10%, where they increased with increasing oxygen. The observed transient oscillations suggested nuances to calcium signaling, which led to subsequent Fourier analysis. Note that this 1-minute sampling was significantly slower than the 15 s acquisition that we achieved for the fixed location, single oxygen imaging in the previous figure. Thus, these results could potentially underestimate actual calcium oscillations. C. Insulin secretion was quantified via a built-in sensor. A jump occurred at oxygen levels of approximately 8-12% (*p=0.057). D. Mitochondrial ATP was quantified via fluorescence labeling, showing modest increases until the same 8-12% oxygen range, where the response dipped before rising again near 20%. These results suggested that Beta TC6 cells did mount ATP responses to glucose. These responses exhibited a transition between 8-12% oxygen that may be related to changes in metabolites.

### 1.3.5 Oxygen Modulation of Calcium Dynamics Revealed by Spatiotemporal Imaging

A difference in calcium oscillation was observed near the 8-10% range of the oxygen gradient (Figure 1-5B). To further quantify this change in calcium dynamics, frequency analysis was

applied to the series of time-lapse images. To reduce the data size and the time of calculation, a 33 megapixel area over 24 time points (duration of GSIR pulse) was used for analysis (Figure 1-6A). A Fourier transform was applied, and a nominal frequency value (center of gravity of spectrum) was calculated for each pixel. The resultant image revealed a dependence on the underlying oxygen gradient, where a higher intensity corresponded to higher oscillation frequencies (Figure 1-6B). A region near 12% oxygen showed brighter intensities than the surrounding concentrations. The data were replotted by averaging across the image to provide a modulation versus oxygen profile (Figure 1-6C). In this profile, a peak frequency of 13.5 oscillations per hour was observed at 12% oxygen. This oscillation was equivalent to 4.4 minutes per cycle, which is comparable to reported values for whole islets and single beta cells at 4 to 5 minutes per cycle. This calcium modulation was consistent with the insulin jump and ATP dip that occurred in the same 10-12% region (Figure 1-5). These data suggest that oxygen plays a key role for both the metabolic and electronic components in the dual oscillator model (Figure 1-6D). Certain levels of oxygen represent a balance between these two components via ATP-related metabolites. We note that the overshoots of the calcium pulses were not included in this analysis, as they presented an asymmetrical artifact near 0% oxygen not seen in the adjacent corner.

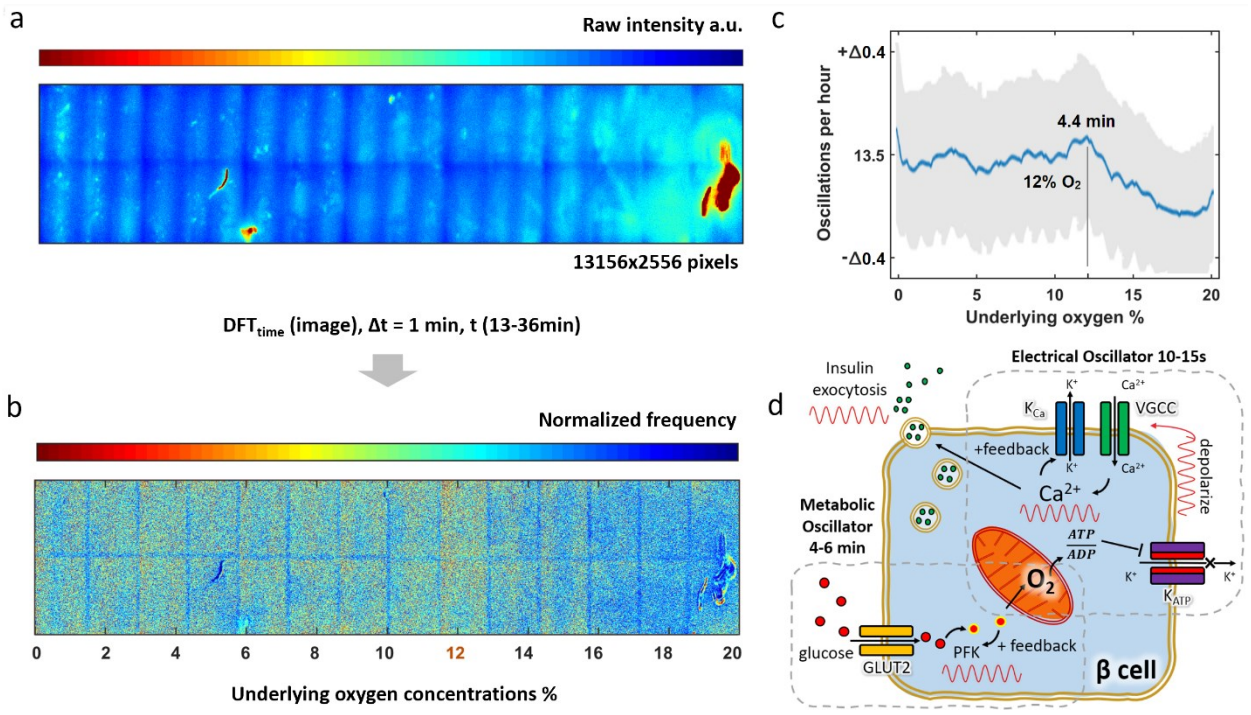


Figure 1-6. The specific oxygen level increased the frequency of calcium oscillations. a section of the symmetric oxygen gradient was acquired using stage scanning fluorescence microscopy, encompassing a 0-20% gradient as characterized earlier. A. The resultant raw intensity image has 13156x2556 pixels from the collage, or 33 Megapixels total per image. Artifacts visible in these images were removed prior to analysis. Collage images were acquired at 1-minute intervals for 46 minutes. Only time points corresponding to glucose boluses were used, giving 24 points from 13-36 minutes. The initial overshoot at 12 minutes was removed to reduce artifacts (see supplementary data S3). B. A per-pixel time-based Fourier transform was applied, and the magnitude profile was weighed at the center of gravity, giving a nominal frequency value for each pixel. The result was replotted to show this frequency versus underlying oxygen concentrations, where an intense region approximately 12% oxygen was observed (visible banding seen in collage was due to image stitching). C. The pixels were averaged and flattened vertically to show a frequency profile versus oxygen concentrations. The resultant profile showed a peak oscillation at 12% oxygen. This oxygen level is neither hypoxic nor normoxic in the standard cell culture sense. D. A conventional dual oscillator model for calcium includes both electrical and metabolic components. Feedback in the PFK portion of glycolysis is viewed as the center of metabolic oscillation, whereas calcium channel feedback is viewed as the center for electrical oscillations. Oxygen, due to its effect on the mitochondria, could be a key factor in both oscillator components.

## 1.4 Discussion

### 1.4.1 Enhanced Platform With Gradient-Based Multimodal Biosensing

We have created a platform for gradient-based multimodal biosensing enabling modulation of both oxygen and aqueous factors on beta cell cultures. The technique employed a custom rotational fluid shear apparatus for assessing gel adhesion on PDMS (Figure 1-2B). Compared to conventional atomic force microscopy or mechanical shearing tests, the 3D printed device is easy to apply on stir plates and enables simple calculation of shear forces. The fluidic-based test is also compatible with cell-laden hydrogels and is applicable to numerous shear-dependent cellular studies. Using the multimodal gradient, we demonstrated spatial insulin sensing with a lower detection limit than conventional single point ELISA kits for 0-20% oxygen concentrations across an entire cell culture (Figure 1-3D). The improved detection can be attributed to the hydrogel porosity and the direct path of insulin from the cell to the sensor. The platform also allows monitoring of calcium and mitochondrial ATP levels *in situ*, which revealed interesting dynamics at approximately 10% oxygen levels, as reported earlier [18, 19]. Although the mechanisms of these dynamics are still unclear, our results suggest that they are related to changes in the levels of metabolites.

### 1.4.2 Oxygen Modulation of GSIR Dynamics

By examining the spatiotemporal data from islets exposed to oxygen gradients, we observed a distinction between the effects on calcium transients versus the effects on insulin secretions. Unlike the optimal modulation of calcium transients (Figure 1-6C), there was no optimal or peak

insulin at the center of the gradient. Nevertheless, a discontinuity was seen at the same 12% oxygen level for insulin (Figure 1-5C). We attribute the difference between insulin and calcium dynamics to the 2D, planar cell culture employed. For planar beta cells, glucose concentration is readily available and independent from specific oxygen concentrations. In 3D constructs and devascularized islets, both hypoxia and glucose diffusion overlap in a descending gradient toward the center of the microtissue. Our observation is yet another potential difference between 2D and 3D tissue structures.

Moreover, the observed oxygen effect appears to target GSIR oscillations. The current model of GSIR oscillations involves two components, as shown in Figure 6d. In the slower metabolic component (3-6 minute durations), phosphofructose kinase (PFK) feedback [23, 28-30, 41, 42] drives oscillatory mitochondrial ATP production. In the faster electrical component (10 seconds), membrane channel feedbacks modulate intracellular calcium flux [23, 27, 28, 43-46]. A rise in intracellular calcium requires ATP pumps to recover, and ATP depletion then promotes PFK feedback in the metabolic component of the model [23, 47]. As this dual oscillator model involves mitochondrial metabolism, oxygen consumption is also modulated [23, 32, 34]. Given this model, one potential mechanism of the observed oxygen effect is the limit on aerobic respiration, which shuts off the electron transport chain and promotes glycolysis and PFK feedback [33]. In comparison, our results showed that 8-12% hypoxia resulted in a decrease in mitochondrial ATP with a modest increase in the frequency of calcium oscillations. This is consistent with experiments in which a decrease in metabolic activity enhances cell networking and calcium oscillations via glycolytic effects on mitochondrial metabolism [36]. Furthermore, the dual oscillator model can also reproduce fast calcium oscillations when glycolysis is stationary [23, 48]. The observed oxygen modulation of calcium could simply represent a dynamic balance between glycolysis and

aerobic respiration. A second potential mechanism is the direct hypoxic modification of $K_{ATP}$ channels and ion balance. This mechanism is observed in ischemia-reperfusion of tissue [49, 50] and our previous results in islet preconditioning [18].

Another consideration is the difference in GSIR oscillations between whole islets versus single beta cells, where the latter is dominated by the slower metabolic component [23, 44]. Although our cell culture conditions allow calcium and metabolites to distribute spatially across clusters of cells, we observed mostly slower oscillations related to the metabolic component of the model. The faster electrical component could simply be too weak and/or too sensitive [28, 51] to be observed by our minute-scaled spatial imaging compared to our faster fixed location, single oxygen results. Nevertheless, our data suggest that oxygen modulation of glucose-insulin oscillations occurs across the cell culture.

### 1.4.3 Implications in Studying Islet Pathogenesis and Improving Islet Therapies

We note that there is a distinction between cell culture and physiological oxygen levels; atmospheric oxygen is 21%, whereas physiological blood oxygen is 10-13% (75-100 mmHg), and pancreatic tissue oxygen level is ~5.6% (40 mmHg) [52-55]. In earlier islet therapies, the hepatic portal vein was used as the transplant site (<2% $O_2$ 5-15 mmHg), and those transplanted grafts suffered from hypoxia and shortened graft survival, which is associated with only 30-45% long-term insulin impendence [56-58]. Current research has been focused on improving islet hypoxia via hydrogel substrates, vascular grafts, novel transplant sites, and stem cell-derived islets. However, the specific effects of oxygen levels on GSIR are still unclear. Both our previous islet hypoxia study and the results in this work suggest a transitional oxygen level of 10-12%. This level of oxygen is higher than that in islets *in vivo*, and the difference may be due to the dense

vascularization and convective transport of oxygen in the native pancreas versus the diffusion-limited transport in our cell culture devices. Nevertheless, the observed optimal oxygen level of 12% for calcium oscillation goes against the conventional view of a linear relationship between hypoxia and GSIR. Further studies on oxygen consumption rates, calcium flux, and intracellular metabolite levels could aid in interpreting this observed difference.

Additionally, future mechanistic studies could clarify the pathways affected by oxygen. Channel blocking or $K_{ATP}$ knockout models can target the electronic oscillation pathway under different oxygen level conditions. Glucose starvation, oxygen consumption rates, and glycolysis tagging can target the metabolic oscillation pathway with different oxygen levels. Last, we have yet to explore the phase portion of our Fourier-based image analysis. This means that future studies comparing both pathways can be aided by phase maps to visualize the potential synchronization of adjacent beta cells, similar to what has been done in network analysis of GSIR [59-62]. Differential synchronization between faster electronic and slower metabolic oscillators can lead to a number of observed calcium response profiles [23], with oxygen as a key controller in these processes.

In addition to the understanding of tissue hypoxia on islets, our results also suggest new strategies for improving islet therapies in the future. Our previous work leveraged microfluidics to improve islet selection for transplants. We have also demonstrated islet preconditioning to hypoxia [18]. Similarly, gradient modulation of calcium oscillation can precondition, or in this case, train naïve β-cells or stem cell-derived islets to synchronize their GSIR for a more responsive replacement tissue. This training strategy can be applied at oxygen levels determined per tissue sample and monitored by calcium imaging and network analysis. The goal would be to potentially

improve the glucose sensitivity and magnitude of insulin secretion toward better islet therapy outcomes.

There is a limit in interpreting our cell culture results for native islet tissue. Beta cells in native islets are well vascularized and capable of cell-to-cell contact in all directions via gap junctions. Although our Beta TC6 cell culture also exhibits clusters that resemble tissue spheroids, synchronization of their calcium waves is probably inferior to that of the native islet construct. Nevertheless, this means native islets should see a more pronounced effect in the oxygen modulation of calcium oscillations, as we observed. It would be interesting and important to extend our oxygen modulation technique to whole islets for comparison in the future.

## 1.5 Conclusion

The work was performed to create a robust multimodal gradient device to study β-cells under oxygen gradients. The realized microfluidic platform incorporated sensitive, spatial detection of insulin secretion in situ with an oxygen gradient. Using microfluidics, a peak calcium oscillation was observed at the 10-12% oxygen level, accompanied by a dip in mitochondrial ATP and a jump in insulin secretion. The evidence of an optimal oxygen level that is neither hypoxic nor normoxic counters the conventional view of a linear hypoxia relationship. Furthermore, the findings suggest oxygen to be a key parameter to balance the components within the dual oscillator model of GSIR but also raise further questions on the role that oxygen plays in either calcium channel modifications or metabolite modulations. The microfluidic technique enables experimental protocols to further answer these questions and provides a platform to apply training strategies for islet therapies. Furthermore, the technique for 3D fluid shear stress can provide a facile hydrogel

adhesion test for biomaterial applications. Last, spatiotemporal analysis via time-based Fourier analysis can be applied to monitor growth factors, cytokines, and other secretory biomolecules to improve the visualization of molecular transport and gradients.

To study the cell-to-cell contact in diabetes, we must develop a compatible microfluidic platform to enable cross reactions between cells. To achieve that, we will need a powerful microfluidic pump, so that the cells can be introduced to the medium and allow the cross activities between different cells.

This work was submitted to peer-review journal Microsystems & Nanoengineering. Refer as "Duan, K., Zhou, M., Wang, Y., Oberholzer, J., & Lo, J. F. *Visualizing hypoxic modulation of beta cell secretions via a sensor augmented oxygen gradient.* Microsystems & Nanoengineering, 2023. 9(1), 14."

# Chapter 2. Reducing Shear Effects on Islet Beta Cells Driven by an Optimize μTesla Pump

## 2.1 Introduction

Mammalian cells are sensitive to mechanical and shear forces. In the past few decades, the exploration of cell biomechanics has led to several approaches for stimulations [63-67]. Specifically, shear stress is a key biomechanical stimulation in cells exposed to flow. For example, shear regulates vascular endothelial phenotypes and induce polarity in endothelial cells [68]. Interstitial shear stress and blood shear stress is a regulator of tumor cell adhesion and extravasation [69]. Broadly speaking, shear affects cells morphology [70], proliferation [71], differentiation [72], metabolism [73], and many other cellular processes [74]. Therefore, disease models that study cell responses to microenvironments should include not only biomolecular, but also biomechanical cues. Current understanding of how cells sense shear stress involves calcium responses through two pathways: 1) perfusion related shear stress can enhance mass transfer of agonist to the cell surface, and 2) the exposure to shear stress increase the permeability of the cell membrane [75-77]. In the islet beta cells, cytoplasmic calcium concentration regulates cell metabolism, DNA/RNA transcription, proliferation, and insulin secretion [78-80]. Insulin

secretion start with the uptake of glucose into the cytoplasm and its metabolism to pyruvate [81, 82], followed by the citric acid cycle, which leads to oxidative phosphorylation and an increase in ATP/ADP ratio. ATP causes the closure of ATP-sensitive $K_{ATP}$ channels [83, 84], which depolarizes the voltage dependent calcium channels and trigger the influx of calcium. Finally, the intracellular calcium influx prompts the exocytosis of insulin granules [85, 86]. Shear-related calcium influx in islet beta cells is an unignorable part when doing diabetes related research.

Microfluidic technology has been widely used to mimic *in vivo* flow shear stress (FSS) conditions. Advantages of using microfluidics for FSS modeling include precise flow modulation, complex 3D geometry, long term cell culturing, and integration with real-time microscope [87-91]. A number of these microfluidic shear models have been realized to study biological phenomena, disease pathologies, and cell biology and clinical applications [92-96]. However, the lack of integrated microfluidic flow source hampers further development of FSS studies. Although conventional microfluidic flow sources such as the syringe pump, peristaltic pump, pressure-driven pump, gravity pump, and capillary pumps can control the flow rate at μL to nL per minute regimes, they are limited by dynamically changing velocities, pulsatile pressures, and small, fixed perfusion volumes  There have been recent advances in integrated pumps, like finger-actuated pumps, centrifugal pumps, accoustofluidic pumps, electroosmotic pumps, among others, [97-100]. However, the majority of these novel pumps are still unable to combine the steady constant velocity and continuous flow required for long term modeling of *in vivo* FSS physiologies.

To address these limitations, we leveraged our microTesla (μTesla) micropump to provide continuous, non-pulsatile, and recirculating flow designed for FSS modeling. Our previous μTesla version was a 2 cm device to demonstrate the ability of Nikola Tesla's turbine as a boundary layer pump for microfluidic flow. In this work, we taking advantage of higher resolution

stereolithography 3D printing to create µTesla-II, with a 10 mm rotor that is comprised of two circular discs with 1 mm gap in between. In addition to miniaturization, we investigated how surface textures can modulated the fluid adherence to the rotor, a fundamental working principle of the Tesla turbines [99].

We designed the µTesla-II rotor to operate with the Reynolds number in the laminar regime. During the rotation of the tesla rotor, the only velocity component of the fluid flow is towards the center to the exhaust port nozzle. The Reynolds number can be described by the following flow conditions:

$$\mathrm{Re} = \frac{\rho u D_h}{\mu}$$

Where $\rho$ is the density of fluid, $u$ is the flow velocity, $D_h$ is the hydraulic diameter.

The µTesla rotor was design to pumped outwards from the center to the side, based on this centrifuging action, the designed fluid flow rate $Q$ can be calculated by the equation:

$$Q = 2\rho r \int_0^{\hbar} u dx$$

Where r is the radius of the disk, $u$ is the velocity of fluids at axis surface. At our operating conditions of 4000 rpm and a target flow rate $Q$ of, we were able to keep $Re$ near 2000 range.

Furthermore, the Tesla rotor leverages the boundary layer effects of laminar flow between the parallel disks. In this study, the flow rate $Q$ was selected based on suitable ranges of stimulation for FSS modeling. We further optimized the boundary layer effects by modifying the µTesla-II pump surface textures. Texturized µTesla-II rotors were tested by pumping fluids in different viscosities, including shear thinning solutions to model blood rheology. Lastly, the µTesla-II was

compared to syringe pumps to shear islet beta cells in FSS experiments. We showed that µTesla-II avoided transient artefacts that were present in syringe pump driven islet beta cells, as seen in their calcium and ATP responses. These results provided further understanding of the mechanics of boundary layer pumps and their surface optimization, and further illustrated their importance in avoiding misleading results in FFS experiments.

## 2.2 Materials and Methods

### 2.2.1 Fabrication of the µTesla 2 Pump

The µTesla 2 pump rotor and housing model was designed using Auto CAD. A Stereolithography (SLP) based 3D printer (Phrozen 3D) with a voxel resolution of 50 µm was used to fabricate the pump rotor and housing. After the printing, two 1.6 mm thickness 1.6 mm outer diameter magnets were inserted into the rotor in a magnetic axis, then the rotor and housing were assembled together using glue gang to seal the pump and stabled at the center of a stir plate. The inlet and outlet were connected to tubes for the flow pumps.

### 2.2.2 Simple Texturization via Voxel Staircasing in 3D Printing

The 3D model design of the pump was sliced using Chitubox software at different angles with respect to the print axes. As the SLP printers have a finite voxel resolution 50µm, the slicing (without anti-aliasing) will create a staircasing or pixelation effect on the rotated surfaces of the µTesla-II rotors, giving us a simple modulation of the surface texture. Three different angles were tested at 0° to the axes featuring flat rotor surfaces, 22.5° with staircasing textures, and 45° with

diagonal staircasing textures. The surface topologies were characterized via profilometry (SurJet SJ-210, Mitutoyo) measurements along to the staircasing direction (Figure 2-1).

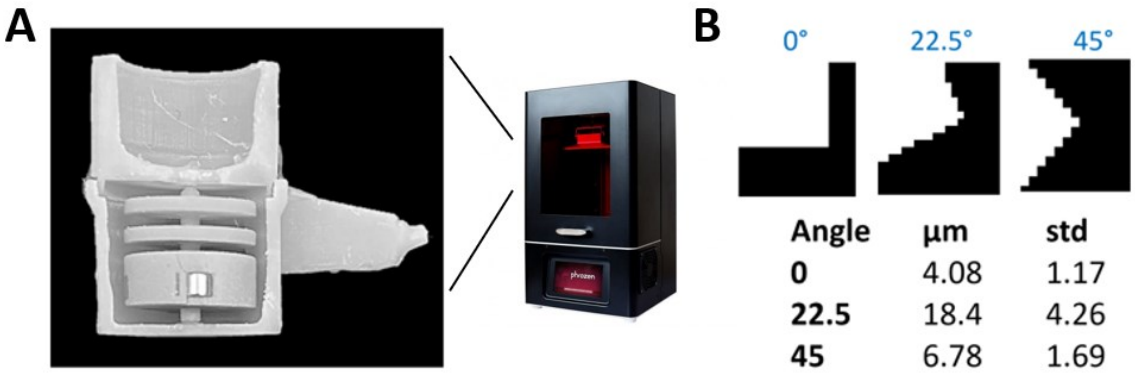


Figure 2-1. µTesla-II pumps design and fabrication. A. µTesla pump schematic picture. µTesla was fabricated by lithography-based 3D printer, the rotor has two magnets inserted to enable the rotation, the pump house has a top inlet chamber and a nozzle outlet. B. texture fabrication. Based on the fact that lithography-based 3D printing, print parts at a 50 µm resolution pixel, surface texture can be fabricated by placing the rotor at different angles at 0, 22.5° and 45°.

### 2.2.3 Illustrating Boundary Layer Modulation via Comsol Modeling

To illustrate our concept of how surface texture modulates the slip conditions at the boundary layer, we employed COMSOL Multiphysics to model the µTesla-II rotors. A 3D model of µTesla-II was generated in COMSOL software. The laminar flow module was selected to model the flow physics. The rotation was set to 4000 rpm, corresponding to actual physical experiments. To simplify the modeling setup, the fluid volume was rotated relative to the disk surfaces. A no-slip boundary was assumed at the disk surfaces and the resultant surface velocity profile, streamline, and pressure distribution were visualized in Figure 2-2.

### 2.2.4 Flow Velocimetry

The integrated microfluidic device was filled with PBS and operated at different rpm from 1200 to 4000. The device inlet was connected to a tube of PBS solution and the outlet was connected to a 15mL empty tube. By measuring the time for the pump to fill up the 15mL outlet tube, we can drive the pumping flow rate at different rpm. To calculate the flow velocity, 10μL fluorescent carboxylate-modified polystyrene latex beads (Sigma, USA) were dispersed in 2mL distilled water; the beads have an average size of 1 μm. Diluted beads solution was injected into the integrated pump for the experiments. The pump was then run at 1500 rpm which result in a flow rate around 50μL/min, fluorescent pictures were took at 100 ms exposure time inside the cell differentiation chamber. The flow velocity was calculated by measuring the travel distance divided the 100 ms exposure time.

### 2.2.5 μTesla Pumping at Different Viscosities

Aqueous glycerol viscosities were prepared from 1 to 9 cP, at 0-53.92% respectively. Pumps with different rotor textures were assembled and characterized via their output head pressures. First, isopropyl alcohol was used to wet the pump and remove air bubbles and voids inside the pump. Subsequently, the alcohol was replaced with different viscosities of glycerol solution. The heights of the solution columns were noted and kept constant to ensure similar hydrostatic pressures. The pump was then rotated at 4000 rpm to pump the glycerol solution through a 1/16" inner diameter Tygon tube placed vertical to quantify $\rho g \Delta h$ as a measure of head pressure.

### 2.2.6 Shear Thinning Measurement

To model the shear thinning behavior of biofluids such as blood, 0.0375% Xanthan gum solution was prepared. Fournier [101] states that blood will approach an asymptotic limit of approximately 3 cP at shear rates higher than 100 1/sec, and our xanthan formulation will mimic this trend. Lastly, we compared the head pressure of the μTesla-II rotors pumping xanthan versus 3cP glycerol solution for rotate rates from 400 to 4200 rpm.

### 2.2.7 μTesla 2 vs Syringe Pump Dye Clearance in Microchannels

A perfusion test was set up to characterize the dynamics of food dye clearance in microfluidic channels. First, we filled the channels of our standard droplet microfluidic devices with food dye. Then, we observed both μTesla pump and syringe pump (NE-300, New Era Pumps) driven devices under time-lapse microscopy for later image analysis. ImageJ (National Institute of Health) was used to calculate the transients of this color clearance based on the appropriate color channels.

### 2.2.8 Cell Shear Stress Test

Our standard microfluidic droplet device was fabricated using SU-8 photolithography and PDMS soft lithography [37, 38]. We selected this device for FSS demonstration despite it being designed for droplet generation as it is well-characterized in our previous work [102]. The 550 x 500 μm rectangular channels within the devices was coated with Poly L lysin to enable the cell attach in the channel. Two cell lines—Beta TC6 and INS1—were tested in this study, first, Beta TC6 cells and INS1 cells were cultured in the droplet microfluidic device with no-glucose medium for 12 hours. The medium was then removed prior to FSS experiments. All the experiments were

performed in Krebs-Ringer buffer (Boston Bioproducts), with 129mM sodium chloride, 5mM sodium bicarbonate, 4.7mM potassium chloride, 1.2mM potassium phosphate monobasic, 1.2mM calcium chloride, 1.2mM magnesium sulfate, 1.2mM heptahydrate and 10mM HEPES.

### 2.2.9 Calcium Influx Detection

For shear-dependent calcium responses, cells were incubated and stained with 5 μM Fura-2AM (Thermo Fisher) for 30 minutes, then replaced by no glucose Krebs-Ringer buffer. The devices were then placed under fluorescence microscopy and incubate for 5 minutes, followed by stimulation of glucose concentrations for another 10 minutes (3mM glucose solution for Beta TC6 cells, 20 mM glucose solution for Ins1 cells). Fura fluorescence intensities were measured at 340 and 380 nm wavelengths every 15 seconds. The ratio of 340/380 nm intensity was then calculated to represent intracellular calcium levels.

### 2.2.10 Mitochondrial ATP Tracking

We also looked at shear-dependent ATP responses as glucose metabolism and mitochondrial function is inherent in glucose-insulin secretions. First, cells were incubated and stained with 5 μM ATP fluorescence dye (Millipore Sigma) for 15 minutes then replaced by no-glucose Krebs-Ringer buffer. The devices were then placed under fluorescence microscopy and incubate for 5 minutes, followed by stimulation of glucose concentrations for another 10 minutes. Fluorescence images were taken every 15 seconds and the intensities overtime were plotted to show mitochondrial ATP activities.

## 2.3 Result and Discussion

### 2.3.1 Comsol Modeling

The modeling result showed that for water as a standard fluid, the maximum velocity at the outlet is 2m/s at 4000 rpm. This corresponds to a flow rate of 94mL/min, compared with our experimental results of 1 ml/min. Moreover, the velocity and streamline map matched our designed flow direction and distribution, where the velocity increased spirally from the center towards the circumference of the disc via centrifuging forces. On the disk surface, the fluid pressure also showed a concomitant increase from the center to circumference, with a relief of pressure near the nozzle outlet (Figure 2-2A). Please note that as the rotor is turned, a negative pressure was created near the center drawing in flow, while a rise toward positive pressure is achieved near the walls of the pump, consistent with the pump generating head pressure (Figure 2-2B).

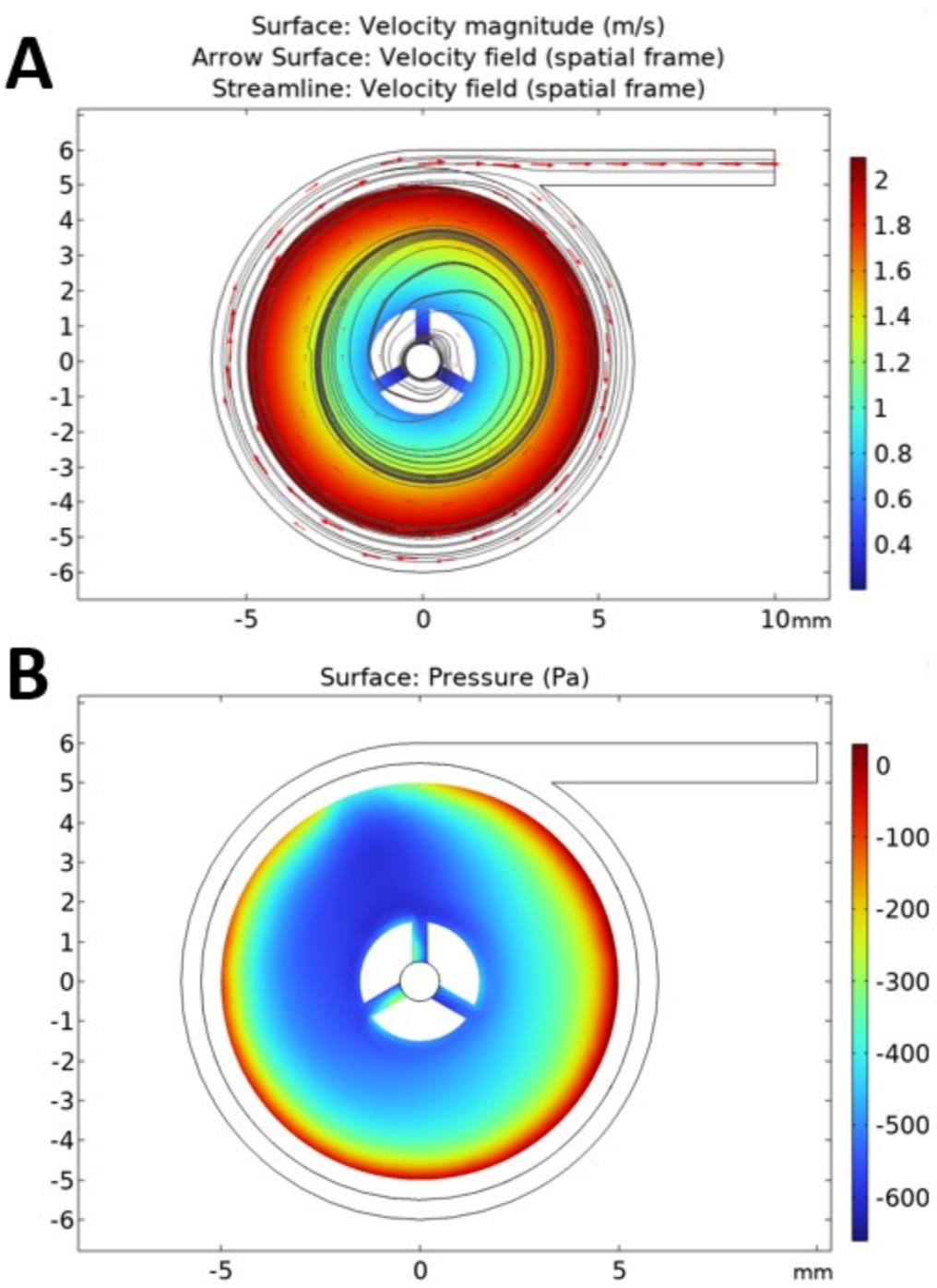


Figure 2-2. COMSOL simulation of rotor surface during rotating. A. Velocity field on the disk surface, the center has the lowest velocity, by the rotation of the rotor, velocity reaches maximum at the boundary. B. Pressure field on the disk surface. Pressure increased from the center to the boundary of the disk, release near the nozzle outlet.

### 2.3.2 Flow Velocimetry

Flow velocimetry was performed to compare the µTesla-II pump to peristaltic pump in maintaining laminar flow. The flow velocity profiles inside our standard microfluidic channel showed that when pumping via the µTesla-II pump, the velocity profile fit more closely to a parabolic curve (Figure 2-3) compared to pumping using a peristaltic pump. This is consistent with our results from µTesla pump version one [102].

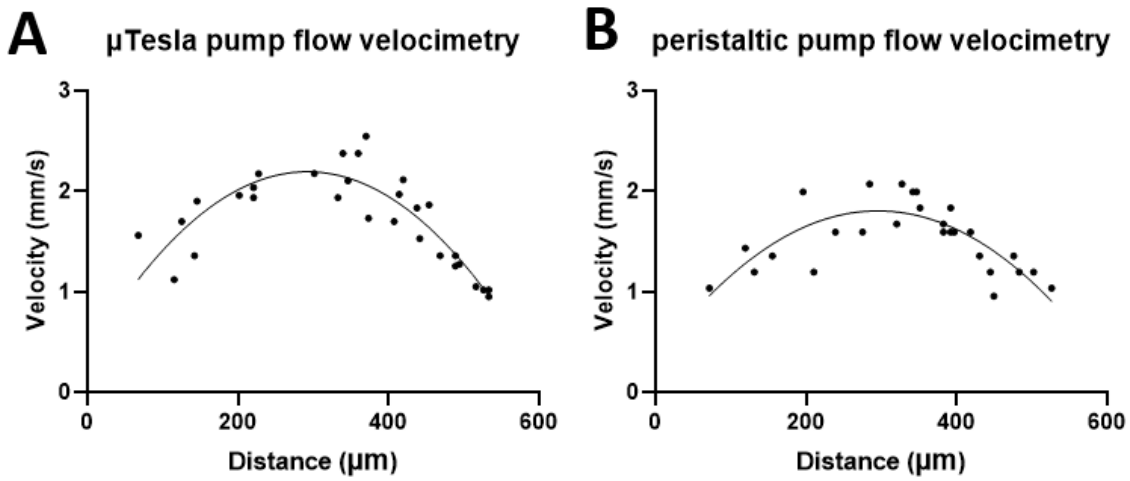


Figure 2-3. flow velocimetry inside microfluidic channels, µTesla-II pump vs peristaltic pump. A. µTesla pump flow profiles fit to a parabolic line and the R value is equal to 0.7705. B. peristaltic pump flow profiles fit to a parabolic line and the R value is equal to 0.6153.

### 2.3.3 µTesla Pump Surface Modification and Optimization

To better understand and test the modulation of the fluid-surface boundary layer effect within µTesla-II rotors, we modified the surface textures using voxel staircasing at various 3D printing angles. Then we tested the head pressures of different rotor print angles at various viscosities. Results showed that the pumping of 22.5° rotors peaks at 6cP viscosity and decreased after 7cP. On the other hand, the 45° rotor peaks at 7cP and drops after 8cP. Lastly, the 0° rotor rises linear

and does not exhibit any maximum in the tested range (Figure 2-4A). Also note that for the µTesla-II pump, the output pressures were higher for viscosities higher than water at 1cP, in contrast to standard bladed pumps. Furthermore, pumping of the 3cP solution was compared to that of a shear-thinning xanthan solution to model biofluids. For shear thinning fluids, an increase in shear rate as modulated by rotor rpm leads to a decrease in viscosity. This agrees with the trends seen in (Figure 2-4B), where both solutions achieved similar pressures below 2000 rpm but xanthan falls behind after afterwards, leading to a ~9% difference at 4k rpm. In summary, our results suggest that surface texture can be tuned for a particular fluid viscosity, with 22° printed rotor giving us higher pump pressures in the physiological range of viscosities. Therefore, we adopted the 22° printed µTesla-II rotors for all subsequent FSS experiments.

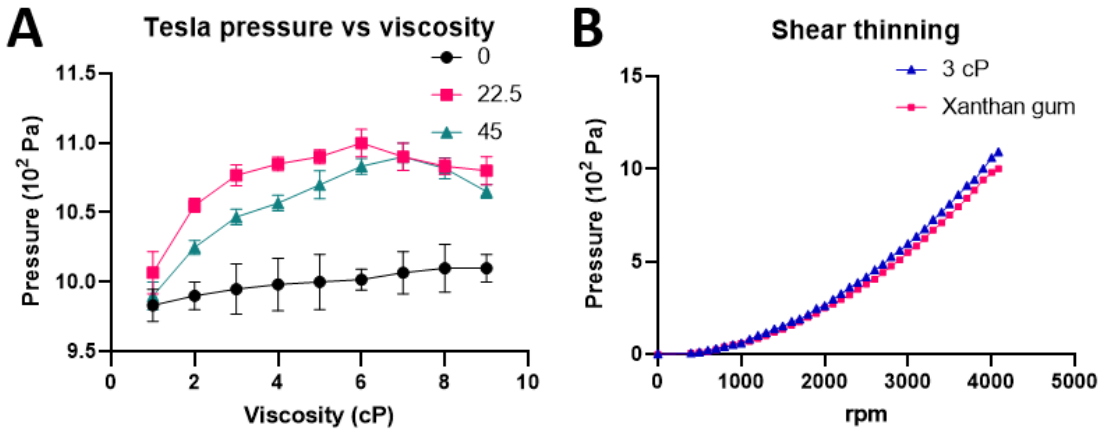


Figure 2-4. µTesla-II pump different surface texture optimization. A. Different print angles, and thus textures, yielded differential pump output vs. viscosity. Result shows a peak pressure output at 6cP for 22.5° texture, 7cP for 45° texture, no significant peak found for 0 texture. B. Pumping of shear thinning xanthan gum versus 3cP glycerol using 25° angle printed µTesla pump. Comparing the 3cP viscosity fluids to Xanthan gum solution at 3cP, the pressure output of Xanthan gum solution shows a pressure drop at higher rpm, which means the fluid viscosity was decreased by the shear generated from the pump.

### 2.3.4 Glucose and Shear Stress Effects on Calcium Influx

A perfusion test using water to clear food dye in the droplet serpentine channel was conducted (Figure 2-5A,B). This simple characterization showed that syringe pump perfusion has 10 s delay followed by a sharp pump-on bump in flow rate and clearance, probably a pressure burst due to the stepper motor pulse, within the first 20 s of the flow. Then, we studied potential shear stimulations on pancreatic beta cells and their glucose-insulin response (Figure 2-5C, D). The result shows that for both Beta TC-6 cells and INS1 cells, a strong shear-dependent overshoot was seen in the first couple of minutes, with higher overshoot for the syringe pump versus μTesla pump. For both cell types the Fura-2 calcium response settles back to normal after 15 minutes of perfusion.

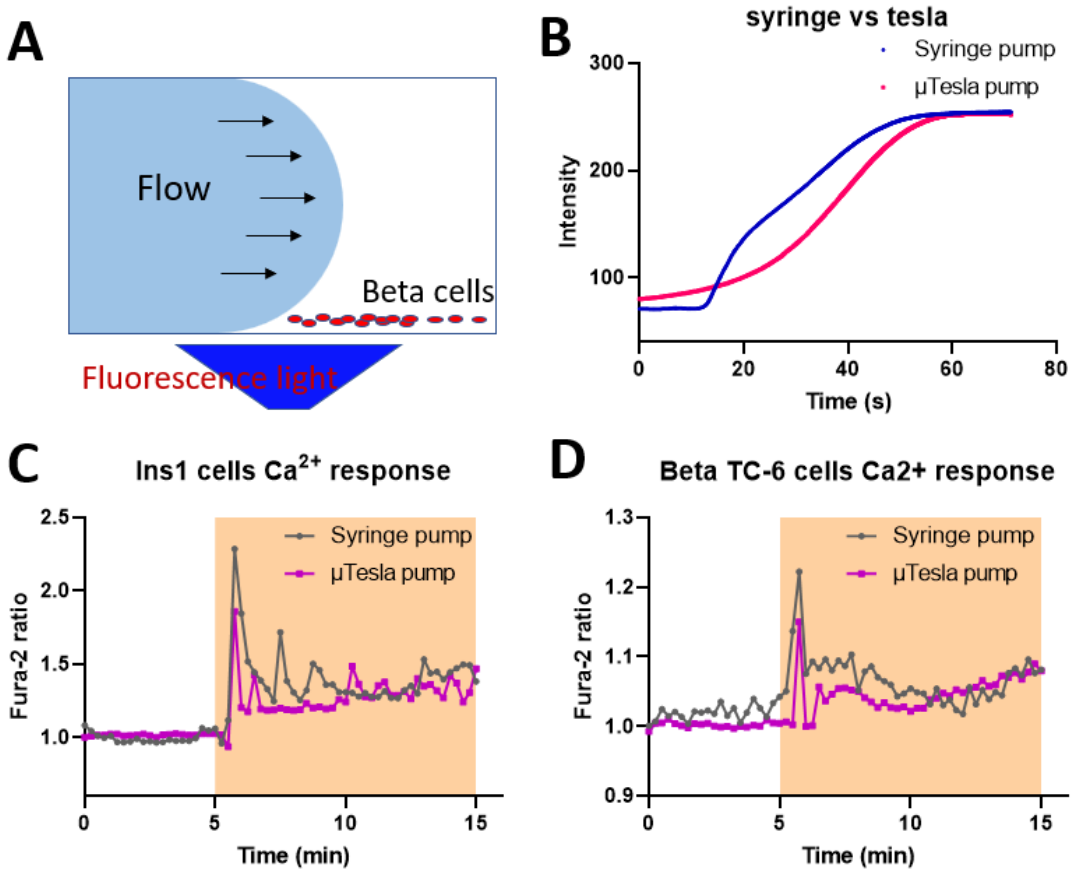


Figure 2-5. µTesla-II pump vs syringe pump. A. flow shear on beta cells inside the microfluidic channels. B. Syringe pump has a 10 s delay followed by a sharp pressure burst within the first 20 s of the flow. On the other hand, the µTesla spools up smoothly. Moreover, shear induces overshot and early transients in of C. Beta TC6 versus D. INS1 cells in microfluidics channel, where syringe pump showed more overshot.

### 2.3.5 Glucose and Shear Effects on Mitochondrial ATP Level

As our results suggest that a higher shear stress from syringe-driven perfusions affected calcium response in beta cells, we investigated FSS effects on their mitochondrial ATP response. The result shows that for Beta TC6, the syringe pump show an artifact in the form of boosted ATP response under flow, compared to that of the stable and flat response seen in µTesla-driven cells, denoted

by the red traces (Figure 2-6A, B), In INS1 cells, similar trends were seen where the syringe pump response was higher than µTesla pump responses (Figure 2-6C, D). One thing noted is that the Krebs-Ringer buffer here plays an important role in ATP depletion to mimic the diabetes related ATP depletion in beta cells.

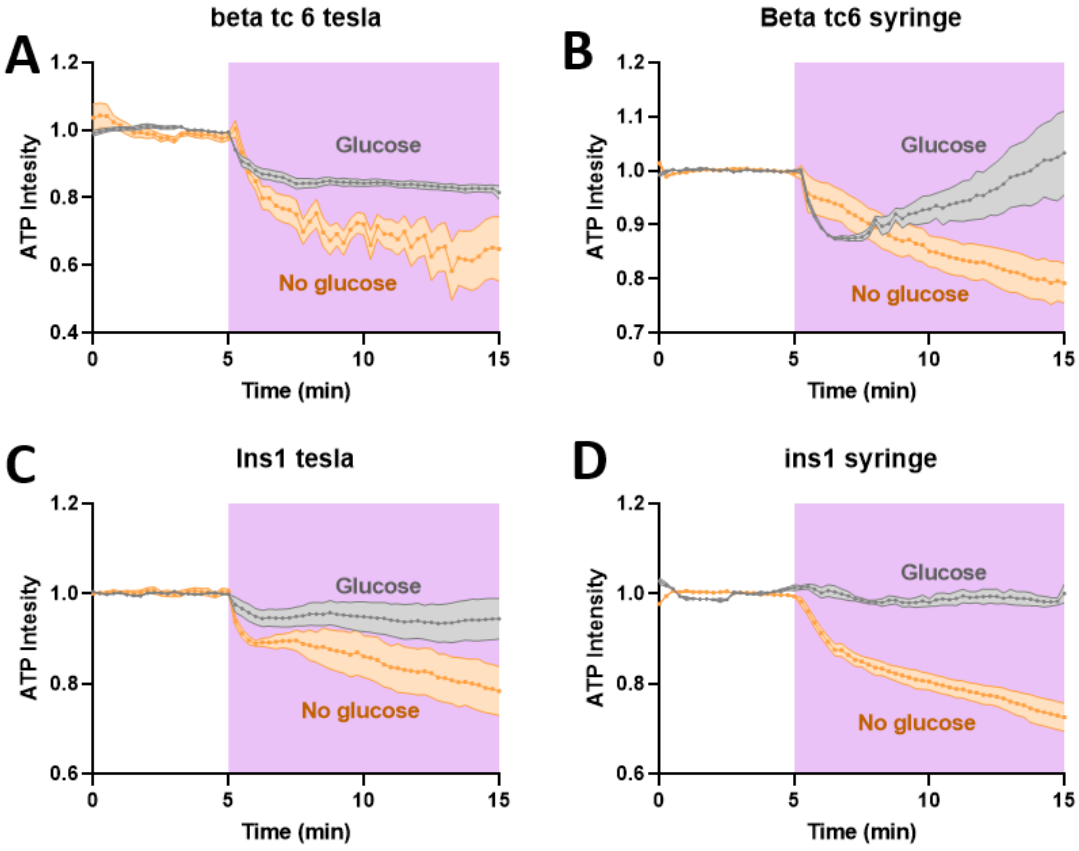


Figure 2-6. ATP response µTesla pump vs syringe pump. A. For Beta TC6, an artificial boost in ATP activities (red curve) was seen in syringe pump versus B. µTesla flow. C. D. For INS1 cells, ATP responses were generally greater than Beta TC6, but also with elevated response using syringe vs µTesla pump.

## 2.4 Conclusion

In the study, we designed and fabricated a μTesla-II pump and compared it to traditional syringe pump and peristaltic pump. our μTesla-II pump was characterized for use with fluids of different viscosities, providing smoother pump-on and stable flow than conventional syringe pump. μTesla-II's smoother flows led to less artifacts in shear-stimulated beta cell glucose-insulin response, compared to traditional syringe pump-driven perfusion. An optimized μTeslla-II pump could be the answer to the next generation microfluidic flow source, due to its cell compatibility, laminar flow generation, smooth output flow, and lower fabrication costs.

To fully harness the potential of our μTesla pump, it is necessary to integrate it into microfluidic devices to pump fluids directly to cells and enable constant, smooth, and recirculating flow inside the device. However, to achieve this, new fabrication techniques are needed to enhance the compatibility of the pump with microfluidic devices. We will discuss our strategy in the next chapter.

# Chapter 3. Monolithically 3D-Printed Microfluidics With Embedded µTesla Pump

Microfluidics has earned a reputation for providing numerous transformative but disconnected devices and techniques. Active research seeks to address this challenge by integrating microfluidic components, including embedded miniature pumps. However, a significant portion of existing microfluidic integration relies on the time-consuming manual fabrication that introduces device variations. we put forward a framework for solving this disconnect by combining new pumping mechanics and 3D printing to demonstrate several novels, integrated and wirelessly driven microfluidics. First, we characterize the simplicity and performance of printed microfluidics with a minimum feature size of 100 µm. Next, we integrated a microTesla (µTesla) pump to provide non-pulsatile flow with reduced shear stress on beta cells cultured on-chip. Lastly, the integration of RF and hobby-grade brushless motor completes a self-enclosed platform that can be remotely controlled sans wires. Our work shows how new physics and 3D-printing approaches not only provide better integration but also enable novel cell-based studies to advance microfluidic research.

# 3.1 Introduction

### 3.1.1 Benchtop Microfluidic Pumps

Lab-on-a-chip devices require a source of fluidic power. Conventional benchtop flow sources can be sorted into multiple types based on their driving force: Gravity-driven pumps can output continuous flow, but their pressures vary over time. Flow from surface tension-driven pumps is also continuous with varying pressure. A recent study of gravity-driven and surface tension-driven flows by Sung et. al, and Beebe et. al showed the disadvantages of these two pumps in long-term perfusion and flow control [103-105]. Precision syringe pumps can provide flow with minute pressure oscillations from a fixed syringe volume [106]. Pressure-driven pumps have accurate flow and pressure controls but are also limited by chamber volumes and unable to recirculate the flow [107]. Peristaltic pumps can siphon and recirculate flow, but their flows are highly pulsatile by nature [108, 109]. Centrifugal flow à la rotating devices from Ren, Y et. al, can generate a wide range of flow rates [110]. But centrifugal flow is directionally outward and cannot be recirculated back into the device. Overall, conventional pumps cannot combine continuous, non-pulsatile flow with flow recirculation for long-term microfluidic cell culture. *In vivo*, pulsatile flow is an inherent characteristic in large blood vessels and central to vascular homeostasis. For in vitro microfluidic models, however, pulsatile pressure waves create unwanted shear stress that can affect cell survival, differentiation, and biomechanical stimulation.

### 3.1.2 On-Chip Integrated Pumps

There are currently several novel techniques to achieve on-chip microfluidic pumps. These include accoustofluidic pumps, the technology used in inkjet print heads; electroosmotic pumps, which apply a voltage across a diffusion membrane to control ionic flow; electrolysis gas pressure pumps; capillary force siphoning à la paper microfluidics; thermal driven micropump that use thermal bubble as pinching rollers to provide peristaltic flow; finger-actuated and solenoid driven pumps that employ deformable dome valves to displace fluid volumes; and integrated ion pumps designed for drug delivery application [111-117]. However, these integrated pumps cannot provide continuous, non-pulsatile flow in a recirculating manner for long-term cell culture. Thus, a microfluidic flow source with recirculation function, continuous flow, and low shear stress is vital to the next-gen lab-on-chip devices. Boundary-layer pumps such as Tesla turbines can achieve these requirements in a recirculation form, and its miniaturization would solve our microfluidic pumping needs.

### 3.1.3 Tesla Turbines Miniature Pumps

Tesla turbine is characterized by a stack of concentric disks with predefined gaps and spiral fluid flow. The operation of a Tesla turbine relies on the continuous momentum transfer between the flow and the rotating disks within the fluid boundary layers. First patented by Nicola Tesla in 1913, Tesla turbines were initially applied to large-scale hydroelectric power generation [118, 119], and subsequently became popular in miniaturized applications among researcher enthusiasts. Specifically, Couto et al. in 2006 discussed the number of disks required for a Tesla turbine based on fluid mechanics [99]. E. Lemma et al. in 2008 and his team performed a numerical study to explore the viscous flow turbine and the results showed a 25% turbomachinery efficiency [120].

In recent years, Ensign et al. designed a multi discs fan based on the Tesla turbine principle [121]. Moreover, computational modeling explored the design and optimizations of Tesla turbines. L. Ciappi et al,'s simulation results suggested that in small scales and miniature sizes the Tesla turbine could be a valuable portable power generator [122]. K. Rusin et, al modeled a five disks Tesla rotor and the simulation showed a doubling of efficiency compared to normal bladed turbines [123]. However, there was a lack of research on Tesla turbines at the microfluidic scale until our group's efforts in 2016 [102]. In that previous work, we leveraged resin-based stereolithography 3D printing to achieve a miniature pump the size of a quarter. While that work demonstrated a μTesla pump-driven microfluidic gradient, we realized that a complicated fabrication and integration would hamper the adoption of μTesla technology.

### 3.1.4 3D Printed Microfluidics

Microfluidics are microengineered devices that enable precise fluid flow and routing. In the past few years, 3D printing has expanded the microfabrication toolbox with non-planar, low-cost, and faster fabrication processes. However, the resolution of consumer-grade 3D printing still lags behind that of traditional fabrication methods like SU-8 molding.

Lithography-based 3D printing relies on a UV laser or other light source to polymerize photo-curable resin from a bath layer-by-layer. Consumer-grade machines with XY resolution down to 30 and 20μm are available at prices from $500 to $2k, making them an affordable choice for fast microfabrication compared to the classical cleanroom processes [124]. Recent advances from Hua Gong et, al. customized a 3D printer to print channels with dimensions of 18x20μm [125]; a few microfluidic devices were fabricated for emulsion perfusion and droplet generation [126-129]. However, conventional resins leave unpolymerized components that are toxic to cells [130],

requires extra step to reduce the toxicity and avoid PDMS curing inhibition [131-133]. Researchers have also developed cell-compatible bio-resins for lithography-based 3D printing [134], but their print resolution, and especially cost efficiency, are far from optimal. Furthermore, studies have also demonstrated that residues from resin-printed molds prevent PDMS from curing itself, requiring extensive post-processing using vacuum ovens.

Fused deposition modeling (FDM) 3D printing is an alternative approach to fabricating integrated microfluidic devices. Consumer-grade FDM machines are more cost-effective with starting prices around $300-$1500. In FDM printers, a stepper motor drives the extruder gears to push polymer filaments through a heated nozzle, which is moved across a heated print bed to deposit materials layer by layer [124, 126, 135]. Multiple cost-effective materials can be used, including polylactic acid (PLA), acrylonitrile butadiene styrene (ABS), polyethylene terephthalate (PET), polycarbonate, and their modified variations [136]. In contrast to resin-based 3D printing, FDM resolution depends mostly on the nozzle orifice size. Some research groups have printed microchannel molds as small as 100-1000μm in width and 50-500μm height [137]. Nelson group improved the resolution by printing a microfluidic device with 100μm transparent channels [138]. The biggest advantage in terms of efficiency is the short printing time (typically less than 1hr) and the lack of post-processing compared to resin-3D printing or traditional photolithography itself. The low-cost, flexible, and automated process of FDM 3D printing represents a powerful tool for microfluidic device fabrication.

In contrast to most of the 3D microfluidics research where enclosed channels are printed, we printed the negatives of the microfluidic geometry for standard PDMS (poly-dimethyl siloxane) soft-lithography molding. As a standalone technique, 3D printing has limitations in fabricating microfluidic devices due to the resolution, material, and biocompatibility issues. However, we

leveraged the advantages of each technique—compatibility of PDMS molding and the robust automation of 3D printing—and created an integrated μTesla pump in a monolithic microfluidic system (Figure 3-1). The integration process was simple since most of the components such as pump housing, siphon, and output channels were designed alongside the microfluidics and printed at the same time. The only manual step for integration was the insertion of the μTesla rotor into the device prior to plasma bonding. And due to the designed dimensions, the components slot in with a snug fit that required no manual alignments. Our integrated pump empowered microfluidics research in long-term perfusion of cell culture, cell differentiation, and wireless operation of recirculating systems.

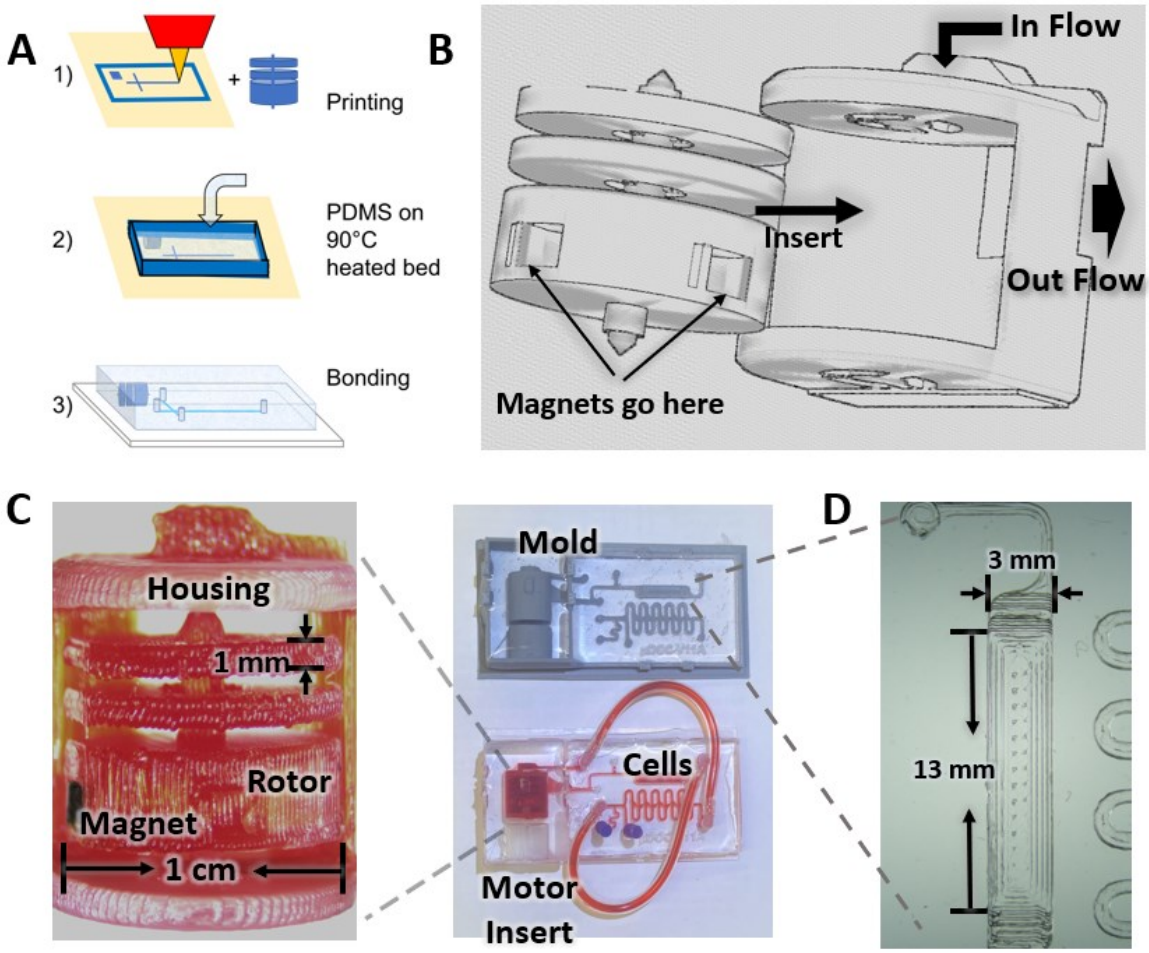


Figure 3-1. Microfluidic device fabrication method using 3D printing. A. Design the microfluidics device mold using Auto CAD and then printed using an FDM 3D printer. Microchannels and the µTesla pump were printed. The PDMS prepolymer is directly poured onto the heated bed and cured at 90°C. The device is then bonded with a µTesla rotor inside. B. Magnets was inserted in µTesla rotor, the rotor was then assembled in the housing, flow comes from the side of the housing and the rotor rotation drive the flow pumping out of the µTesla pump. C. PETG material was used to print the µTesla pump, with a rotor diameter of 1 cm. An integrated device was fabricated with µTesla pump assembled, with the main channel size being 700 µm in both width and height, and the smallest channel size of 200 µm in width and 700 µm in height. D. Close view of the cell culture and differentiation chamber. The chamber size is 3 mm in width, 3 mm in height and 13 mm in length.

## 3.2 Materials and Methods

### 3.2.1 3D Printing Optimization

The 3D prints were designed using Autodesk Inventor Professional 2023 (AutoDesk. Inc) and printed using a Voron Trident CoreXY 3D printer with polylite ASA filament (Polymaker, USA). Slicing of .stl files into G-code for the Voron printer was completed using a CURA slicer (Ultimaker, Netherlands) and the prints were optimized using nozzle diameters of 0.15 mm, 0.25 mm, and 0.4 mm. To print the patterns, the bed was heated to the desired temperatures such as 235°C, 240°C, and 245°C before starting printing. To ensure bed adhesion, adhesive glue (Magigoo MPC2018, Thought3D, Malta) was added to the bed before printing. Two parameters were varied in this: temperature, and nozzle diameter. The printed patterns were 1 mm tall, with line widths/gaps of 100 µm, 200 µm, 300 µm, 400 µm, and 500 µm in dimensions. To quantify the print quality, the channel, gap, and parts over gap ratios were calculated as follows:

Channel ratio= (Printed line width)/(Original line width) (1)

Gap ratio= (Printed gap width)/(Original gap width) (2)

Parts over Gaps (P/G)= (Printed line width)/(Printed gap width) (3)

The printed line width was the width of the line printed at three different temperatures with 3 different nozzle sizes. The same was defined for the printed gap widths. The original line and gap widths were the widths designed in CAD, which are presented in Supplementary Figure S1 as OSW and OGW, respectively.

### 3.2.2 3D Printing Roughness Measurement

A profilometer (Mitutoyo SJ-210, Japan) was used to measure the average roughness where the probe is used to detect the surface while physically moving to acquire the surface height. The surface roughness (Ra) of the printed channels was measured along each channel width for 3 samples per mold. Profilometry demonstrated the surface roughness across a single line pattern versus nozzle sizes, temperatures, and designed channel width.

### 3.2.3 µTesla Pump Fabrication and Sterilization

The µTesla rotor and the pump housing were printed at 240 °C in PETG (Polyethylene Terephthalate Glycol) by a Voron Trident 3D printer with a nozzle size of 0.25mm. The rotor diameter is 10 mm, with the housing designed to hold the free-spinning rotor within a molded microfluidic cavity. After printing, two magnets were inserted in the rotor in a polarized fashion. The rotor was then inserted in the printed pump housing to assemble the µTesla pump. The fabricated µTesla pump was soaked in 1M hydrochloric acid (HCL) to increase positive surface charges and then washed with distilled water 5 times. After the HCL incubation, the pump was incubated in 1% sodium dodecyl sulfate (SDS) for 2 days for sterilization and washed with PBS prior to device encapsulation [139].

### 3.2.4 Cell Culture Device Fabrication

The channels were printed in ASA at 240C using a 0.15 mm nozzle. The 3T3 L1 culture chamber size was 3 mm x 3 mm x 13 mm, the main channel size is 0.7 mm x 0.7 mm, the smallest channel size is 0.2 mm x 0.7 mm including droplet traps for future experiment, Figure 1B. A wall

surrounding the microchannels was printed to allow PDMS molding. While the device was printing, PDMS prepolymer was prepared and degassed to save time. It was subsequently poured onto the 3D-printed mold directly on the print bed and baked at 90°C for 1 hour. The cured PDMS was then peeled from the print bed and bonded with a glass slide encapsulating a pre-printed μTesla rotor using plasma bonding. The bonded device was baked at 100C on the hot plate for 2 hours before device sterilization for cell culturing.

### 3.2.5 Particle Velocimetry Analysis

The integrated microfluidic device was filled with PBS and operated at different rpm from 1200 to 4000. The device inlet was connected to a tube of PBS solution and the outlet was connected to a 15mL empty tube. By measuring the time for the pump to fill up the 15mL outlet tube, we can drive the pumping flow rate at different rpm. To calculate the flow velocity, 10μL fluorescent carboxylate-modified polystyrene latex beads (Sigma, USA) were dispersed in 2mL distilled water; the beads have an average size of 1 μm. Diluted beads solution was injected into the integrated pump for the experiments. The pump was then run at 1500 rpm which result in a flow rate around 50μL/min, fluorescent pictures were took at 100 ms exposure time inside the cell differentiation chamber. The flow velocity was calculated by measuring the travel distance divided the 100 ms exposure time.

### 3.2.6 3T3L1 On-Chip Culture and Differentiation

The 3T3 L1 cells were cultured in high glucose Dulbecco's modified eagle medium (DMEM) (4500mg/l glucose) with 10% bovine calf serum (BCS) inside a cell culture incubator. To culture

the cell in the device, device channels were incubated with Poly-l-lysin solution (Fisher) for half hour to enable cell attachment [140]. 3T3 L1 cells at 1x107 cells/mL concentration were loaded into the cell culture channel. The device was incubated for 5 hours to allow 3T3 L1 cell attachment. During the experiment, the device was driven by a stir plate at 1500 RPM inside a cell incubator. After the cell density became over confluent, the media was replaced with a differentiation media based on high glucose DMEM with 10% Fetal Bovine Serum (FBS), 1µg/mL insulin, 0.5mM methyl isobutylxanthine, and 0.25µM dexamethasone. After 3 days of incubation in differentiation media, the media was replaced with high-glucose FBS media containing 1 µg/ml insulin for another 3 days [141]. All the cell experiments were operated with the µTesla pump rotating at 1500 rpm, resulting in around 50µL/min flow rate.

### 3.2.7 Adipocytes Staining

The differentiated adipocytes were stained using an Oil Red O stain kit (Sigma). According to the protocol, cells were fully differentiated, and the media was removed from microfluidic device channels and washed using PBS. 10% formalin was gently pumped into the channels and incubated for 30 minutes for cell fixation. After that, the formalin solution was discarded, and the cells were washed twice using distilled water. Cells were then incubated with 60% isopropanol for 5 minutes. After the isopropanol was removed, the Oil Red O working solution was added for 15 minutes. After this incubation, the cells were washed 5 times with distilled water and incubated with Hematoxylin for 1 minute. Finally, the cells were washed 5 more times with distilled water until no excess stain was seen. After staining the device was imaged using a fluorescent microscope. Lipids droplets in adipocytes appeared red in color and the nuclei appeared blue in color [142].

### 3.2.8 Wireless µTesla Pump Operations

To achieve wireless operation, we designed an insert for a mini quadcopter brushless motor (2S, 0802 sizes) with a 10 mm neodymium donut magnet (N-S magnetized through the diameter, McMaster Carr). By connecting this electric motor and magnet combination, we can drive the µTesla rotor using hobby-grade micro-RC components. Furthermore, the motor/pump speed was monitored directly from the RC speed controller via a Bluetooth interface running on a cell phone.

### 3.2.9 Statistical Analysis

All experiments were conducted at least in triplicates and repeated three times. The data represent the mean ± S.E.M. of three independent experiments. Statistical analysis was carried out using one-way ANOVA and linear regression analysis. The differences between the two sets of data were considered significant at $p\text{-value}<0.05$.

## 3.3 Results and Discussion

### 3.3.1 Optimizing FDM 3D Printing for Integrated Microfluidics

We applied multiple line widths and gaps in 1 cm square patterns to optimize our FDM printing at various nozzle temperatures and orifice sizes (Figure 3-2). The use of these printed patterns is akin to the use of modulation transfer function in analyzing imaging optics, where spatial patterns better illustrate the imaging capabilities rather than single feature sizes. We note that our FDM optimization is not meant to compare with photolithography or resin 3D printing. However, we illustrate the capabilities of FDM printing as an integration technique for multiscale components.

The ratio for the printed parts over designed parts was calculated for the three different temperatures and then the ratio for channels and gaps was found. Irrespective of the printing temperature, a 0.15mm nozzle was shown to be the best size for printing channels below 200 µm and a 0.25 mm nozzle for channels between 300 µm and 500 µm. As shown in Figure 3A, for 235 °C, the ratio was 1.03±0.06 for the 0.15mm nozzle while the ratios for other nozzles of the same temperature were higher than 1 reaching 1.08±0.15 for 0.25 mm and 1.26±0.09 for the 0.4 mm nozzle ($p$-value<0.001). However, a different trend was noticed for 240°C and 245°C where the ratios decreased from 1.12±0.06 and 1.15±0.05 for 0.15 mm nozzle into 0.88±0.15 and 0.98±0.08 for 0.25 mm nozzle before it increased to reach 1.17±0.04 and 1.09±0.14 for 0.4 mm nozzle of 240°C and 245°C temperatures, respectively (Figure 3-3A) ($p$-value<0.001). The temperature parameter showed significant improvements to the printed geometries with p values of ***$p$<0.001. Temperatures with optimal channel dimensions were employed for all subsequent protocols. N>=3 for each condition tested.

To investigate more about the printing ratios versus line width, printing over design ratios for channels and gaps were calculated. The ratios were found to be closer to 1 for the channel width of 100 µm and 200 µm of 0.15 mm nozzle reaching 1.05±0.06 and 0.87±0.08 for 100 µm and 1.1±0.05 and 0.84±0.07 for 200 µm of channel and gap ratio, respectively (Figure 3-3B). The regression analysis for printing over design ratios showed a linear correlation between these values and initially designed strands for channels only with Pearson's r of 0.93; however, the analysis for gaps' ratios showed a nonlinear correlation with Pearson's r of -0.17 which means the error between printed, and the designed gaps are higher than that of channels. The 100 µm designed channel width for the 0.25 mm nozzle was unprintable (Figure 3-2). However, the ratios for other channels and gap widths of the same nozzle were the best with values slightly closer to 1 (Figure

3-3C). The regression analysis for 0.25 mm showed a linear correlation for both, channels and gaps with Pearson's r of -0.832 for channels and 0.59 for gaps. On the contrary, a completely different trend was found for the 0.4 mm nozzle with ratios close to 1 for channel measurements, and ratios not that far from the same value for the gap ones (Figure 3-3D). This can be attributed to over-extrusion while printing with high nozzle sizes and higher temperatures, resulting in gap values much lower than the design. This was noticed in the regression analysis where channels showed a completely linear correlation with Pearson's r of -0.71. Statistical analysis showed that p-values<0.001 for 0.4, 0.25, and 0.15 nozzles while comparing the three different temperatures. Linear regression showed that Pearson's r was closer to 1 for all the channels and gaps unless the gap ratios for 0.15 nozzle.

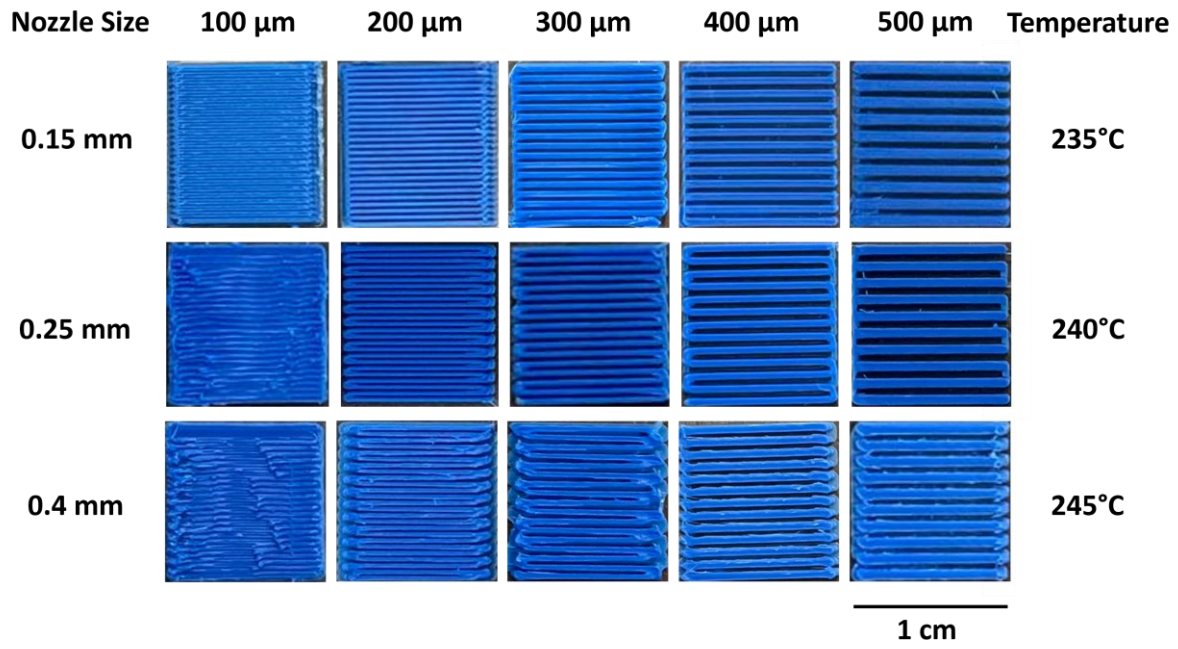


Figure 3-2. Printed patterns for FDM optimization. A pattern of lines and alternating gaps of equal widths were printed at 100, 200, 300, 400, and 500 µm widths. At their optimal temperatures, the smallest feature sizes were 100, 200, and 400 µm for 0.15, 0.25, and 0.4mm nozzles, respectively.

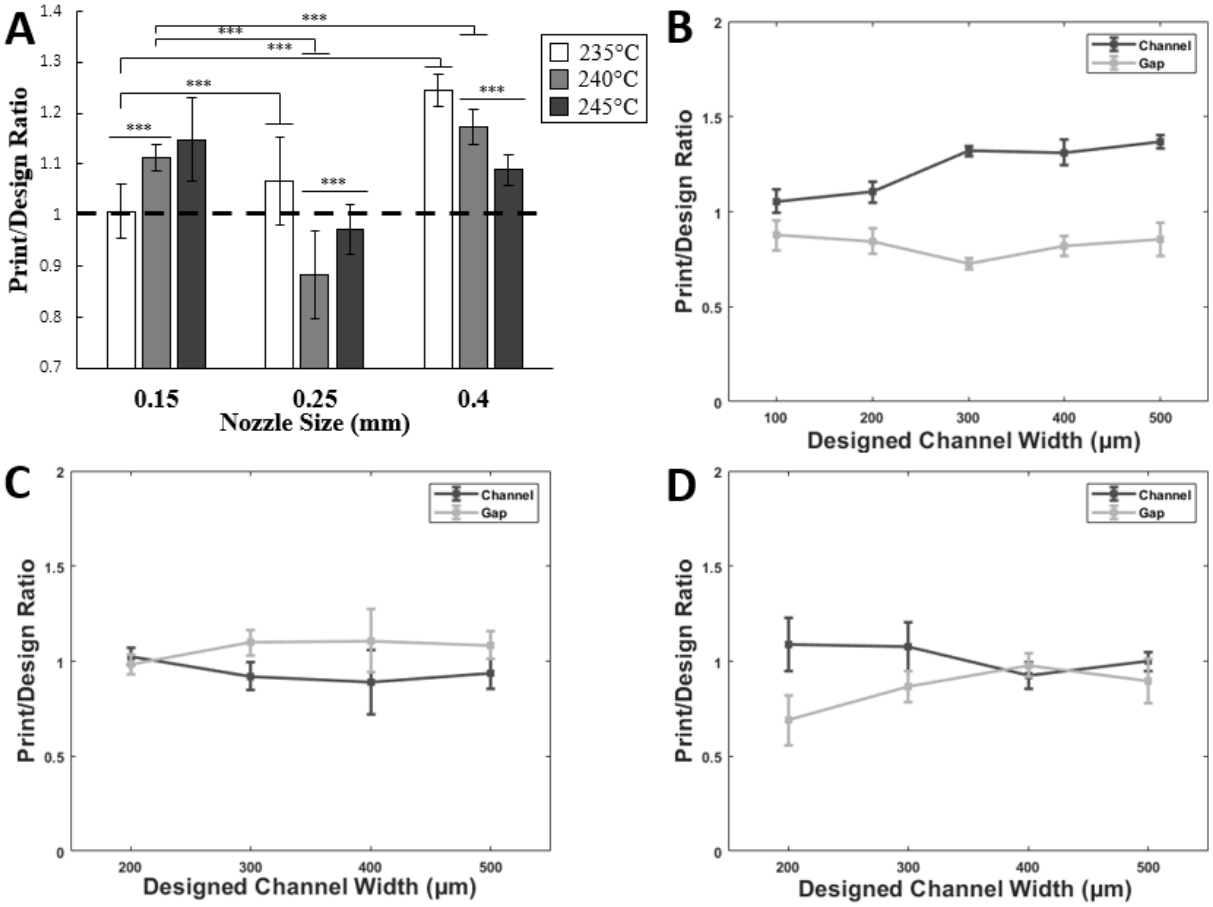


Figure 3-3. Optimizing FDM print resolution. A. When ABS filaments were printed at various temperatures, accurate line widths compared to their nozzle sizes were obtained at 235, 245, and 245°C for 0.15mm, 0.25mm, and 0.4 mm nozzles, respectively. At these optimal temperatures, alternating bands with line widths of 100 to 500 μm were printed at equal spacings. Data is represented as a ratio of printed over designed parts. Error bar S.E.M (N=3), ***p-value<0.001. B. For the 0.15 nozzle, the most accurate printed lines were obtained near the 100 μm designed width. Pearson's r=0.93 for channel and -0.17 for gap. C. For the 0.25 nozzle, the most accurate printed lines were obtained near the 200 μm designed width. Pearson's r=-0.83 for channel and 0.59 for gap. D. For the 0.4 nozzle, the most accurate printed lines were obtained near the 400 μm designed width. These values allowed us to tailor slicer parameters that best suit the desired microfluidic geometries. Pearson's r=-0.72 for channel and 0.78 for gap. Data is represented as a ratio of printed channel/gap over designed parts for the same channel/gap.

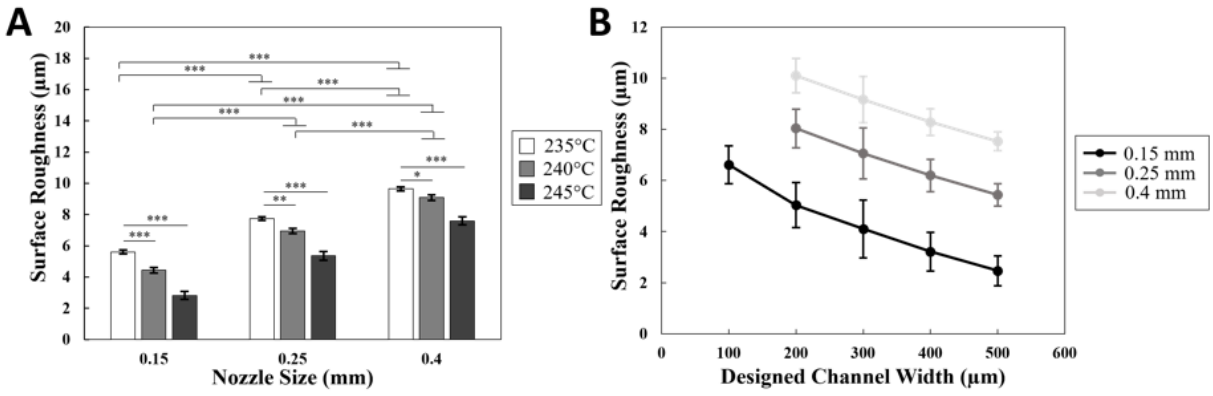


Figure 3-4. Surface roughness of printed channels. A Mitutoyo profilometer (Mitutoyo SJ-210, Japan) was used to characterize the surface roughness of the printed channels. A. The roughness decreases with increasing nozzle temperatures and smaller orifice sizes. B. Surface roughness decreases with increasing channel width and smaller orifice sizes. Error bar S.E.M (N=3), *p-value<0.05, **p-value<0.01, and ***p-value<0.001.

To measure the average roughness for the channel surface of the molds printed, a profilometer (Mitutoyo SJ-210, Japan) was used. Profilometry demonstrated the surface roughness across a single line pattern versus nozzle sizes, temperatures, and designed channel width. The data showed that the average surface roughness (Ra) increased with increasing nozzle sizes and decreased with increasing temperatures (Figure 3-4A). The surface roughness decreased from 5.61±0.12 for 235°C to 4.43±0.17 for 240°C, and then to 2.82±0.25 for 245°C (p-values<0.001). The same trend was found for the other 2 orifice sizes (0.25mm and 0.4 mm). However, a different trend was shown when comparing the roughness with orifice sizes as Ra increased with the increase in size. For 235°C, Ra increased from 5.61±0.12 for 0.15mm to 7.74±0.12 for 0.25 mm and then to 9.64±0.12 for 0.4mm (p-values<0.001). The same trend was found for the other 2 temperatures. These results indicate that the roughness and orifice sizes are directly proportional while roughness and temperatures are inversely proportional. These findings completely agree with the published

data [143] and [144]. On the contrary, Ra decreased with increasing channel widths and also decreased for the smaller nozzle sizes (Figure 3-4B).

### 3.3.2 3D Printing Material Compatibility for Cell Culture

3D-printed microfluidic devices were coated with Poly-l-lysin to promote cell attachment. 3T3 L1 cells were loaded into the cell culture chamber and cultured in the incubator until confluency. Both Resin printed µTesla rotors and FDM printed µTesla rotors were used to culture the cells in the device. Results showed that when resin printed, µTesla rotors were used to pump the system, cell density decreased in 4 hours, from 100% surface area to 30% surface coverage at the end of the 4-hour pumping (Figure 3-5A).

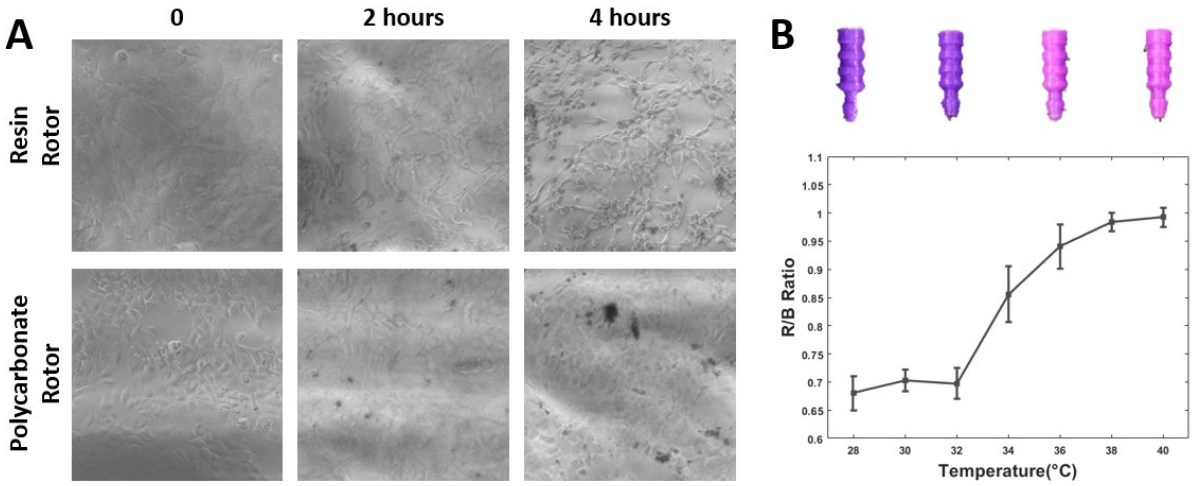


Figure 3-5. 3D printing material comparisons. A. Resin lithography and polycarbonate FDM printed µTesla rotors were used in the devices to culture 3T3 L1 cells. Culturing with resin-printed rotors lead to cell detachment when compared to FDM-printed polycarbonate rotors after 4 hours of incubation. FDM-printed rotors were adopted for subsequent cell culture. B. The temperature of the plug changes from purple to pinkish when the temperature increases from 28°C to 40°C.

### 3.3.3 Temperature-Sensitive Microfluidic Plugs

To enable monitoring of the cell culture outside of the incubator, plugs for fluidic ports were printed in temperature-sensitive PLA (37°C blue to pink PLA). After cell loading, the loading port on the microfluidic was sealed with these color-changing plugs, providing visual monitoring of the temperature close to the cell culture chamber. The sensor calibration was done via image processing, whereby the ratio of red to blue intensities was plotted from 28 to 40°C (Figure 3-5B). The calibration shows a sharp color change from 32 to 40°C, allowing a quick assessment of cell culture temperature at a glance. These calibrated temperature plugs were used to monitor temperatures in our devices in a variety of settings. We used them within the cell culture incubator while changing media or incubating fluorescent dyes, and atop the microscope stage incubator.

### 3.3.4 Flow Rate and Particle Velocimetry Analysis

The μTesla pump, as a pressure pump, has different working conditions when applied to various microfluidic channel resistances. In our μTesla integrated microfluidics, increasing pump rotation from 1200 to 4000 increased the flow rate from 33 to 900 μL/min (Figure 3-6A). For cell culture experiments, we choose 1500 rpm or 50 μL/min for media perfusion. Particle velocimetry experiments were performed and measured in the cell culture chamber (Figure 3-6B). Velocity at the center of the chamber was sampled at 3s intervals for 2 minutes (Figure 3-6C), showing a stable 150 μm/s velocity with a coefficient of variance of 4.67%. Across the 3 mm x 3 mm cross section of the cell culture chamber, the velocity profile exhibited a parabolic shape characteristic of laminar flow, with an R2- value of 0.824 (Figure 3-6D). The shear stress of the cell culture chamber was calculated when the pumps ran at 37°C with a 50μL/min flow rate, result shows the shear stress in the channel was around 0.6481*10-3 N/m2. These flow characteristics demonstrated that

our µTesla integrated platform can provide a non-pulsatile and continuous laminar flow that is critical to cell culturing and precise microfluidic assays.

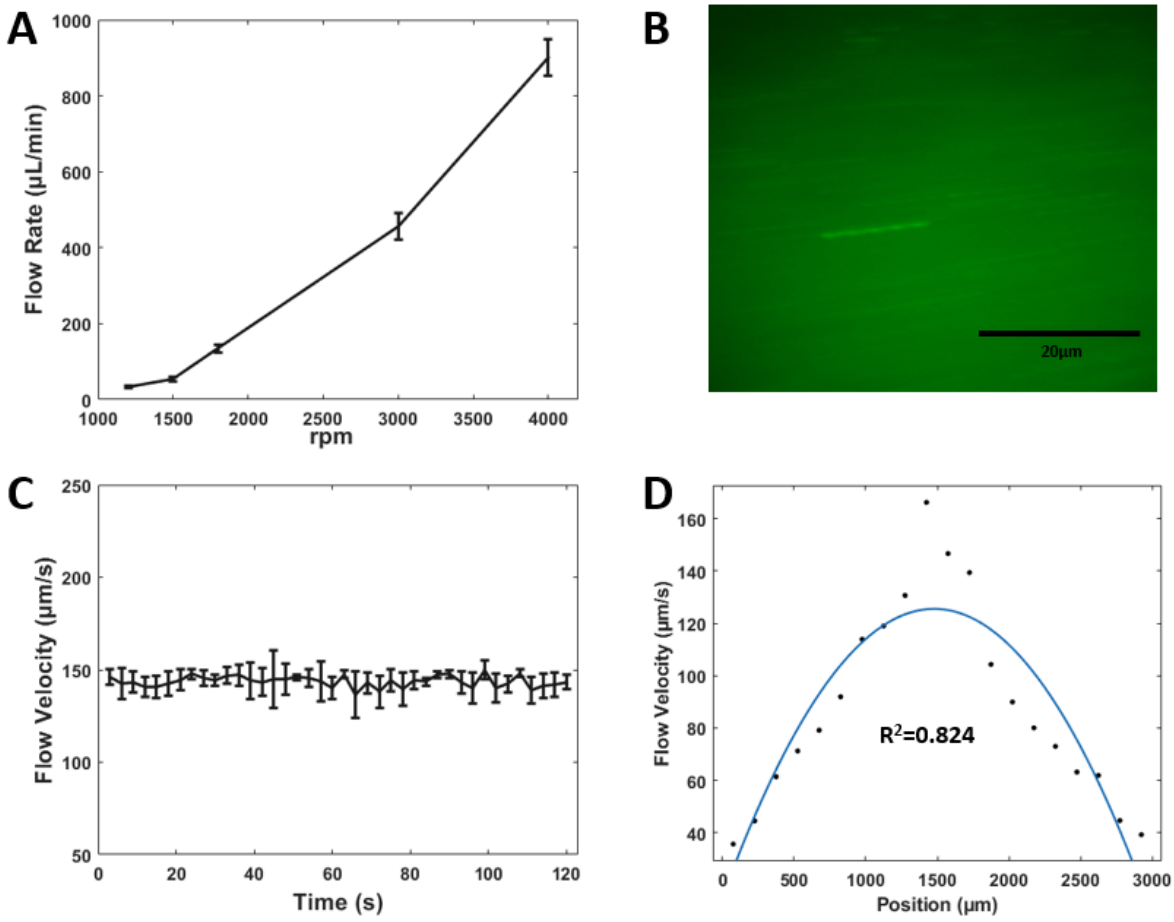


Figure 3-6. Flow rate and particle velocimetry for µTesla-driven microfluidics. A. Flow rate increases with increasing µTesla rotation. Note that we operate cell culture perfusion at 1500 rpm or 50 µL/min. B. Fluorescent microscopy of particles traveling in the center of the chamber. C. Particle velocity was continuously measured at the center chamber with 100ms exposure time at 3s intervals for 2 minutes total. D. Velocity profile inside the 3 mm wide cell culture chamber. A fitted parabola has an R2 value of 0.824, showing that the flow conforms to a laminar profile.

### 3.3.5 On-Chip Cell Culturing and Differentiation

We fabricated the cell culture device with an integrated PETG printed µTesla pump. The device included a rotor housing, motor housing, and a cell differentiation chamber to achieve long-term culturing. Poly-l-lysin coated device was used to culture cells for 24, 48, and 96 hours, with a sterilized PETG µTesla pump providing medium recirculation. The results showed that cells achieved a greater than 98% survival rate after 24 hours of culturing and 95% of the cells were alive after 96 hours of culture (Figure 3-7A, B).

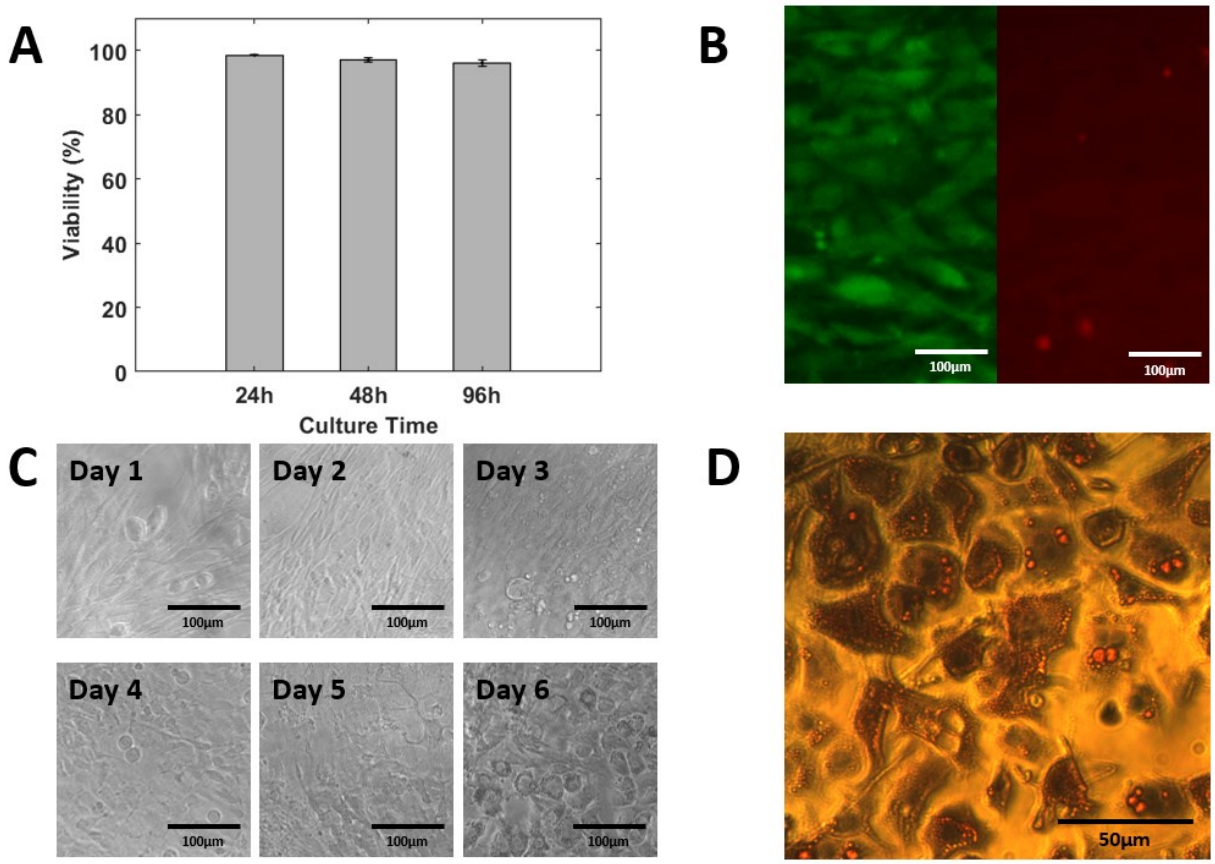


Figure 3-7. On-chip cell culturing and differentiation of 3T3 L1 cells to adipocytes. A. Viability was assayed up to 96 hours of culturing. B. Live dead assay after 96 hours culture. C. On-chip differentiation can be seen up to Day 6. D. Fat droplets were stained red and visualized under the microscope. This demonstrated the ability of our integrated pump to maintain long-term on-chip cell culturing.

3T3 L1 cells were loaded in the device and incubated until over-confluency, followed by incubation in differentiation medium for 3 days, insulin medium for 3 days, and finally FBS medium for 2 days (Figure 3-7C). The cells were stained with Oil Red O dye. Lipid droplets in the cells are stained red while the cell nuclear was stained blue. The differentiated cells have high counts of red droplets in their cytosols. The on-chip differentiation yielded more than an 80% differentiation ratio (Figure 3-7D). By leveraging the µTesla pump to power the microfluidic

device, we achieved long-term cell culturing and differentiation. This represents a powerful tool for future cell-based lab-on-a-chip applications.

We want to emphasize the advantage of our μTesla pump in providing integrated recirculating flow that allowed such a long-term cells culture on the chip. Without continuous perfusion, the 3T3 cells cannot survive beyond the differentiation process on a chip. And petri dish differentiated 3T3 cells also cannot be harvested and reseeded without losing differentiation. Achieving this length of culturing allowed new disease models such as adipose-beta co-culturing models of diabetes to be possible.

### 3.3.6 Wireless Operations

To demonstrate the utility of our 3D-printed microfluidic platform, we compared two types of device operations: 1) benchtop stir plate, and 2) miniaturized RC modes. Upon PDMS bonding, the encapsulated rotor with magnets can be directly actuated via a standard laboratory stir plate, in the same manner as our μTesla 1 [102]. In addition, we can wirelessly actuate the rotor via a micro brushless motor with magnetic coupling (Figure 3-8A). There were minimal differences between the stir plate and wireless operations in terms of output pressures as shown in (Figure 3-8B). At a max speed of 4.2 krpm, the power draw at 8V or full voltage for the 2S battery was 720 mW, Figure 8. When used with a 2S 400 mAh LiPo battery, the entire system ran for 4 hrs. without depleting the battery. Connecting multiple 2S LiPo batteries in parallel increased the runtime and allowed for quick swapping for indefinite operation in cell culture applications.

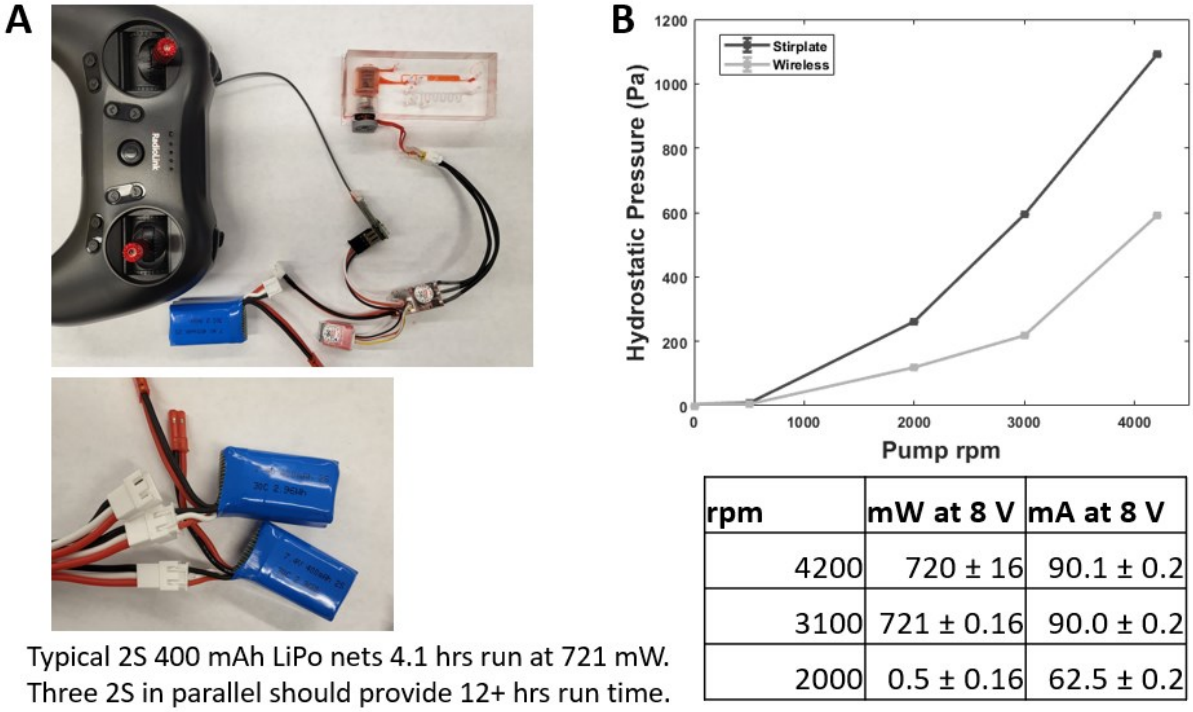


| rpm | mW at 8 V | mA at 8 V |
|---|---|---|
| 4200 | 720 ± 16 | 90.1 ± 0.2 |
| 3100 | 721 ± 0.16 | 90.0 ± 0.2 |
| 2000 | 0.5 ± 0.16 | 62.5 ± 0.2 |

Figure 3-8. Wireless Operation of Integrated µTesla Pump. A. Wireless operation was enabled by inserting a miniature quadcopter brushless motor into the device and powering it via a micro speed controller and RF receiver. The speed was controlled by the RF joystick (on the transmitter) and monitored via a Bluetooth app on a smartphone not pictured. B. The pump output under wireless operation was lower than the output when driven by a laboratory stir plate. The difference was attributed to brushless motor cogging below its designed speeds, which prevented steady µTesla rotations. The table summarized the power consumption of the wireless operation of the µTesla pump. At a maximum of 4k rpm, the power draw is 721 mW. With multiple LiPo batteries in parallel, the run time can be extended indefinitely.

## 3.4 Conclusion

In our view, FDM-printed microfluidics are not meant to compete in terms of resolution against classic SU8 photolithography. Nor are they meant to achieve the low cost of stamped and roll-to-roll manufacturing for industrial-scale microfluidics. What the current evolution of FDM microfluidic excels at is the ability to span the micro to millimeter-scaled dimensions, and do so

in a reliable, automated fashion. For applications that do not require channel resolution smaller than 100 μm, such as the 3T3L1 cell culture device, any novice student can learn to operate the printer to fabricate the entire PDMS in 2 hours. Furthermore, 3D printing in general, including FDM and higher resolution resin printing, enables novel three-dimensional structures like overhanging channels and non-planar cylinders and cones to be fabricated easily. The one multi-material print we demonstrated here was a clever temperature-sensitive plug for quick visual monitoring of cell culture temperatures. But numerous novel materials are already available, including conductive filaments, ferromagnetic filaments, and water-soluble filaments, with more being developed at a rapid pace. The most important contribution of this work was the development of an integrated microfluidic pump with its non-pulsatile and recirculating flow. And we achieved this fabrication not through complicated microfabrication, but by using a low-cost and fully automated 3D printing technique. There are numbers of complex microfluidics that can be accelerated and optimized using our integrated prototyping, for instance digital microfluidics [145], disposable nucleic assay amplification tests [146], and co-culture disease models [147]. To these and future bioengineering endeavors, we are proposing an integrated electromechanical microfluidic fabrication that is available at the push of a "print" button.

The integration of the μTesla pump into a microfluidic device has proven to be effective in providing smooth laminar flow to cells and facilitating a recirculation system. This system holds significant potential for a wide range of applications, such as long-term perfusion, cell differentiation, and co-culture studies. Through the combination of different types of cells, researchers can build organ-on-chip platforms or disease models on chip, opening up new avenues for diabetes research. These models could aid in the understanding of the mechanisms and development of the disease, ultimately leading to the development of novel therapeutic approaches.

This work was submitted to peer-review journal Micromachines, refer as "Duan, K., Orabi, M., Warchock, A., Al-Akraa, Z., Ajami, Z., Chun, T. H., & Lo, J. F. *Monolithically 3D-Printed Microfluidics with Embedded μTesla Pump*. Micromachines, 2023. 14(2), 237."

# Chapter 4. μTesla Pump Integrated Microfluidic Co-Culture System of Adipocytes and Islet Beta Cells

## 4.1 Introduction

Co-culture is important in numerous areas of biomedical research, as disease pathogenesis often involves multiple cell types. Therefore, *in vitro* disease modeling can benefit from reliable co-culture system [147-151]. In standard petri dish based co-culture systems, cell-to-cell interactions is created by physically introducing multiple cell types next to each other [152, 153]. To do this, researchers leverages cell patterning, cell multiple layers [154], cell stamping, or seeding on transwell membranes to culture different cell types together [155]. However, there are limitations, for examples, limit the cell types been co-cultured, slow mass transfer because of the stational medium, lack of the cell-to-cell interactions [156, 157] --- most happen only at the plane where two cell types meet each other [158]. Recent microfluidic co-culture approaches in drug testing, tissue regeneration, cell stimulation and metabolism [159-164], brought forth advantages in reliable control of culturing, long-term perfusion, and better geometries to mimic *in vivo* conditions. Nevertheless a recirculating microfluidic co-culture system is still sought after for biomedical research.

### 4.1.1 Microfluidic Co-Culture

Microfluidic technology is a great tool for engineering fluids at the submillimeter scale and studying biology environments. Due to the advantages such as high fabrication resolution of SU-8 photolithography, PDMS transparency, and its gas-permeability, SU-8/PDMS soft-lithography based microfluidic has been wildly applied in lab-on-chip research. These include microfluidic models for cancer biology, immunology, chip-based neurobiology, angiogenesis, among others [165-168]. The main limitation of these lab-on-chip models is their ability to study complex, muti-step and multi-cellular biological process. To better address the issue of disease complexity, co-culture based microfluidic were designed based on two approaches. First approach is to culture different types of cells in different microfluidic chambers [169], separated by a diffusion membranes used to control mass transport. The second approach is to leverage biocompatible hydrogel [170, 171], in which different types of cells were encapsulated and the mass transport is then tuned via hydrogel diffusion. In either of these approaches, the interactions between different types of cells are still limited by the route of media perfusion, where fresh media injection convectively dilute and clear out any relevant biomolecular secretion from one cell to the other [172]. On the other hand, a recirculating microfluidic co-culture system can address both of these limitations. An integrated microfluidic flow source is the key to achieve on-chip recirculation without volume dilution. In comparison, recirculation using standard peristaltic pumps introduces pulsatile flow and related shear stresses. Gravity-driven flow is dynamically decreasing and cannot recirculate device outflows back to its volume. Recent approaches based on centrifugal and capillary forces are still directional and volume limited. In this study, we leveraged a 3D printed microfluidic platform with and integrated μTesla pump to build a high throughput co-culture system for long term recirculated perfusion.

### 4.1.2 Co-Culture of Adipocytes and Islet Beta Cells

Obesity and type 2 diabetes are two strongly associated disorders, nearly one third of diabetes persons are overweight. In obesity, the raising level of free fatty acids (FFA) [173] will lead to the release of inflammatory cytokines include interleukin-6 (IL-6) and tumor necrosis factor-alpha (TNF-α) [174, 175]. These inflammatory responses also lead to insulin resistance in adipocytes. FFA's effects on adipocytes evidently function through the ER (endoplasmic reticulum) stress sensor PERK (protein kinase R (PKR)-like endoplasmic reticulum kinase) [176-178]. Moreover, ER stress and the unfolded protein response (UPR) mechanisms are also modulated by hypoxia through the same PERK sensor, leading to hypoxia stimulated cytokine release [179-182]. In addition, visceral adipose tissue expansion in obesity is associated with hypoxia and HIF1 activation [183]. Thus, FFA-hypoxia synergy can be hypothesized as a mechanism of adipocyte cytokine modulation. Among this mechanism, the cell-to-cell communication between adipocytes and beta cells is central to the mechanism of FFA-hypoxia synergy. As a result, TNF-α modulates beta cell survival and IL6 impairs glucose stimulated insulin secretions [184]. To deterministically deconvolve this potential FFA-hypoxia synergy, it is important to quantify their individual and combined effects on the rates of adipose cytokine release, and their downstream influences on beta cells.

## 4.2 Materials and Methods

### 4.2.1 µTesla Pump Fabrication and Sterilization

The µTesla rotor and the pump housing were printed at 240 °C in PETG by a Voron Trident 3D printer with a nozzle size of 0.25mm. The rotor diameter is 10 mm, with the housing designed to hold the free-spinning rotor within a molded microfluidic cavity. After printing, two magnets were inserted in the rotor in a polarized fashion. The rotor was then inserted in the printed pump housing to assemble the µTesla pump. The fabricated µTesla pump was soaked in 1M hydrochloric acid (HCL) to increase positive surface charges and then washed with distilled water 5 times. After the HCL incubation, the pump was incubated in 1% sodium dodecyl sulfate (SDS) for 2 days for sterilization and washed with PBS prior to device encapsulation.

### 4.2.2 Cell Culture Device Fabrication

The channels were printed in ASA at 240 °C using a 0.15 mm nozzle. The 3T3 L1 culture chamber size was 3 mm x 3 mm x 13 mm, the main channel size is 0.7 mm x 0.7 mm, the smallest channel size is 0.2 mm x 0.7 mm including droplet traps for future experiment, Figure 4-1A. A wall surrounding the microchannels was printed to allow PDMS molding. While the device was printing, PDMS prepolymer was prepared and degassed to save time. It was subsequently poured onto the 3D-printed mold directly on the print bed and baked at 90°C for 1 hour. The cured PDMS was then peeled from the print bed and bonded with a glass slide encapsulating a pre-printed µTesla rotor using plasma bonding. The bonded device was baked at 100C on the hot plate for 2 hours before device sterilization for cell culturing.

### 4.2.3 3T3L1 Cells Culture and Differentiation

The 3T3 L1 cells were cultured in high glucose Dulbecco's modified eagle medium (DMEM) (4500mg/l glucose) with 10% bovine calf serum (BCS) inside a cell culture incubator. To culture the cell in the device, device channels were incubated with Poly-l-lysin solution (Fisher) for half hour to enable cell attachment [40]. 3T3 L1 cells at 1x107 cells/mL concentration were loaded into the cell culture channel. The device was incubated for 5 hours to allow 3T3 L1 cell attachment. During the experiment, the device was driven by a stir plate at 1500 RPM inside a cell incubator. After the cell density became over confluent, the media was replaced with a differentiation media based on high glucose DMEM with 10% Fetal Bovine Serum (FBS), 1µg/mL insulin, 0.5mM methyl isobutylxanthine, and 0.25µM dexamethasone. After 3 days of incubation in differentiation media, the media was replaced with high-glucose FBS media containing 1 µg/ml insulin for another 3 days [41]. All the cell experiments were operated with the µTesla pump rotating at 1500 rpm, resulting in around 50µL/min flow rate.

### 4.2.4 Beta Cells Culture

Islet INS1 cells were cultured in RPMI 1640 medium with with 10% fetal bovine serum, 50 IU/mL penicillin, 50 mg/L streptomycin, 10 mM HEPES, 2 mM L-glutamine, 1 mM sodium pyruvate, and 50 µM beta-mercaptoethanol. Cells were maintained in a 37° cell culture incubator under 5% $CO_2$ and humidified atmosphere, medium was changed every 2 days and split every 4 days.

### 4.2.5 On Chip Beta Cells Culture

After the INS1 cells grown nearly confluent in dish in the incubator, cells were trypsinized and collected after centrifuging, then cells were suspended in GelMA hydrogel at 1 million cells per milliliter concentration. The hydrogel prepolymer solution with cells was introduced at 1 μL $min^{-1}$, and mineral oil was introduced at 12 μL $min^{-1}$ to generate the droplets at the microfluidic T cross-junction. When one of the generated droplets was flown into the serpentine pockets, its trapping blocked the cross-serpentine flow and redirected the next droplet toward the following pocket sequentially. After trapping, cell co-culture medium was introduced into the channel, the device was then put on the stir plate at 1500 rpm, resulting in a flow rate around 20 μL $min^{-1}$. The whole setup was then placed in the cell culture incubator for the co-culture and glucose stimulation.

### 4.2.6 Reagents Preparations

IL-6 Goat anti-Mouse (Polyclonal, R&D Systems), IL-6 Rat anti-Mouse (Monoclonal, BD Biosciences) were procured from Fisher Scientific, Anti-Insulin-Like Growth Factor-II antibody (Goat, Polyclonal), Anti-Insulin-like Growth Factor-I antibody (hamster, Monoclonal), Anti-Goat IgG (whole molecule)–TRITC antibody (rabbit, Polyclonal) were procured from Sigma-Aldrich. PEGDA (Mn ≈ 6000), PEG (Mn ≈ 20,000), photoinitiator (2-hydroxy 4′-(2-hydroxyethoxy)-2 methylpropiophenone), PBS, and BSA were procured from Sigma-Aldrich. Acrylate poly (ethylene) glycol succinimidyl carboxymethyl, Mn 5000, (ACRL-PEG-SCM-5000) was obtained from Laysan Bio Inc. (Arab, AL). To immobilize the antigens within the microgel, the primary antibodies were incubated with 1.25 mg of ACRL-PEG-SCM-5000 in PBS at room temperature for 3 h prior to use and discarded afterward. The prepolymer solution consisting of 100 μL of 8% (w/v) of PEG6000DA, 2% (w/v) photoinitiator, 10% (w/v) PEG 20K, and acrylated antibodies

was then loaded in the microfluidics for droplet generation. Then, BSA buffer was flown in at 30 μL $min^{-1}$ to continuously wash the droplet for 30 min to prevent polydimethylsiloxane (PDMS) protein absorption. Lastly, PBS was flown in at 30 μL $min^{-1}$ to continuously wash the droplets for 4 h to remove the unreacted reagents and PEG porogens, thus creating the porous microgel.

### 4.2.7 Insulin and IL-6 ELISA Assay

IL-6 Rat anti-Mouse (BD Biosciences), Insulin (porcine, Sigma) were procured to calibrate the assay. For secreted biomolecule detection, different prepolymers containing different acrylated antibodies were loaded in the microfluidic tubing (Tygon tubing 1/16 in. ID). The prepolymers were then delivered into the microfluidics using a syringe pump to generate droplets. After generating and trapping droplets with the first prepolymer reagent, subsequent unwanted droplets were redirected to the waste channel. These smart microgel droplets were then UV-cured and washed as described above. To run the assays, smart microgels were incubated with appropriate antigens and collected co-culture medium at 20 μL $min^{-1}$ flow rate for 60 min. Then, they were washed with TBST at 30 μL $min^{-1}$ for 15 min and subsequently incubated with the detection antibodies at 30 μL $min^{-1}$ for 40 min. Following this, droplets were washed again with TBST for another 15 min and then incubated with Secondary antibodies for another 60 min. After another 5 min washing with TBST, the device was then put under a fluorescence microscopy for imaging.

### 4.2.8 ZnT-8 Detection

After the co-culture of the adipocytes and INS-1 cells, the INS-1 cells inside the GelMA hydrogel droplet were then washed with PBS 5 times to remove the co-culture medium in channels.

After that, the INS-1 cells were incubated with 200 times diluted ZnT-8 Antibody (B-9) HRP (Santa Cruz Biotechnology) for 30 minutes, then the device was put under a fluorescence microscope for imaging.

## 4.3 Results and Discussion

### 4.3.1 Device Fabrication

The co-culture device was fabricated using filament-based 3D printer and PDMS soft lithography as described in Chapter 3, the large microfluidic chamber is designed for differentiation of adipocytes, and the serpentine channel is designed for generating the GelMA (Gelatin methacryloyl) hydrogel droplet for INS-1 cells culture (Figure 4-1A). After cultured the 3T3L1 cells in the cell culture chamber, differentiation cell culture medium and insulin medium were introduced into the channel sequentially, incubated the cells in each type of medium for 3 days until the 3T3L1 cells were differentiated into adipocytes (Figure 4-1B). After that, GelMA hydrogel droplets with INS-1 cells were generated and trapped in the pockets in serpentine channel (Figure 4-1C). By using 1/16| Tygon tubes to connect the two microchannels and replacing the medium with co-culture medium, the rotation pump will start the co-culture.

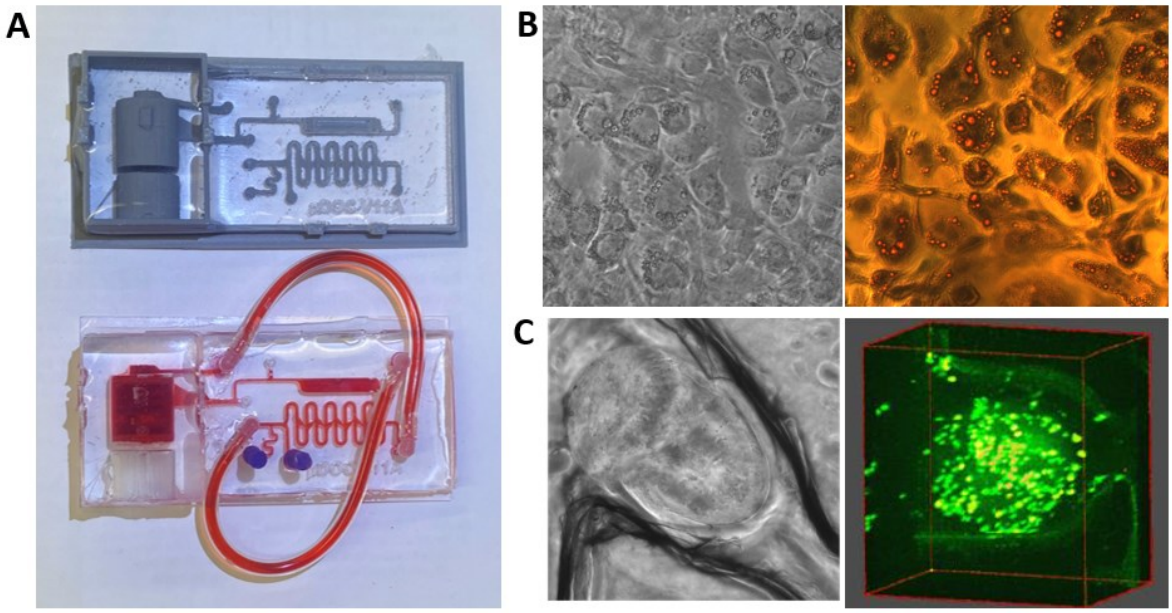


Figure 4-1. co-culture of adipocytes and INS-1 cells. A. co culture device with μTesla pump integrated was fabricated using filament-based 3D printer and PDMS soft lithography, tubes connected the adipocytes culture chamber and INS-1 culture channel for co-culture. B. adipocytes were differentiated from 3T3L1 cells, after oil-red-o staining, the lipids were stained to red color, and nucleus were stained to blue color. C. INS-1 cells were cultured in the GelMA hydrogel droplet in pockets.

### 4.3.2 Insulin and IL-6 Detection Assay Optimization

Insulin and IL-6 detection were enabled via PEGDA smart hydrogel droplets loaded along side the adipocyte/beta co-cultures. The PEGDA prepolymer solution containing different antibodies were injected into the droplet generation device. PEGDA droplet were then generated and trapped in the device pockets. After 5 minutes of UV curing, PEGDA droplets were cured. The immunodetections assays were ran at designated concentration: 50, 100, 300, 1000, 10000 pg/mL, fluorescence ratios were measured under a fluorescence microscopy, result shows that the fluorescence ratio of insulin and IL-6 droplets will increase with the increasing of antigen concentration in the designated solutions. The detection limit was then calculated as 3.3 times the

standard deviation of the blank response divided by the slop of the calibration curve. Thus, insulin detection limit was calculated to be 23.74 pg/mL (Figure 4-2A) while IL-6 detection limit was 10.8 pg/mL (Figure 4-2B), compared to standard ELISA assay, a 50 pg/mL limit of detection for insulin and 2.453 pg/mL limit of detection for IL-6.

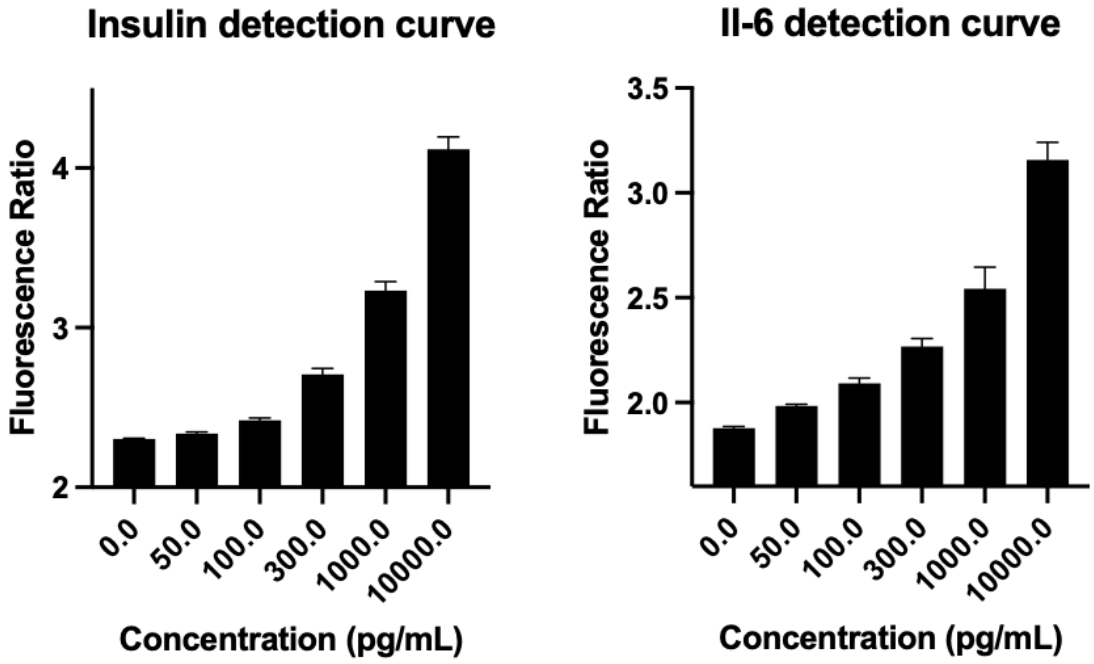


Figure 4-2. Optimizations of insulin and IL-6 detection curve. A. the fluorescence ratio shows that by increasing the concentration of insulin in sample solution, the fluorescence ratios increase, the detection limit of insulin is 23.74 pg/mL. B. the increase of IL-6 concentration in sample solution results in the increase of fluorescence ratio, the detection limit of IL-6 is 10.8 pg/mL.

### 4.3.3 24-hr Co-Culturing Under Different Glucose Conditions

We cultured the INS1 cells and adipocytes together with co-culture media contain different glucose concentrations for 24 hours to measure the insulin and IL-6 secretion. After that, we co-cultured the INS1 and adipocytes together with medium containing different glucose

concentrations for 24 hours and measured the insulin and IL-6 secretion. The result shows that during the regular culturing, both insulin and IL-6 secretion from INS1 cells and adipocytes increase when increasing the glucose concentration in the medium. In co-culture condition, the insulin and IL-6 secretion increase at all glucose concentrations compared to the regular culture condition (Figure 4-3A, B). Especially in high glucose condition, the IL-6 secretion has a significant increase during co-culture compared to the regular high glucose culture (Figure 4-3B).

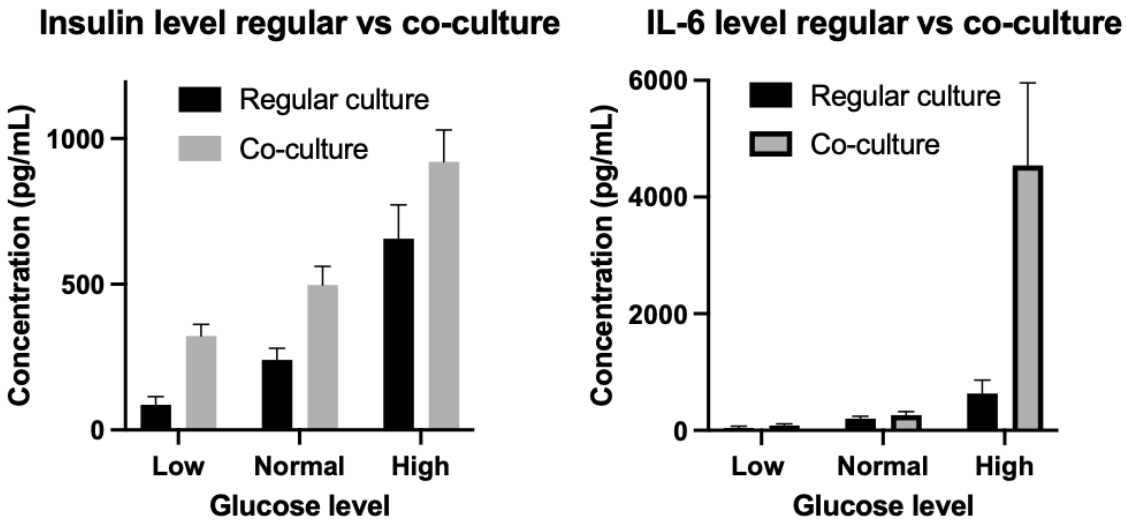


Figure 4-3. Co-culture vs regular culture. A. under co-culture environment, the insulin secretion is higher than the regular culture for all low, normal, and high glucose conditions. B. co-culture environment results in higher IL-6 expression compared to regular culture, especially in high glucose conditions.

### 4.3.4 Long-Term Co-Culture

We co-cultured the INS1 cells and adipocytes for 24 hours, 48 hours and 72 hours while measured the insulin and IL-6 secretion after every experiment. The result shows that insulin secreted from INS1 cells stimulated further IL-6 secretion from adipocytes. Furthermore, the IL-6 secretion from adipocytes also stimulated more insulin secretion from INS1 cells (Figure 4-3).

When co-culture INS1 cells and adipocytes longer, the insulin stimulated IL-6 secretion steadily increased while the IL-6 stimulated insulin secretion slowed (Figure 4-4).

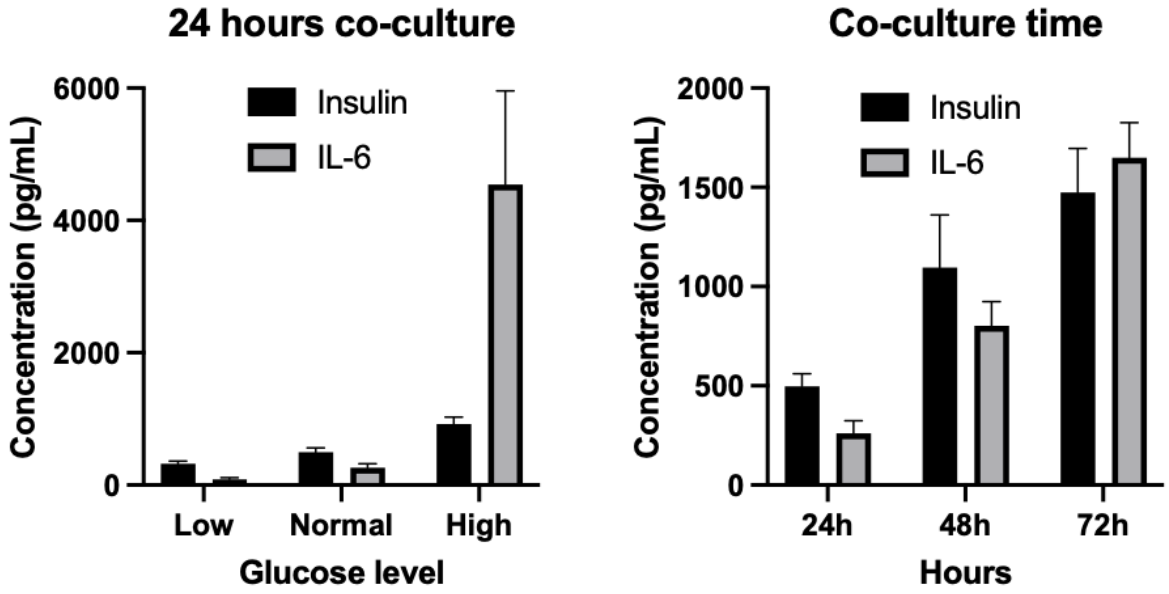


Figure 4-4. long-term co-culture. A. when co-culture of adipocytes and INS-1 cells, higher glucose concentration can stimulate more insulin and IL-6 secretion. B. long-term co-culture result in more insulin and IL-6 expressions.

### 4.3.5 ZnT-8 Measurement

After the co-culture of adipocytes and INS-1 cells, we measured the membrane Znt8 level using ZnT-8 Antibody (B-9) HRP. The result showed that under normal glucose co-culture conditions, the Znt8 level increases by the time, similar to insulin and Il-6 expression. At high glucose, 24 hours co-culture condition, the Znt8 level is higher than normal glucose at 48 hours co-culture but lower than normal glucose 72 hours co-culture. Compared to insulin and IL-6 expressions at same conditions, high glucose 24 hours insulin secretion is lower than 48 hours and 72 hours normal glucose co-culture condition, while high glucose 24 hours IL-6 secretion is much higher than 48

hours and 72 hours normal glucose co-culture condition. The results suggested that Znt8 expression is regulated by both insulin and IL-6 when co-cultured INS-1 cells and adipocytes at high glucose condition.

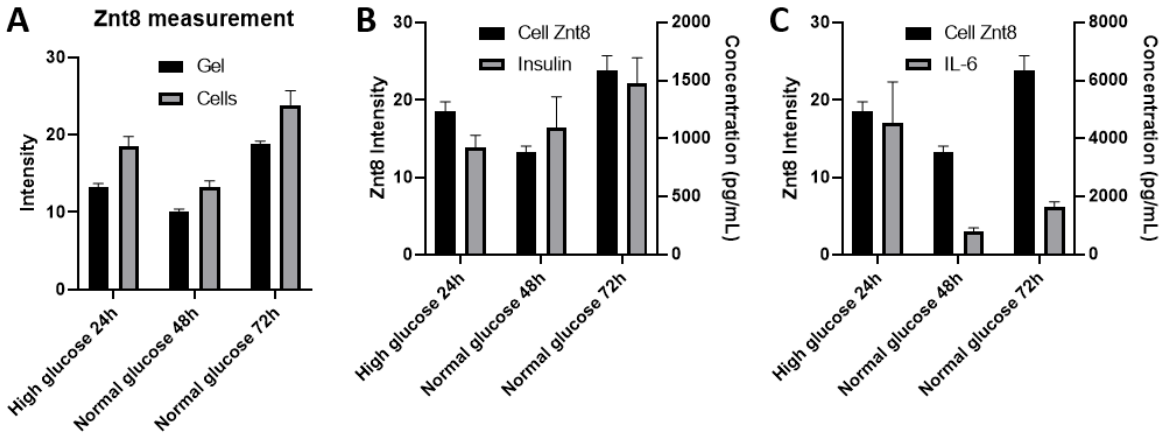


Figure 4-5. Znt8 measurement. A. Znt8 intensity under different conditions, with high glucose 24 hours, normal glucose 48 hours and 72 hours. B. Znt8 level fluorescence intensity compared to insulin secretion. C. Znt8 level fluorescence intensity compared to IL-6 secretion.

### 4.3.5 Discussion

We have developed a microfluidic co-culture system for INS-1 cells and adipocytes, which is a powerful platform for studying the relationship between obesity and diabetes. The system provides a stable and uniform flow of media across two cell culture channels. The two cell types are arranged in separate culture channels, with adipocytes in a culture chamber and INS-1 cells encapsulated in a hydrogel droplet. This arrangement better mimics the natural arrangement of INS-1 cells and adipocytes in the human body, allowing for the introduction of aqueous cell-cell interactions and effects through the recirculating media flow across the two channels. An

advantage of our system is that the microfluidic device can be placed under a fluorescence microscope for real-time imaging.

By examining insulin and IL-6 secretion from INS-1 cells and adipocytes, we found that the results matched current studies on diabetes. IL-6 can stimulate islet beta cells to secrete insulin, and in the other way around, insulin secreted from islet beta cells will stimulate adipocytes to secrete more IL-6. This two-way effect suggests that the hormone secretions from adipocytes and islet beta cells regulate cell behavior. In high glucose conditions, IL-6 expression significantly increases, as reported by K. Esposito et al. Our findings under co-culture conditions suggest that the mechanism of IL-6 and insulin expression differs from that of normal and low glucose conditions. K. Huang et al. reported that among prediabetes and type 2 diabetes patients, IL-6 levels are greatly correlated with prediabetes and insulin resistance. Another role that IL-6 plays in the immune system is that it induces the differentiation of activated B cells into Ab-producing plasma cells. Overexpression of IL-6 results in autoantibody production, which may lead to the development of type 1 diabetes.

## 4.4 Conclusion

Obesity and diabetes are often linked, and to better understand the mechanism between the two, we have developed a co-culture microfluidic device that provides a stable and well-controlled environment for the co-culture of different cell types. Unlike most current co-culture systems, our device integrates a powerful μTesla pump, which enables a recirculating system and facilitates interactions and crosstalk between different cell types.

Using our co-culture device, we co-cultured adipocytes and INS-1 cells together and stimulated the system with varying glucose levels for different amounts of time. After detecting and measuring the insulin and IL-6 secretion from the two types of cells, our results demonstrate that this system closely mimics *in vivo* conditions and can serve as a diabetes-on-a-chip model. Additionally, the high glucose condition provides a new direction for future studies on the mechanisms of adipocyte and islet INS-1 cell interactions in high glucose environments.

From a device standpoint, our integrated system is compatible with more cell co-culture and can be easily modified for a more complex co-culture system. Furthermore, our device can achieve multiple stimulations simultaneously. Overall, our powerful 3D-printed microfluidic co-culture system boasts advantages such as ease of fabrication, handling, and modification, as well as biocompatibility and high potential for upgradation. It is a great tool for bioengineering research.

# Chapter 5. Conclusion

In this dissertation, we demonstrated multiple microfluidics devices and a powerful integrated microfluidic pump. We showed different engineering approaches for diabetes research: By applying the oxygen gradient device, we could stimulate the islet beta cells with glucose and different oxygen concentration. By integrating the μTesla pump into microfluidic devices, we could stimulate the islet beta cells with shear stress and mimic blood flow. By co-culturing the beta cells and adipocytes in the same microfluidic device, we could mimic *in vivo* condition and stimulate cell-cell communications. We found that islet BetaTC6 cell oscillation peaks at 8% to 12% $O_2$. We showed that shear induced calcium influx and insulin secretion separate from glucose-insulin response. Lastly, the co-culturing of adipocytes and beta cells led to IL-6-induced insulin secretion and also insulin-induced IL-6 secretion, with the nuance that their behavior differs under different glucose concentration.

Overall, this dissertation showed that microfluidic can be widely used for diabetes research. Microfluidic techniques enables more interest studies to better understand this complex disease. Furthermore, microfluidics can uncover new disease mechanisms and propose novel therapeutic to make meaningful impacts on human health.

# Chapter 6. Future Directions

From the microfluidic-enhanced diabetes research in this dissertation, several new directions have been uncovered: microfluidic device fabrication using different materials for 3D printing, fully remote μTesla pump-integrated device fabrication, and FFA-hypoxia synergy effect on islet beta cell dysfunction.

## 6.1 Microfluidic Devices

Nowadays, the development of 3D printing techniques provides another direction in microfluidic device fabrication. The commercial SLP 3D printer can easily reach a 30 μm resolution, while the filament-based 3D printer resolution depends more on the nozzle size. From our optimization, a 150 μm nozzle diameter can output the best resolution of around 100 μm. To further improve the printing resolution, one way is to depend mostly on the manufacturing of the nozzle; a smaller nozzle size will enable better resolution. Another way is to use the SLP 3D printer, where the resolution depends on the laser system development. Although the current resolution meets most of the microfluidic device requirements, to better develop the microfluidic system, 3D printing material is another approach. For example, water-soluble 3D printing filament, hydrogel-based printing scaffold, shrink material, and PDMS compatible material. All these materials could help the fabrication process and provide a new way for microfluidic applications in bioengineering research.

## 6.2 μTesla Pump Integration

We have demonstrated the advantages of using our μTesla pump and how to integrate it into a microfluidic device to achieve recirculating co-culture. To take advantage of our μTesla pump and enhance its functions, there are a couple of approaches we could take. First, we could optimize the μTesla pump; the pump performance can be enhanced by changing the surface properties, such as the geometry, texture, and material. In this way, the water-rotor interaction can be changed, such as slip length, water contact angle, and water rotation direction. Another approach to improving the μTesla pump is to integrate remote control into the pump while scaling the pump to make it better fit the microscope stage. The final version of the μTesla pump should be a pump that can be integrated into various microfluidic devices, provide stable constant flow, and can be remotely controlled under a microscope. In this way, the μTesla could enable more applications in disease modeling and organ-on-chip projects, while having functions such as real-time protein expression detection and imaging, and real-time flow adjustments.

## 6.3 Mechanism between ER stress and diabetes

Both FFA and hypoxia are known risk factors in obesity. Elevated FFA levels, which are common in obesity, have effects on adipocytes that appear to function through the ER stress sensor PERK (protein kinase R (PKR)-like endoplasmic reticulum kinase). A large number of research shows that high ROS production by the mitochondria has strong relationship to ER stress in diabetes, cell autophagy and mitophagy also play an important part in diabetes complications. However, the mechanisms between ER stress, glucose, FFA, ATP, calcium, insulin, are still

unclear, better understanding of the mechanisms will help us develop efficient therapeutic methods and drugs used in diabetes.

# References


1. Heymans, C. and J.J. Bouckaert, *Sinus caroticus and respiratory reflexes: I. Cerebral blood flow and respiration. Adrenaline apnoea.* J Physiol, 1930. **69**(2): p. 254-66.
2. Ivan, M., et al., *HIFalpha targeted for VHL-mediated destruction by proline hydroxylation: implications for O2 sensing.* Science, 2001. **292**(5516): p. 464-8.
3. Jaakkola, P., et al., *Targeting of HIF-alpha to the von Hippel-Lindau ubiquitylation complex by O2-regulated prolyl hydroxylation.* Science, 2001. **292**(5516): p. 468-72.
4. Wang, G.L., et al., *Hypoxia-inducible factor 1 is a basic-helix-loop-helix-PAS heterodimer regulated by cellular O2 tension.* Proc Natl Acad Sci U S A, 1995. **92**(12): p. 5510-4.
5. Hockel, M. and P. Vaupel, *Tumor hypoxia: definitions and current clinical, biologic, and molecular aspects.* J Natl Cancer Inst, 2001. **93**(4): p. 266-76.
6. Pistollato, F., et al., *Intratumoral hypoxic gradient drives stem cells distribution and MGMT expression in glioblastoma.* Stem Cells, 2010. **28**(5): p. 851-62.
7. Helmlinger, G., et al., *Interstitial pH and pO2 gradients in solid tumors in vivo: high-resolution measurements reveal a lack of correlation.* Nat Med, 1997. **3**(2): p. 177-82.
8. Trayhurn, P., *Hypoxia and adipose tissue function and dysfunction in obesity.* Physiol Rev, 2013. **93**(1): p. 1-21.
9. Sano, S., et al., *Lipid synthesis is promoted by hypoxic adipocyte-derived exosomes in 3T3-L1 cells.* Biochem Biophys Res Commun, 2014. **445**(2): p. 327-33.
10. Regazzetti, C., et al., *Hypoxia decreases insulin signaling pathways in adipocytes.* Diabetes, 2009. **58**(1): p. 95-103.
11. Pedraza, E., et al., *Preventing hypoxia-induced cell death in beta cells and islets via hydrolytically activated, oxygen-generating biomaterials.* Proc Natl Acad Sci U S A, 2012. **109**(11): p. 4245-50.
12. Kim, J.J., et al., *Hypoxia Increases beta-Cell Death by Activating Pancreatic Stellate Cells within the Islet.* Diabetes Metab J, 2020. **44**(6): p. 919-927.
13. Karsai, M., et al., *Lack of ZnT8 protects pancreatic islets from hypoxia- and cytokine-induced cell death.* J Endocrinol, 2022. **253**(1): p. 1-11.
14. Benninger, R.K., et al., *Gap junction coupling and calcium waves in the pancreatic islet.* Biophys J, 2008. **95**(11): p. 5048-61.
15. Rocheleau, J.V., et al., *Critical role of gap junction coupled KATP channel activity for regulated insulin secretion.* PLoS Biol, 2006. **4**(2): p. e26.
16. Santos, R.M., et al., *Widespread synchronous [Ca2+]i oscillations due to bursting electrical activity in single pancreatic islets.* Pflugers Arch, 1991. **418**(4): p. 417-22.
17. Easley, C.J., et al., *Quantitative measurement of zinc secretion from pancreatic islets with high temporal resolution using droplet-based microfluidics.* Anal Chem, 2009. **81**(21): p. 9086-95.
18. Shackman, J.G., et al., *Dynamic monitoring of glucagon secretion from living cells on a microfluidic chip.* Anal Bioanal Chem, 2012. **402**(9): p. 2797-803.

19. Zhang, X., et al., *Microfluidic system for generation of sinusoidal glucose waveforms for entrainment of islets of Langerhans.* Anal Chem, 2010. **82**(15): p. 6704-11.
20. Nourmohammadzadeh, M., et al., *Microfluidic array with integrated oxygenation control for real-time live-cell imaging: effect of hypoxia on physiology of microencapsulated pancreatic islets.* Anal Chem, 2013. **85**(23): p. 11240-9.
21. Lo, J.F., et al., *Islet preconditioning via multimodal microfluidic modulation of intermittent hypoxia.* Anal Chem, 2012. **84**(4): p. 1987-93.
22. Li, Z., et al., *Balancing oxygen diffusion and convection in spiral microfluidics to mimic radial biological gradients.* Biomed Microdevices, 2015. **17**(1): p. 14.
23. Bertram, R., A. Sherman, and L.S. Satin, *Metabolic and electrical oscillations: partners in controlling pulsatile insulin secretion.* Am J Physiol Endocrinol Metab, 2007. **293**(4): p. E890-900.
24. Carvalho, C.P., et al., *Beta cell coupling and connexin expression change during the functional maturation of rat pancreatic islets.* Diabetologia, 2010. **53**(7): p. 1428-37.
25. Cao, D., et al., *Mechanisms for the coordination of intercellular calcium signaling in insulin-secreting cells.* J Cell Sci, 1997. **110 ( Pt 4)**: p. 497-504.
26. Tsaneva-Atanasova, K., et al., *Diffusion of calcium and metabolites in pancreatic islets: killing oscillations with a pitchfork.* Biophys J, 2006. **90**(10): p. 3434-46.
27. Bertram, R., et al., *The phantom burster model for pancreatic beta-cells.* Biophys J, 2000. **79**(6): p. 2880-92.
28. Pedersen, M.G., *Phantom bursting is highly sensitive to noise and unlikely to account for slow bursting in beta-cells: considerations in favor of metabolically driven oscillations.* J Theor Biol, 2007. **248**(2): p. 391-400.
29. Ristow, M., et al., *Deficiency of phosphofructo-1-kinase/muscle subtype in humans is associated with impairment of insulin secretory oscillations.* Diabetes, 1999. **48**(8): p. 1557-61.
30. Bertram, R., et al., *Interaction of glycolysis and mitochondrial respiration in metabolic oscillations of pancreatic islets.* Biophys J, 2007. **92**(5): p. 1544-55.
31. Jung, S.K., C.A. Aspinwall, and R.T. Kennedy, *Detection of multiple patterns of oscillatory oxygen consumption in single mouse islets of Langerhans.* Biochem Biophys Res Commun, 1999. **259**(2): p. 331-5.
32. Jung, S.K., et al., *Correlated oscillations in glucose consumption, oxygen consumption, and intracellular free Ca(2+) in single islets of Langerhans.* J Biol Chem, 2000. **275**(9): p. 6642-50.
33. Hellman, B., et al., *Influence of anoxia on glucose metabolism in pancreatic islets: lack of correlation between fructose-1,6-diphosphate and apparent glycolytic flux.* Diabetologia, 1975. **11**(6): p. 495-500.
34. Longo, E.A., et al., *Oscillations in cytosolic free Ca2+, oxygen consumption, and insulin secretion in glucose-stimulated rat pancreatic islets.* J Biol Chem, 1991. **266**(14): p. 9314-9.
35. Barbosa, R.M., et al., *Control of pulsatile 5-HT/insulin secretion from single mouse pancreatic islets by intracellular calcium dynamics.* J Physiol, 1998. **510 ( Pt 1)**(Pt 1): p. 135-43.
36. Westacott, M.J., N.W.F. Ludin, and R.K.P. Benninger, *Spatially Organized beta-Cell Subpopulations Control Electrical Dynamics across Islets of Langerhans.* Biophys J, 2017. **113**(5): p. 1093-1108.

37. Zhao, Z., et al., *On-chip porous microgel generation for microfluidic enhanced VEGF detection.* Biosens Bioelectron, 2015. **74**: p. 305-12.
38. Duan, K., G. Ghosh, and J.F. Lo, *Optimizing Multiplexed Detections of Diabetes Antibodies via Quantitative Microfluidic Droplet Array.* Small, 2017. **13**(46).
39. Arai, T., F. Arai, and M. Yamato, *Hyper Bio Assembler for 3D Cellular Systems*. 2015: Springer.
40. Poitout, V., et al., *Morphological and functional characterization of beta TC-6 cells--an insulin-secreting cell line derived from transgenic mice.* Diabetes, 1995. **44**(3): p. 306-13.
41. Tornheim, K., *Are metabolic oscillations responsible for normal oscillatory insulin secretion?* Diabetes, 1997. **46**(9): p. 1375-80.
42. Yaney, G.C., et al., *Phosphofructokinase isozymes in pancreatic islets and clonal beta-cells (INS-1).* Diabetes, 1995. **44**(11): p. 1285-9.
43. Chay, T.R., *Effects of extracellular calcium on electrical bursting and intracellular and luminal calcium oscillations in insulin secreting pancreatic beta-cells.* Biophys J, 1997. **73**(3): p. 1673-88.
44. Rinzel, J., *BURSTING OSCILLATIONS IN AN EXCITABLE MEMBRANE MODEL*. 1985: Springer.
45. Stokes, C.L. and J. Rinzel, *Diffusion of extracellular K+ can synchronize bursting oscillations in a model islet of Langerhans.* Biophys J, 1993. **65**(2): p. 597-607.
46. Chay, T.R.J.T.J.o.P.C., *Eyring rate theory in excitable membranes: application to neuronal oscillations.* 1983. **87**(15): p. 2935-2940.
47. Detimary, P., P. Gilon, and J.C. Henquin, *Interplay between cytoplasmic Ca2+ and the ATP/ADP ratio: a feedback control mechanism in mouse pancreatic islets.* Biochem J, 1998. **333 ( Pt 2)**(Pt 2): p. 269-74.
48. Satin, L.S., et al., *Pulsatile insulin secretion, impaired glucose tolerance and type 2 diabetes.* Mol Aspects Med, 2015. **42**: p. 61-77.
49. Cohen, M.V., C.P. Baines, and J.M. Downey, *Ischemic preconditioning: from adenosine receptor to KATP channel.* Annu Rev Physiol, 2000. **62**: p. 79-109.
50. Konstantinov, I.E., et al., *Remote ischemic preconditioning of the recipient reduces myocardial ischemia-reperfusion injury of the denervated donor heart via a Katp channel-dependent mechanism.* Transplantation, 2005. **79**(12): p. 1691-5.
51. Nunemaker, C.S., et al., *Individual mice can be distinguished by the period of their islet calcium oscillations: is there an intrinsic islet period that is imprinted in vivo?* Diabetes, 2005. **54**(12): p. 3517-22.
52. Ortiz-Prado, E., et al., *Partial pressure of oxygen in the human body: a general review.* Am J Blood Res, 2019. **9**(1): p. 1-14.
53. Carlsson, P.O., et al., *Measurements of oxygen tension in native and transplanted rat pancreatic islets.* Diabetes, 1998. **47**(7): p. 1027-32.
54. Papas, K.K., et al., *A stirred microchamber for oxygen consumption rate measurements with pancreatic islets.* Biotechnol Bioeng, 2007. **98**(5): p. 1071-82.
55. F Lo, J., et al., *Microfluidic Control of Hypoxia Aids Investigations of Islet Pathophysiology.* 2013. **5**(3): p. 209-215.
56. Pepper, A.R., et al., *Revascularization of transplanted pancreatic islets and role of the transplantation site.* Clin Dev Immunol, 2013. **2013**: p. 352315.
57. Olsson, R., et al., *Increased numbers of low-oxygenated pancreatic islets after intraportal islet transplantation.* Diabetes, 2011. **60**(9): p. 2350-3.

58. Moritz, W., et al., *Apoptosis in hypoxic human pancreatic islets correlates with HIF-1alpha expression.* FASEB J, 2002. **16**(7): p. 745-7.
59. Markovic, R., et al., *Progressive glucose stimulation of islet beta cells reveals a transition from segregated to integrated modular functional connectivity patterns.* Sci Rep, 2015. **5**: p. 7845.
60. Gosak, M., et al., *The relationship between node degree and dissipation rate in networks of diffusively coupled oscillators and its significance for pancreatic beta cells.* Chaos, 2015. **25**(7): p. 073115.
61. Daraio, T., et al., *SNAP-25b-deficiency increases insulin secretion and changes spatiotemporal profile of Ca(2+)oscillations in beta cell networks.* Sci Rep, 2017. **7**(1): p. 7744.
62. Gosak, M., et al., *Multilayer network representation of membrane potential and cytosolic calcium concentration dynamics in beta cells.* 2015. **80**: p. 76-82.
63. Kretzmer, G., K.J.A.m. Schügerl, and biotechnology, *Response of mammalian cells to shear stress.* 1991. **34**: p. 613-616.
64. Klak, M., et al., *Bionic organs: Shear forces reduce pancreatic islet and mammalian cell viability during the process of 3D bioprinting.* 2021. **12**(3): p. 304.
65. Tharmalingam, T., et al., *Pluronic enhances the robustness and reduces the cell attachment of mammalian cells.* 2008. **39**: p. 167-177.
66. Meurant, G., *Physical forces and the mammalian cell*. 2012: Academic Press.
67. Christophis, C., M. Grunze, and A.J.P.C.C.P. Rosenhahn, *Quantification of the adhesion strength of fibroblast cells on ethylene glycol terminated self-assembled monolayers by a microfluidic shear force assay.* 2010. **12**(17): p. 4498-4504.
68. Simmers, M.B., et al., *Arterial shear stress regulates endothelial cell-directed migration, polarity, and morphology in confluent monolayers.* 2007. **293**(3): p. H1937-H1946.
69. Huang, Q., et al., *Fluid shear stress and tumor metastasis.* 2018. **8**(5): p. 763.
70. Ohashi, T. and M.J.F.d.r. Sato, *Remodeling of vascular endothelial cells exposed to fluid shear stress: experimental and numerical approach.* 2005. **37**(1-2): p. 40.
71. Kadohama, T., et al., *Effects of different types of fluid shear stress on endothelial cell proliferation and survival.* 2007. **212**(1): p. 244-251.
72. Huang, Y., et al., *Effects of shear stress on differentiation of stem cells into endothelial cells.* 2021. **13**(7): p. 894.
73. Frangos, J., et al., *Shear stress induced stimulation of mammalian cell metabolism.* 1988. **32**(8): p. 1053-1060.
74. Li, Y.-S.J., J.H. Haga, and S.J.J.o.b. Chien, *Molecular basis of the effects of shear stress on vascular endothelial cells.* 2005. **38**(10): p. 1949-1971.
75. Shen, J., et al., *Fluid shear stress modulates cytosolic free calcium in vascular endothelial cells.* 1992. **262**(2): p. C384-C390.
76. Wiesner, T.F., B.C. Berk, and R.M.J.P.o.t.N.A.o.S. Nerem, *A mathematical model of the cytosolic-free calcium response in endothelial cells to fluid shear stress.* 1997. **94**(8): p. 3726-3731.
77. Park, J., Z. Fan, and C.X.J.J.o.b. Deng, *Effects of shear stress cultivation on cell membrane disruption and intracellular calcium concentration in sonoporation of endothelial cells.* 2011. **44**(1): p. 164-169.
78. Prentki, M.J.E.J.o.E., *New insights into pancreatic β-cell metabolic signaling in insulin secretion.* 1996. **134**(3): p. 272-286.

79. Li, C., et al., *Functional and metabolomic consequences of KATP channel inactivation in human islets.* 2017. **66**(7): p. 1901-1913.
80. Aamodt, K.I., A.C.J.D. Powers, Obesity, and Metabolism, *Signals in the pancreatic islet microenvironment influence β-cell proliferation.* 2017. **19**: p. 124-136.
81. Rutter, G.A.J.M.a.o.m., *Nutrient–secretion coupling in the pancreatic islet β-cell: recent advances.* 2001. **22**(6): p. 247-284.
82. Jensen, M.V., et al., *Compensatory responses to pyruvate carboxylase suppression in islet β-cells: Preservation of glucose-stimulated insulin secretion.* 2006. **281**(31): p. 22342-22351.
83. Ghosh, A., et al., *The role of ATP and free ADP in metabolic coupling during fuel-stimulated insulin release from islet beta-cells in the isolated perfused rat pancreas.* 1991. **266**(34): p. 22887-22892.
84. Koster, J.C., M.A. Permutt, and C.G.J.D. Nichols, *Diabetes and insulin secretion: the ATP-sensitive K+ channel (KATP) connection.* 2005. **54**(11): p. 3065-3072.
85. Satin, L.S.J.E., *Localized calcium influx in pancreatic β-cells: its significance for Ca 2+-dependent insulin secretion from the islets of Langerhans.* 2000. **13**: p. 251-262.
86. Hou, J.C., et al., *Insulin granule biogenesis, trafficking and exocytosis.* 2009. **80**: p. 473-506.
87. Chen, H., et al., *Microfluidic models of physiological or pathological flow shear stress for cell biology, disease modeling and drug development.* 2019. **117**: p. 186-199.
88. Lee, J., et al., *A microfluidic cardiac flow profile generator for studying the effect of shear stress on valvular endothelial cells.* 2018. **18**(19): p. 2946-2954.
89. Leclerc, E., et al., *Study of osteoblastic cells in a microfluidic environment.* 2006. **27**(4): p. 586-595.
90. Luo, C., et al., *A fast cell loading and high -throughput microfluidic system for long -term cell culture in zero -flow environments.* 2008. **101**(1): p. 190-195.
91. Khodadadei, F., A.P. Liu, and C.A.J.C.b. Harris, *A high-resolution real-time quantification of astrocyte cytokine secretion under shear stress for investigating hydrocephalus shunt failure.* 2021. **4**(1): p. 387.
92. Lu, H., et al., *Microfluidic shear devices for quantitative analysis of cell adhesion.* 2004. **76**(18): p. 5257-5264.
93. Sonmez, U.M., et al., *Endothelial cell polarization and orientation to flow in a novel microfluidic multimodal shear stress generator.* 2020. **20**(23): p. 4373-4390.
94. Velve-Casquillas, G., et al., *Microfluidic tools for cell biological research.* 2010. **5**(1): p. 28-47.
95. Riehl, B.D. and J.Y.J.C. Lim, *Macro and microfluidic flows for skeletal regenerative medicine.* 2012. **1**(4): p. 1225-1245.
96. Kimura, H., et al., *Organ/body-on-a-chip based on microfluidic technology for drug discovery.* 2018. **33**(1): p. 43-48.
97. Park, J. and J.-K.J.L.o.a.C. Park, *Integrated microfluidic pumps and valves operated by finger actuation.* 2019. **19**(18): p. 2973-2977.
98. Clime, L., et al., *Active pumping and control of flows in centrifugal microfluidics.* 2019. **23**: p. 1-22.
99. Couto, H., J. Duarte, and D. Bastos-Netto. *The tesla turbine revisited*. in *Proceedings of the Eighth Asia-Pacific International Symposium on Combustion and Energy Utilization*. 2006.

100. Ozcelik, A., Z.J.M. Aslan, and nanofluidics, *A practical microfluidic pump enabled by acoustofluidics and 3D printing.* 2021. **25**: p. 1-10.
101. Fournier, Z., et al., *Mechanical properties of wet granular materials.* Journal of Physics: Condensed Matter, 2005. **17**(9): p. S477.
102. Habhab, M.-B., T. Ismail, and J.F.J.S. Lo, *A laminar flow-based microfluidic tesla pump via lithography enabled 3D printing.* 2016. **16**(11): p. 1970.
103. Byun, C.K., et al., *Pumps for microfluidic cell culture.* 2014. **35**(2-3): p. 245-257.
104. Sung, J.H., C. Kam, and M.L.J.L.o.a.C. Shuler, *A microfluidic device for a pharmacokinetic–pharmacodynamic (PK–PD) model on a chip.* 2010. **10**(4): p. 446-455.
105. Beebe, D.J., G.A. Mensing, and G.M.J.A.r.o.b.e. Walker, *Physics and applications of microfluidics in biology.* 2002. **4**(1): p. 261-286.
106. Hung, P.J., et al., *Continuous perfusion microfluidic cell culture array for high-throughput cell-based assays.* 2005. **89**(1): p. 1-8.
107. Zeng, W., S. Li, and Z. Wang. *Characterization of syringe-pump-driven versus pressure-driven microfluidic flows*. in *2015 International Conference on Fluid Power and Mechatronics (FPM)*. 2015. IEEE.
108. Schneider, S., et al., *Peristaltic on-chip pump for tunable media circulation and whole blood perfusion in PDMS-free organ-on-chip and Organ-Disc systems.* 2021. **21**(20): p. 3963-3978.
109. Skafte-Pedersen, P., et al., *Multi-channel peristaltic pump for microfluidic applications featuring monolithic PDMS inlay.* 2009. **9**(20): p. 3003-3006.
110. Ren, Y., L.M.-C. Chow, and W.W.-F.J.B.m. Leung, *Cell culture using centrifugal microfluidic platform with demonstration on Pichia pastoris.* 2013. **15**: p. 321-337.
111. Du, X., et al., *Microfluidic pumps employing surface acoustic waves generated in ZnO thin films.* 2009. **105**(2): p. 024508.
112. Gallas, Q., et al., *Lumped element modeling of piezoelectric-driven synthetic jet actuators.* 2003. **41**(2): p. 240-247.
113. Urbanski, J.P., et al., *The effect of step height on the performance of three-dimensional ac electro-osmotic microfluidic pumps.* 2007. **309**(2): p. 332-341.
114. Munyan, J.W., et al., *Electrically actuated, pressure-driven microfluidic pumps.* 2003. **3**(4): p. 217-220.
115. Steigert, J., et al., *Integrated siphon-based metering and sedimentation of whole blood on a hydrophilic lab-on-a-disk.* 2007. **9**: p. 675-679.
116. Hayes, B., et al., *Rapid Fabrication of Low-Cost Thermal Bubble-Driven Micro-Pumps.* 2022. **13**(10): p. 1634.
117. Park, J. and J.-K.J.A.C. Park, *Finger-actuated microfluidic display for smart blood typing.* 2019. **91**(18): p. 11636-11642.
118. Armstrong, J.H., *An investigation of the performance of a modified Tesla turbine*. 1952, Georgia Institute of Technology.
119. Rice, W., *An analytical and experimental investigation of multiple-disk turbines.* 1965.
120. Lemma, E., et al., *Characterisation of a small viscous flow turbine.* 2008. **33**(1): p. 96-105.
121. Engin, T., et al., *Design, testing and two-dimensional flow modeling of a multiple-disk fan.* 2009. **33**(8): p. 1180-1187.
122. Talluri, L., et al., *Design and optimization of a Tesla turbine for ORC applications.* 2018. **226**: p. 300-319.

123. Rusin, K., et al., *Comparison of methods for the determination of Tesla turbine performance.* 2019. **57**.
124. Melchels, F.P., J. Feijen, and D.W.J.B. Grijpma, *A review on stereolithography and its applications in biomedical engineering.* 2010. **31**(24): p. 6121-6130.
125. Gong, H., et al., *Custom 3D printer and resin for 18 μm× 20 μm microfluidic flow channels.* 2017. **17**(17): p. 2899-2909.
126. Warr, C.A., et al., *3d-printed microfluidic droplet generator with hydrophilic and hydrophobic polymers.* 2021. **12**(1): p. 91.
127. Monaghan, T., et al., *Customisable 3D printed microfluidics for integrated analysis and optimisation.* 2016. **16**(17): p. 3362-3373.
128. He, Y., et al., *Developments of 3D printing microfluidics and applications in chemistry and biology: a review.* 2016. **28**(8): p. 1658-1678.
129. Ji, Q., et al., *A modular microfluidic device via multimaterial 3D printing for emulsion generation.* 2018. **8**(1): p. 4791.
130. Zhu, F., et al. *3D printed polymers toxicity profiling: A caution for biodevice applications*. in *Micro+ Nano Materials, Devices, and Systems*. 2015. SPIE.
131. de Almeida Monteiro Melo Ferraz, M., et al., *3D printed mold leachates in PDMS microfluidic devices.* 2020. **10**(1): p. 1-9.
132. Oskui, S.M., et al., *Assessing and reducing the toxicity of 3D-printed parts.* 2016. **3**(1): p. 1-6.
133. Musgrove, H.B., M.A. Catterton, and R.R.J.A.C.A. Pompano, *Applied tutorial for the design and fabrication of biomicrofluidic devices by resin 3D printing.* 2022: p. 339842.
134. Lim, K.S., et al., *Bio-resin for high resolution lithography-based biofabrication of complex cell-laden constructs.* 2018. **10**(3): p. 034101.
135. Nielsen, A.V., et al., *3D printed microfluidics.* 2020. **13**: p. 45-65.
136. Swetham, T., et al., *A Critical Review on of 3D Printing Materials and Details of Materials used in FDM.* 2017. **3**(2): p. 353-361.
137. Lee, K.G., et al., *3D printed modules for integrated microfluidic devices.* 2014. **4**(62): p. 32876-32880.
138. Nelson, M.D., et al., *Flexible, transparent, sub-100 μm microfluidic channels with fused deposition modeling 3D-printed thermoplastic polyurethane.* 2019. **29**(9): p. 095010.
139. Gottenbos, B., et al., *Antimicrobial effects of positively charged surfaces on adhering Gram-positive and Gram-negative bacteria.* 2001. **48**(1): p. 7-13.
140. Lu, H., et al., *Effects of poly (L-lysine), poly (acrylic acid) and poly (ethylene glycol) on the adhesion, proliferation and chondrogenic differentiation of human mesenchymal stem cells.* 2009. **20**(5-6): p. 577-589.
141. Zebisch, K., et al., *Protocol for effective differentiation of 3T3-L1 cells to adipocytes.* 2012. **425**(1): p. 88-90.
142. Ramirez-Zacarias, J., F. Castro-Munozledo, and W.J.H. Kuri-Harcuch, *Quantitation of adipose conversion and triglycerides by staining intracytoplasmic lipids with Oil red O.* 1992. **97**: p. 493-497.
143. Burke, C., et al. *Effects of process parameter variation on the surface roughness of polylactic acid (PLA) materials using design of experiments (DOE)*. in *IOP Conference Series: Materials Science and Engineering*. 2020. IOP Publishing.

144. Chaidas, D., et al. *The impact of temperature changing on surface roughness of FFF process*. in *IOP conference series: materials science and engineering*. 2016. IOP Publishing.
145. Werner, E.M., B.X. Lam, and E.E.J.M. Hui, *Phase-Optimized Peristaltic Pumping by Integrated Microfluidic Logic.* 2022. **13**(10): p. 1784.
146. Cooney, C.G., et al., *A plastic, disposable microfluidic flow cell for coupled on-chip PCR and microarray detection of infectious agents.* 2012. **14**: p. 45-53.
147. Dosh, R.H., et al., *Long-term in vitro 3D hydrogel co-culture model of inflammatory bowel disease.* 2019. **9**(1): p. 1-15.
148. Mountcastle, S.E., et al., *A review of co-culture models to study the oral microenvironment and disease.* 2020. **12**(1): p. 1773122.
149. Saini, H., et al., *3D cardiac microtissues encapsulated with the co‐culture of cardiomyocytes and cardiac fibroblasts.* 2015. **4**(13): p. 1961-1971.
150. Chemmarappally, J.M., et al., *A co-culture nanofibre scaffold model of neural cell degeneration in relevance to Parkinson's disease.* 2020. **10**(1): p. 1-14.
151. Romualdo, G.R., et al., *Sorafenib reduces steatosis‐induced fibrogenesis in a human 3D co‐culture model of non‐alcoholic fatty liver disease.* 2021. **36**(2): p. 168-176.
152. Goers, L., P. Freemont, and K.M.J.J.o.T.R.S.I. Polizzi, *Co-culture systems and technologies: taking synthetic biology to the next level.* 2014. **11**(96): p. 20140065.
153. Ma, S.H., et al., *An endothelial and astrocyte co-culture model of the blood–brain barrier utilizing an ultra-thin, nanofabricated silicon nitride membrane.* 2005. **5**(1): p. 74-85.
154. Jinno, S., et al., *Microfabricated multilayer parylene‐C stencils for the generation of patterned dynamic co‐cultures.* 2008. **86**(1): p. 278-288.
155. Dai, W., et al., *Convenient, Reliable, Bias‐Free Dynamic Patterning of Multiple Types of Cells into Precisely Defined Micropatterns for Co‐Culture Study.* 2016. **2**(5): p. 447-453.
156. Nienow, A.W.J.A.c.c., *Mass transfer and mixing across the scales in animal cell culture.* 2015: p. 137-167.
157. Haycock, J.W.J.D.c.c.m. and protocols, *3D cell culture: a review of current approaches and techniques.* 2011: p. 1-15.
158. Mi, S., et al., *Microfluidic co-culture system for cancer migratory analysis and anti-metastatic drugs screening.* 2016. **6**(1): p. 1-11.
159. Chen, Q., et al., *Microfluidic isolation of highly pure embryonic stem cells using feeder-separated co-culture system.* 2013. **3**(1): p. 2433.
160. Zhou, Q., et al., *Liver injury-on-a-chip: microfluidic co-cultures with integrated biosensors for monitoring liver cell signaling during injury.* 2015. **15**(23): p. 4467-4478.
161. Middleton, K., et al., *Microfluidic co-culture platform for investigating osteocyte-osteoclast signalling during fluid shear stress mechanostimulation.* 2017. **59**: p. 35-42.
162. Jie, M., et al., *Integrated microfluidic system for cell co-culture and simulation of drug metabolism.* 2016. **6**(59): p. 54564-54572.
163. Bricks, T., et al., *Development of a new microfluidic platform integrating co-cultures of intestinal and liver cell lines.* 2014. **28**(5): p. 885-895.
164. Li, W., et al., *Advances in tumor-endothelial cells co-culture and interaction on microfluidics.* 2018. **8**(4): p. 210-218.

165. Gao, Y., et al., *A versatile valve-enabled microfluidic cell co-culture platform and demonstration of its applications to neurobiology and cancer biology.* 2011. **13**: p. 539-548.
166. Shah, P., et al., *A microfluidics-based in vitro model of the gastrointestinal human–microbe interface.* 2016. **7**(1): p. 11535.
167. Ahn, J., et al., *Modeling of three-dimensional innervated epidermal like-layer in a microfluidic chip-based coculture system.* 2023. **14**(1): p. 1488.
168. Sato, K. and K.J.A.S. Sato, *Recent progress in the development of microfluidic vascular models.* 2018. **34**(7): p. 755-764.
169. Fernandes, J.T., et al., *A novel microfluidic cell co-culture platform for the study of the molecular mechanisms of Parkinson's disease and other synucleinopathies.* 2016. **10**: p. 511.
170. Lee, J.M., et al., *Hydrogel microfluidic co-culture device for photothermal therapy and cancer migration.* 2017. **38**(9-10): p. 1318-1324.
171. Patel, D., et al., *Microfluidic co-cultures with hydrogel-based ligand trap to study paracrine signals giving rise to cancer drug resistance.* 2015. **15**(24): p. 4614-4624.
172. Dinh, N.-D., et al., *Microfluidic construction of minimalistic neuronal co-cultures.* 2013. **13**(7): p. 1402-1412.
173. Boden, G.J.E. and m.c.o.N. America, *Obesity and free fatty acids.* 2008. **37**(3): p. 635-646.
174. King, G.L.J.J.o.p., *The role of inflammatory cytokines in diabetes and its complications.* 2008. **79**: p. 1527-1534.
175. Fain, J.N.J.V. and Hormones, *Release of interleukins and other inflammatory cytokines by human adipose tissue is enhanced in obesity and primarily due to the nonfat cells.* 2006. **74**: p. 443-477.
176. Reverendo, M., et al., *At the crossway of ER-stress and proinflammatory responses.* 2019. **286**(2): p. 297-310.
177. Chipurupalli, S., U. Samavedam, and N.J.F.i.m. Robinson, *Crosstalk between ER stress, autophagy and inflammation.* 2021. **8**: p. 758311.
178. Jiao, P., et al., *FFA-induced adipocyte inflammation and insulin resistance: involvement of ER stress and IKKβ pathways.* 2011. **19**(3): p. 483-491.
179. Díaz-Bulnes, P., et al., *Crosstalk between hypoxia and ER stress response: a key regulator of macrophage polarization.* 2020. **10**: p. 2951.
180. Rozpedek, W., et al., *The role of the PERK/eIF2α/ATF4/CHOP signaling pathway in tumor progression during endoplasmic reticulum stress.* 2016. **16**(6): p. 533-544.
181. Urra, H. and C.J.M.c. Hetz, *A novel ER stress-independent function of the UPR in angiogenesis.* 2014. **54**(4): p. 542-544.
182. Zhao, L. and S.L.J.C.o.i.c.b. Ackerman, *Endoplasmic reticulum stress in health and disease.* 2006. **18**(4): p. 444-452.
183. Gaspar, J.M. and L.A.J.F.i.N. Velloso, *Hypoxia inducible factor as a central regulator of metabolism–implications for the development of obesity.* 2018. **12**: p. 813.
184. Bouzakri, K., et al., *Bimodal effect on pancreatic β-cells of secretory products from normal or insulin-resistant human skeletal muscle.* 2011. **60**(4): p. 1111-1121.